TU Delft

Delft University of Technology

Operando spectroscopic methods to study electrochemical processes

Firet, Nienke

DOI
10.4233/uuid:d0e0ef9d-caa5-4794-86b8-ab0eaabd0de5

Publication date
2020

Document Version
Final published version

Citation (APA)
Firet, N. (2020). *Operando spectroscopic methods to study electrochemical processes*. [Dissertation (TU Delft), Delft University of Technology]. https://doi.org/10.4233/uuid:d0e0ef9d-caa5-4794-86b8-ab0eaabd0de5

Important note
To cite this publication, please use the final published version (if applicable).
Please check the document version above.

Copyright
Other than for strictly personal use, it is not permitted to download, forward or distribute the text or part of it, without the consent of the author(s) and/or copyright holder(s), unless the work is under an open content license such as Creative Commons.

Takedown policy
Please contact us and provide details if you believe this document breaches copyrights.
We will remove access to the work immediately and investigate your claim.

This work is downloaded from Delft University of Technology.
For technical reasons the number of authors shown on this cover page is limited to a maximum of 10.

Operando spectroscopic methods to study electrochemical processes

Proefschrift

ter verkrijging van de graad van doctor
aan de Technische Universiteit Delft,
op gezag van de Rector Magnificus Prof.dr.ir. T.H.J.J. van der Hagen,
voorzitter van het College voor Promoties,
in het openbaar te verdedigen op
vrijdag 5 juni 2020 om 12:30 uur

door

Nienke Joan FIRET
Master of Science in Chemical Engineering
Master of Science in Sustainable Energy Technology
Universiteit Twente, Nederland

This dissertation has been approved by the promotors.

Composition of the doctoral committee:

Rector Magnificus	chairman
Dr. W.A. Smith	Delft University of Technology, promotor
Prof.dr. B. Dam	Delft University of Technology, promotor

Independent members:

Prof.dr. A. Urakawa	Delft University of Technology
Prof.dr. M. Tromp	University of Groningen
Prof.dr.ir. J. Huskens	University of Twente
Dr. M. Escudero Escribano	University of Copenhagen, Denmark
Prof.dr. H. Geerlings	Delft University of Technology, reserve member

Other member:

Dr. A. Longo	European Synchrotron Radiation Facility, France

This work is part of the 'APPEL' project, funded by the Netherlands Organisation for Scientific Research (NWO) and Shell. Synchrotron experiments were funded by grants acquired from DUBBLE (part of NWO) and the European Synchrotron Radiation Facility (ESRF).

Front cover artwork by: Studio Hudson, Amsterdam. studiohudson.nl
Printed by: GVO drukkers & vormgevers B.V.
Copyright © 2020 by N.J. Firet
ISBN 978-94-6384-137-5
An electronic version of this dissertation is available at repository.tudelft.nl

Or perhaps – but here I speculate, here my own curiosity leads me by the nose – the world is so arranged that when all things are learnt, when curiosity is exhausted (so, long live curiosity), that is when the world shall have come to its end.

By Graham Swift, in Waterland (1983)

I have been to the year 3000. Not much has changed but they lived under water. And your great great great granddaughter. Is pretty fine.

By Busted, The Year 3000 (2002)

Table of contents

1 Introduction and Theory 7

1.1 Introduction 8

1.2 Theory 2

1.3 Aim of this thesis and research questions 26

1.4 References 28

2 Probing the reaction mechanism of CO_2 electroreduction over Ag films via operando infrared spectroscopy 32

2.1 Foreword 33

2.2 Abstract 33

2.3 Introduction 34

2.4 Results and discussion 37

2.5 Conclusions 45

2.6 Experimental section 45

2.7 References 48

Appendix A 51

3 Operando EXAFS study reveals presence of oxygen in oxide-derived silver catalysts for electrochemical CO_2 reduction 59

3.1 Introduction 61

3.2 Results and discussion 63

3.3 Conclusions 78

3.4 References 79

Appendix B 83

4 Copper and silver gas diffusion electrodes performing CO_2 reduction studied through operando X-ray absorption spectroscopy 93

4.1 Introduction 95

4.2 Results – Guide to operando XAS on a GDE 97

4.3 Results – operando XAS on copper GDEs 103

4.4 Results – operando XAS on silver GDEs 109

4.5 Discussion 112

4.6 Conclusions 114
4.7 Experimental section 114
4.8 References 117
Appendix C 123
5 Chemisorption of anionic species from the electrolyte alters the surface electronic structure and composition of photocharged $BiVO_4$ 126
5.1 Introduction 128
5.2 Experimental section 130
5.3 Results 132
5.4 Discussion 142
5.5 Conclusions 144
References 146
Appendix D 151
6 Outlook 160
6.1 The role of science versus industry 160
6.2 Techno-economic background 161
6.3 Conclusion 163
6.4 References 164
Summary 165
Samenvatting 168
List of publications 171
Acknowledgements 172
Curriculum Vitae 174

1

Introduction and Theory

1.1 Introduction

30 years from now it will be 2050. According to the European and Dutch policy plans, the Netherlands should emit 80 to 100% less greenhouse gasses compared to 1990 by then. What does this mean? What does that world look like? You may now envision lush green landscapes filled with wind turbines and solar panels on every roof, something like the picture depicted in Figure 1.1a. In this image that is printed in your mind by graphic designers, you see a happy green economy. But when you do the math, you will soon realise that realistically, wind turbines and solar panels alone will not nearly be able to cover our energy demand. One of the main reasons for this is the type of energy these resources produce: electricity. In the world's energy mixture, electricity is only 30% of what we use. The rest of our energy usage is accounted for by fuels and materials. Fuels are needed for transport, and materials are often produced in highly energy intensive processes such as the extraction of metals from their ores or fertilizer production. Therefore we need new technologies to create renewable fuels and materials. How will we provide >733 EJ (30% more than today's energy consumption) of renewable energy of different forms on a yearly basis by 2050?[1]

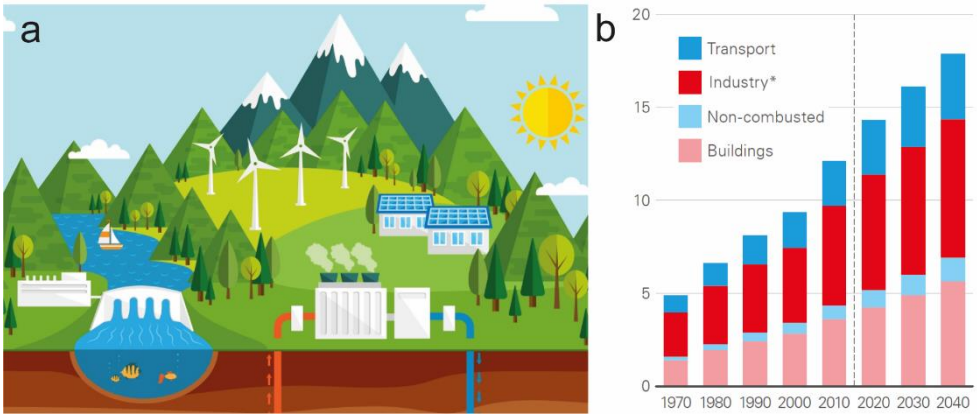

Figure 1.1. (a) Artist impression of renewable energy future.[2] (b) World primary energy demand by end-use sector in 10^9 tonnes oil equivalent (toe).[3] *Industry excludes non-combusted use of fuels.

Four end-use sectors can be classified: transport (primarily fuelled by oil), industry (production of materials), non-combusted (i.e. plastic production where oil is a precursor and not an energy source) and buildings, as shown in Figure 1.1b. Buildings include residential and commercial buildings where the main energy consumption is through electricity and consists of heating, cooling and lighting. Different from today where oil, coal and natural gas are the three primary energy carriers for all these end-use sectors, in a world based on renewable energy there will be many different types of energy carriers providing electricity, fuel, fertilizer and materials.

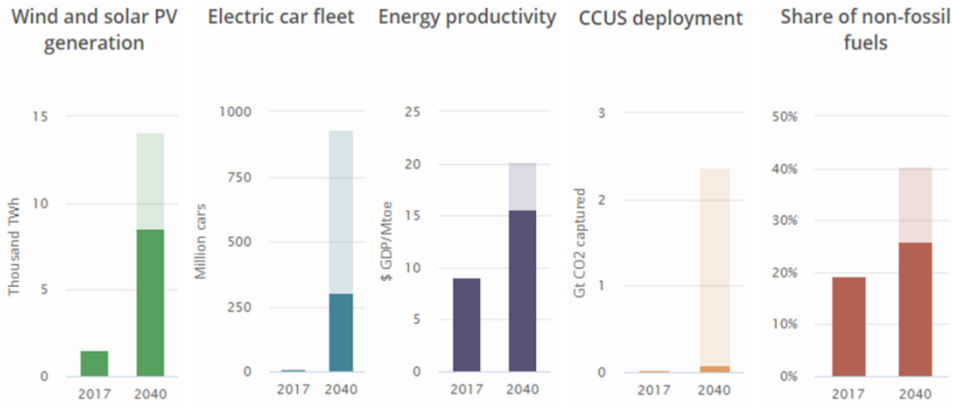

Figure 1.2. New policies scenario (solid colour) and sustainable development scenario (transparent colour) for several major renewable energy technologies, showing which technologies are expected to grow the most.[4]

Renewable electricity production from wind and solar PV is expected to increase significantly between now and 2040, which can be seen in Figure 1.2. Also, the stark difference between currently planned government policies ('New policies scenario') and the implementations needed to stop climate change ('Sustainable development scenario') is obvious. The first two graphs in Figure 1.2 point toward a strong increase in renewable electricity demand and generation, and due to the intermittent nature of renewable electricity, a strong need for energy storage has developed. Currently, the main energy storage technology is the lithium ion battery. Batteries have a limited storage capacity, are expensive, and require a lot of material, making them less sustainable for large-scale applications. Alternatively, storage through the conversion of electricity into chemical bonds via electrochemistry is an intensely investigated method. The potential large-scale application of chemical storage in molecules makes it possible to supply a constant energy output despite daily and seasonal variations in renewable electricity generation.

Electrochemistry is an old technology that has received renewed attention over the last several decades due to its potential to store (renewable) electricity into chemical bonds.[5] These bonds could be anything: they can be bonds in hydrogen, methane, ethanol, ethylene, ammonia, and more complicated molecules. Since electrochemistry is based on the transfer of electrons, it is more energy efficient to form small molecules that need relatively little extra electrons compared to the starting material. Smaller molecules can then be converted into larger molecules using thermocatalytic processes that already exist such as the Fischer-Tropsch process that converts hydrogen and carbon monoxide into hydrocarbons, as outlined in Figure 1.3.[6] Using electrochemistry, renewable electricity can be converted into the building blocks for already developed technologies that currently turn oil into different types of materials such as plastics and energy

carriers. Electrochemistry is an important technology that can supply fuels and materials, and it can serve as storage to make the current intermittent renewable electricity supply more constant.

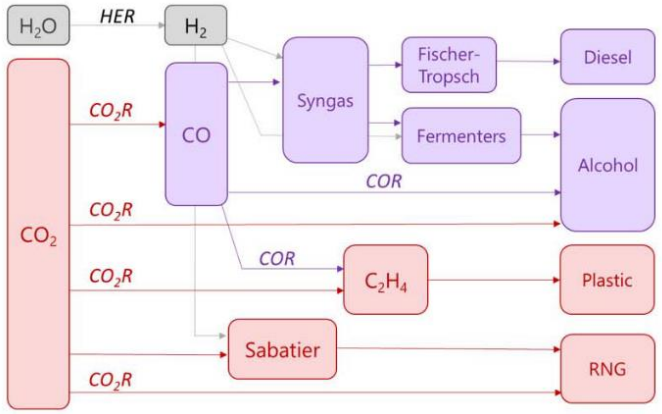

Figure 1.3. There are many possible (partly) electrochemical pathways from CO_2 and H_2O to valuable products. Reprinted from De Luna et al.[6]

1.1.1 Chapter outline

This chapter contains a theory section where the main technologies used in this thesis are explained. This includes carbon dioxide reduction, which is topic of research in most of this thesis. Then, all operando characterisation techniques used in this thesis are discussed, followed by a section on cell design for operando X-ray absorption spectroscopy studies. This chapter ends with the research questions of this thesis.

1.2 Theory

One of the main electrochemical reactions that is being studied for renewable energy purposes is the reduction of carbon dioxide (CO_2) into molecules with a higher energy content. CO_2 is the most oxidised state of carbon; by reducing it (adding electrons), it can be up converted into energetically and economically valuable chemicals.

1.2.1 CO_2 reduction

Carbon dioxide (CO_2) can be reduced to many different products. The conversion from CO_2 into carbon monoxide (CO) is one of the simpler reactions since it requires the transfer of only 2 electrons. A schematic of a CO_2 reduction system operating in alkaline conditions is shown in Figure 1.4. The half reaction that takes place at the surface of the cathode is given in equation 1.1 with its corresponding equilibrium potential versus the reversible hydrogen electrode (RHE).

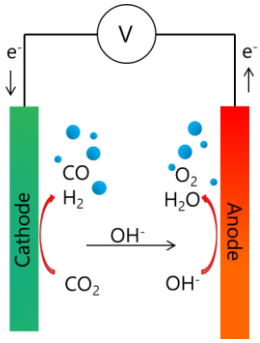

Figure 1.4. Schematic drawing of the electrochemical reduction of CO_2 to CO. The oxidation reaction of hydroxide (OH^-) into oxygen and water, and the unwanted side reaction forming hydrogen are also presented.

$CO_2 + H_2O + 2\ e^- \rightarrow CO + 2\ OH^-$	(-0.11 V)	1.1
$CO_2 + H_2O + 2\ e^- \rightarrow HCOO^- + OH^-$	(-0.03 V)	1.2
$CO_2 + 5\ H_2O + 6\ e^- \rightarrow CH_3OH + 6\ OH^-$	(0.03 V)	1.3
$CO_2 + 6\ H_2O + 8\ e^- \rightarrow CH_4 + 8\ OH^-$	(0.17 V)	1.4
$2\ CO_2 + 8\ H_2O + 12\ e^- \rightarrow C_2H_4 + 12\ OH^-$	(0.08 V)	1.5
$2\ CO_2 + 9\ H_2O + 12\ e^- \rightarrow C_2H_4 + 12\ OH^-$	(0.09 V)	1.6

Oxygen is generated at the anode as presented in equation 1.7 through the consumption of hydroxide ions (OH^-) and electrons (e^-).

$2\ OH^- \rightarrow ½\ O_2 + H_2O + 2\ e^-$	(1.23 V)	1.7

The same reactions can take place in an acidic or neutral environment, the charge carrier through the electrolyte is now a proton (H^+), in equations 1.8 and 1.9 the half reactions of the reduction of CO_2 into CO are given for neutral conditions.

$CO_2 + H_2O + 2\ e^- \rightarrow CO + 2\ OH^-$	1.8
$2\ H_2O \rightarrow ½\ O_2 + 2\ H^+ + 2\ e^-$	1.9

The evolution of hydrogen (equation 1.10) also occurs at the cathode and is an unwanted side reaction of CO_2 reduction.

$2\ H^+ + 2\ e^- \rightarrow H_2$	(0.00 V)	1.10

Apart from carbon monoxide, CO_2 reduction can result in many other products such as formic acid, methane, methanol, ethylene and ethanol, amongst others.[5,7] All these products have equilibrium potentials that lie in a narrow range from each other. The formed product is therefore not dependent on the applied potential but rather on the

used cathode. Both the type of material and its morphology impact the products that are formed.

1.2.2 Choice of cathode

The product formation depends on the electronic alignment of orbitals in the element used as the cathode since they determine how strongly the element will bind to an adsorbing molecule. Silver binds weakly to CO_2 and therefore CO_2 reduction on Ag requires an overpotential to have this adsorption occur. Once it binds to silver with the addition of a proton and an electron, it readily converts into CO through the addition of a second proton and electron, and CO is released. When the same reaction occurs on copper, the interaction between copper and CO is stronger, thus instead of releasing the CO, it can further react into C_2 molecules such as ethylene. The exact binding energy of the catalyst can be altered by changing the exposed crystal facet[8–10], introducing defect sites with dangling bonds[11] that are more likely to bind to an adsorbate or introducing dopants[12–14] that alter the electronic structure of the catalyst.

The morphology of the cathode favours certain reactions over others by influencing the local pH. This feature is mainly exploited to suppress the evolution of hydrogen. When CO_2 reduction is performed in an acidic environment, the protons can also form hydrogen. To suppress this reaction, the pH of the local environment near the cathode surface can be raised. This way, less protons are available and the reduction of CO_2 is favoured.[15,16]

To evolve CO_2 reduction into a mature technology, several factors need to be improved. The activity of the reaction should be addressed in terms of current density and required overpotential. The overpotential should be as low as possible to improve the overall energy efficiency of the process, and the current density should be as high as possible since it is a measure of the reaction rate. The selectivity of CO_2 reduction towards the desired product should be maximised to avoid downstream separation processes. Lastly, the stability of the reaction should be high: the process should be able to run for several years (>20 000 hours)[17] without deactivating the catalyst.

1.2.3 Cell design

In recent years it was found that cell design has a large impact on the cell performance. The standard H-cell design (Figure 1.5a) requires the CO_2 to be dissolved in the catholyte. Since the maximum solubility of CO_2 in water is only 34 mM, the reaction of CO_2 is strongly mass transfer limited and can reach a maximum of roughly 35 mA/cm^2 at 1 bar.[17] If instead the CO_2 can be transported to the electrode in the gas phase, like in a gas diffusion electrode (GDE) cell design (Figure 1.5b) or a membrane electrode assembly (MEA) design (Figure 1.5c), current densities of 300 mA/cm^2 and higher can be reached.[6] This is possible because the CO_2 diffusion length to reach the reaction site is drastically reduced, from around 50 μm in an H-cell to ~50 nm in a GDE cell, even

though the maximum solubility of CO_2 remains the same.[17] This configuration further allows for highly alkaline electrolytes (i.e. 1 M KOH) to also be used as an electrolyte as there exists a reaction equilibrium between CO_2 and the basic electrolyte, but it equilibriates on a slower timescale than the CO_2 reduction reactions. The reaction between CO_2 and OH^- forms bicarbonate (HCO_3^-), which can react with an additional hydroxide ion to form carbonate (CO_3^{2-}); these reactions would over time consume the electrolyte. However, as these reactions happen quite slowly, instead CO_2 can react at the catalyst surface and form the desired CO_2 reduction products. A highly alkaline electrolyte is beneficial as it favours CO_2 reduction over hydrogen evolution, and thus improves the selectivity of CO_2 reduction.

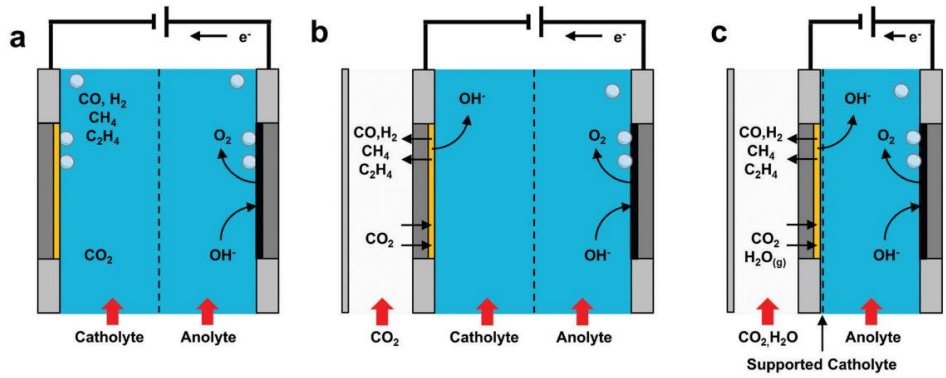

Figure 1.5. Schematic representations of (a) an H-cell design, (b) a GDE cell design for the cathode and (c) a MEA cell design for the cathode. Reprinted from Burdyny and Smith.[17]

Besides the higher current density and improved selectivity, GDE cells also decrease the overpotential required to run CO_2 reduction (due to the more favourable electrolyte 1 M KOH instead of 0.1 M $KHCO_3$ in most H-cells) and show improved stability.[18,19]

Up until now, the main focus of CO_2 reduction research has been on catalyst development and fundamental understanding. Whereas it is of paramount importance to develop stable and efficient catalysts, there are many other issues that need to be overcome for CO_2 reduction to be able to become an industrially relevant process:[6,17,20] Process integration, intermittency design, product separation technologies, long-term process stability, impact of impurities and cell design require a lot of research in the years to come.

1.2.4 Operando characterisation techniques

An electrochemical cell is a very complicated system with many variables. So in order to optimise the above mentioned operational factors, we need a thorough understanding of the reactions and processes that are happening during CO_2 reduction. In order to gain this understanding, ex situ characterisation of the catalyst before and

after CO_2 reduction and monitoring of the product output is not sufficient. Catalysts can alter their electronic and structural properties when they are transferred from an ambient pressure aqueous environment with an applied potential to a vacuum chamber, where most ex situ characterisation occurs. To account for the actual environment of the catalyst, it needs to be studied under operando conditions. There are several techniques available that allow us to study electrocatalytic reactions as they are being performed. In situ transmission electron microscopy (TEM) and in situ X-ray photoelectron spectroscopy (XPS) are able to study the catalyst size and oxidation state, respectively, albeit under low vacuum conditions and in the case of TEM, the small reactor chamber still poses many issues for electrode design and electrochemistry.[21,22] Attenuated total reflection Infrared (ATR-IR) spectroscopy can be used to study species on the surface of the catalyst under ambient pressure.[23] Raman spectroscopy can do the same and is able to probe the bonds between the catalyst and the surface species.[24,25] X-ray absorption spectroscopy (XAS) can be used to specifically study the catalyst while performing CO_2 reduction.[26] ATR-IR and XAS are used in this thesis and will be discussed further.

Attenuated total reflection infrared spectroscopy (ATR-IR). Mid-infrared radiation (2.5 – 25 μm) has the same energy as the vibrational modes of molecules and can thus be absorbed by molecules to distinguish between different functional groups, molecular symmetry, and intra- and intermolecular bonds. This makes infrared (IR) spectroscopy a very suitable technique to study chemical reactions. However, the strong absorption of water in the infrared region makes electrochemical studies in aqueous electrolytes challenging. In order to use IR spectroscopy to study reaction mechanisms in electrochemical CO_2 reduction, the path length of the IR beam through the electrolyte needs to be kept to a minimum. This can be achieved through reflectance infrared spectroscopy, where there exists a distinction between the external (Figure 1.6a) and internal (Figure 1.6b) reflection mode. In the external reflection geometry, the infrared beam leaves the IR transparent window and is reflected by a metal working electrode that is pressed against the window (Figure 1.6a). The thin (~10 μm) electrolyte layer between the window and electrode is then probed by the IR radiation. Although this electrolyte layer is extremely thin, in case an aqueous electrolyte is used, the water vibrations will still dominate the IR spectra. Therefore, instead the internal reflection mode can be adopted (Figure 1.6b).

This internal reflection geometry is called the attenuated total reflection (ATR) geometry, where the IR beam is sent through an IR-transparent crystal of a higher refractive index than the electrolyte. If the angle of incidence is higher than the critical angle, the beam is internally reflected in this crystal and an evanescent wave is created from the interference between the incoming and reflected beam at the point of reflection. The evanescent wave probes the element of lower refractive index (the electrolyte) and

its probing intensity decreases exponentially according to equation 1.11. This makes it possible to specifically study species near the ATR crystal surface.

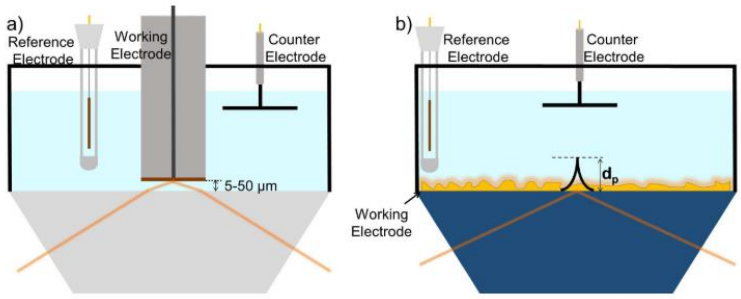

Figure 1.6. (a) External and (b) internal reflection modes for infrared experiments.

$$I = I_0 \, exp\left(\frac{-z}{d_p}\right) \qquad 1.11$$

With I the probing intensity at point z, I_0 the IR beam intensity at the interface between the crystal and the electrolyte, and d_p the penetration depth where $I = I_0/e$. The penetration depth is considered the depth that can be probed in the ATR geometry and is defined as:

$$d_p = \frac{\lambda}{2\pi n_1 \sqrt{sin^2\theta_i - (n_2/n_1)^2}} \qquad 1.12$$

Where λ is the IR wavelength, θ_i is the angle of incidence and n_1 and n_2 are the refractive indexes of the ATR crystal and the electrolyte, respectively. These equations show that the penetration depth varies with wavelength. Note that the refractive indexes also vary with wavelenght.

Through the surface enhancement of infrared absorption (SEIRA) effect, the IR absorption can be 10-1000 times more intense due to a locally formed electric field.[27,28] The local electric field is generated by the excitation of localised surface plasmons (LSPs) originating from a thin metal structure. The most commonly used method to use the SEIRA effect is the Kretschmann configuration: a 10 – 50 nm thin film with nanometre roughness deposited on the IR crystal, the island-like formation of the metal film causes the LSPs. Figure 1.7 shows how the Kretschmann configuration can be employed to study CO_2 reduction on a silver cathode. The strongest local enhancements of the SEIRA effect can be achieved by nanostructuring the metal into rods or other shapes that localise the electric field close to the surface of the catalyst.[29]

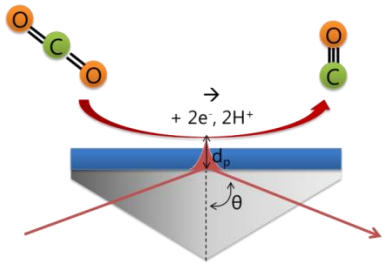

Figure 1.7. Schematic of an ATR crystal in the Kretschmann configuration. The blue film is the thin metal film needed to induce the SEIRA effect. In the current configuration it is also used as a silver working electrode to perform CO_2 reduction.

X-ray absorption spectroscopy (XAS). X-ray absorption spectroscopy probes the behaviour of photo-electrons excited by incoming X-rays absorbed by an atom's core-levels. X-rays (or photons) with the energy of the core electrons of the element of interest are absorbed by the absorber atom and excite the core electrons, causing them to scatter between the neighbouring atoms. The local environment of the absorber atom determines the X-ray absorption coefficient μ(E) and is therefore always unique. The fact that the energy of the core electron is different for every element makes this technique element specific.

The energy of the core electrons is so high (the 1s electron of silver needs to be excited by a 25515 eV X-ray), that the X-rays are capable of traveling through materials of lower elemental mass without losing much of their intensity: the technique can therefore be used under operating conditions (*operando*).

An XAS spectrum (Figure 1.8) shows the absorption coefficient as a function of incident X-ray energy and consists of a pre-edge, the absorption edge, the X-ray Absorption Near-Edge Structure **(**XANES) part and the Extended X-Ray Absorption Fine Structure (EXAFS) part. Below the absorption edge (the pre-edge part), the incoming photons do not have a high enough energy to excite the core electrons. The absorption edge is at the energy equal to the core electrons' energy. From the XANES part of the spectrum (the first 50-80 eV above the absorption edge), we can derive coordination chemistry, molecular orbitals, band-structure and multiple-scattering. However, there exists no theory that adequately describes the XANES spectrum. The interpretation is therefore based on empirical knowledge mainly derived from reference spectra, and mainly provides qualitative information. The EXAFS spectrum on the other hand (the 80 – 1000 eV above the edge), gives structural information about the probed species and can be fitted to the EXAFS equation. This makes a quantitative analysis possible, although the signal-to-noise ratio of the EXAFS is lower than that of a XANES spectrum, which can cause errors in the interpretation.

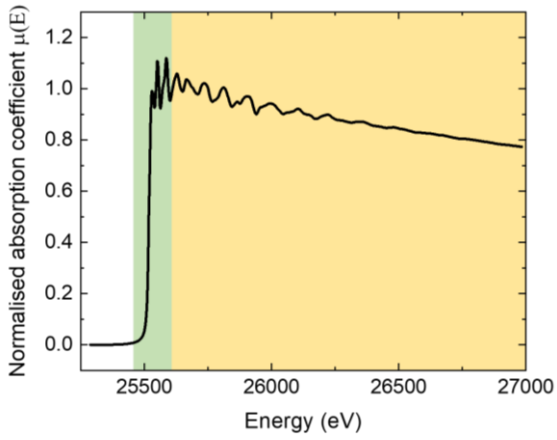

Figure 1.8. X-ray absorption spectroscopy spectrum showing the pre-edge (white background), XANES part (green background) and EXAFS part (yellow background) of the spectrum.

The notation of core-levels for XAS is denoted in absorption edges, the K edge corresponds to the 1s orbital, the L edges are the 2s (L_1), $2p_{1/2}$ (L_2) and $2p_{3/2}$ (L_3) orbitals.

X-ray Absorption Near-Edge Structure (XANES). The XANES spectrum shows core electrons that are excited from the core electron level of the absorber atom (i.e. O K-edge = O 1s) to empty states. The lowest-lying empty states are the first 'peaks' in the XANES spectrum. The peaks can be assigned using density of states (DoS) calculations and molecular orbital diagrams. For a semiconductor, the empty states are the conduction band states. When the semiconductor is a metal oxide, the conduction band consists of antibonding orbitals that are often hybridisation orbitals between the metal and the oxygen. In the case of a XANES O K-edge spectrum, the probed transition is that of O 1s to O 2p. The O 2p is often a very wide orbital hybridised with several other metal 3d or sp orbitals. The relative intensity of the peaks in the spectrum are a measure of coordination symmetry, since its type determines the e_g/t_{2g} ratio. The degree of hybridisation can be derived from the XANES spectrum since the stronger the interaction between the metal and oxygen, the more pronounced the peak in the spectrum will be. The dispersion or energy width of the orbitals can be determined from the full width half maximum (FWHM) of the peaks.

A simple approach that is often used for fast XANES analyses is to compare the spectrum of interest to reference spectra of the same element in different structural and compositional configurations such as the pure metal state and metal oxides with well-defined oxidation states. By comparing these spectra, an estimate of the oxidation state of the sample can be obtained.

A comprehensive analysis of the spectrum can be achieved by simulating the XANES. This can be valuable when several spectra of similar composition are compared and the differences between the samples need to be determined. Density functional theory (DFT) calculations can be combined with empirically determined parameters that influence the degree of ionic character (dilation of orbitals) or the degree of band broadening between the atoms. A software package to do these calculations is finite difference method near-edge structure (FDMNES).

Extended X-Ray Absorption Fine Structure (EXAFS). EXAFS treats the excitations where the photo-electrons are no longer excited to individual states, instead they are scattered between neighbouring atoms and their paths can be described by wave functions. When a photo-electron wave meets neighbouring atoms, it is scattered elastically, changing its wave-function by constructive and destructive interference.

The kinetic energy of the photo-electron is $E_{kin} = E - E_0$, where E is the incident X-ray energy and E_0 the excitation energy of the absorber atom's core-level (Figure 1.9). E is varied during the experiment, since E_0 is fixed, E_{kin} will also vary and so will the wavelength λ and the wavenumber k of the photo-electron. As λ varies, the outgoing and backscattered waves will interfere constructively or destructively, also dependent on the distance R between the absorber atom and its neighbour (Figure 1.9). The interference determines the shape of the absorption coefficient μ(E), which is the probability of the incident X-ray being absorbed by the probed material.

To analyse the EXAFS data, one first has to convert the absorption coefficient data μ(E) (Figure 1.10a) to χ(k) (Figure 1.10b), which are the oscillations χ as a function of the photo-electron wavenumber k (equation 1.13 and 1.14).

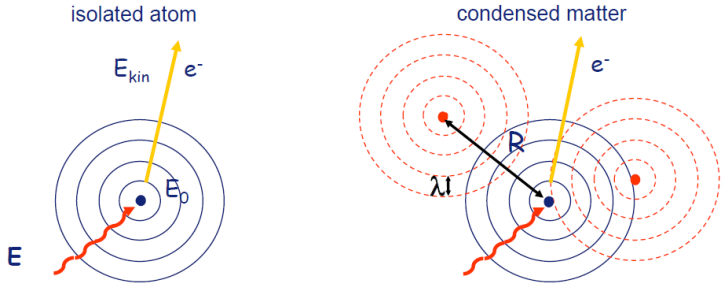

Figure 1.9. An isolated absorber atom (left) and an absorber atom surrounded by other atoms (right) are shown. The incident X-ray (E) excites photo-electron e^- with energy E_0 and the excess kinetic energy E_{kin} is transferred to the photo-electron.[30]

$$\chi(E) = \frac{\mu(E) - \mu_0(E)}{\Delta\mu_0(E)} \quad 1.13$$

$$k = \sqrt{\frac{2m(E - E_0)}{\hbar^2}} \quad 1.14$$

In equation 1.13, μ(E) is the measured absorption coefficient and $\mu_0(E)$ is the theoretical absorption coefficient for one isolated atom. $\Delta\mu_0$ is the adsorption edge step, so the difference in μ between the pre-edge and the absorption signal. Wavenumber k in equation 1.14 is a function of the mass of an electron (m), the incident X-ray energy (E) and the absorption edge energy (E_0).

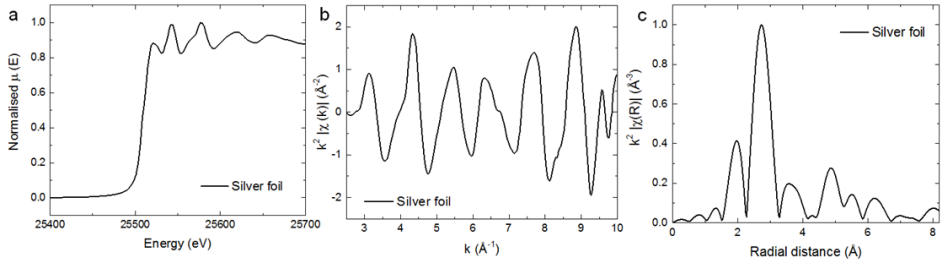

Figure 1.10. (a) Normalised absorption coefficient μ(E), (b) k^2-weighted χ(k) and (c) the Fourier transformed k^2-weighted χ(k) of a silver foil.

The different contributions to χ(k) are frequencies of different types of oscillators. For example, in a silver oxide, the Ag-O frequency oscillates differently than the Ag-Ag frequency. The EXAFS equation can be fitted to χ(k) and is in fact a summation of these different frequencies that all have their own interatomic distance (R), coordination number (N) (a measure of the amount) and Debye-Waller factor (σ^2) (equation 1.15). σ^2 is the distance variance of the absorber-scatterer distance, and is affected by the different distances between the absorber atom and the various scattering atoms. There is a thermal and a structural disorder component present in the Debye-Waller factor. The thermal component is temperature dependent but the structural disorder is sample-specific and can be used to gain information about the amount of disorder within a sample.

$$\chi(k) = \sum_i \frac{N_i f_i(k) e^{-2k^2\sigma_i^2}}{kR_i^2} \sin[2kR_i + \delta_i(k)] \quad 1.15$$

The scattering amplitude (f) and the phase-shift (δ) are known values for standard components and can be entered into the fitting equation to generate values for R, N and σ^2. f and δ depend on the type of scatterer but only weakly, therefore two atoms that are quite similar in atomic weight (i.e. O and C) cannot be distinguished using their amplitude and phase-shifts.

The EXAFS oscillations diminish quickly at larger distances from the absorber atom; to retain a clear signal, χ(k) can be multiplied with a factor k^2 or k^3. For a pure metal, the different oscillations are different shells around the absorber atom: silver atoms at various distances within the same unit cell. For an oxide, some shells are Ag-O contributions and others are Ag-Ag. The Fourier Transform (FT) of χ(k) gives a spectrum that is easier to interpret by eye compared to the χ(k) spectrum (Figure 1.10c). The x-axis now displays the distance between the absorber atom and the neighbouring shells, the y-axis is a measure of the intensity.

XAS can be measured in transmission mode or in fluorescence mode. Transmission mode is the most direct, where the absorption coefficient is related to the incoming intensity I_0 and the outgoing intensity I according to equation 1.16, where t is the sample thickness and μ is the attenuation coefficient of the absorber material. The exact meaning of μ is discussed in more detail in Section 1.2.5. The fluorescence signal can be used to measure the XAS as well. However, its signal is not determined by a direct change in X-ray intensity. Instead, the relaxation of the core-hole (created when the photo-electron was excited) occurs when a higher level core electron drops to fill the core-hole. This process emits the excess energy in the form of a fluorescent X-ray and $\mu(E) \sim I_F/I_0$.

$$I = I_o e^{\mu t} \qquad 1.16$$

Self-absorption is an unavoidable side effect of measuring in fluorescence mode. The fluorescence intensity is a function of the total absorption. The absorption of the element of interest changes with energy in the energy range of interest. If a sample is quite thick, and $\mu_{absorber}$ is not << $\mu_{background}$, the resulting signal in the XAS spectrum is dampened. Self-absorption has a large effect on the coordination number because the intensity of the signal is affected.[31] However, the bond distance is not affected since no phase shifts occur as a result of self-absorption. XAS data analysis software often contains tools to correct for self-absorption effects, although it is hard to obtain a perfect correction when there is no transmission spectrum of the same sample available. It therefore remains difficult to retrieve correct absolute coordination number values from EXAFS fits even after a self-absorption correction has been applied. However, relative coordination numbers of similar samples in the same cell design can be extracted. The best method to avoid self-absorption is to use a sufficiently thin sample, below ~5 μm. Lower atomic number (Z) elements are also less affected by self-absorption.

X-ray Raman scattering (XRS). X-ray Raman scattering can be used to study soft X-ray (<10^3 eV) edges under ambient pressure and into the bulk of the sample.[32] XRS is a part of a non-resonant inelastic X-ray scattering (NRIXS) experiment where high energy X-rays are scattered. The energy $\omega = \omega_1 - \omega_2$ and momentum $q = k_1 - k_2$ are transferred to the studied system. ω_1 and k1 are the energy and momentum of the incident photons, and ω_2 and k_2 of the scattered photons (Figure 1.11). If the transferred energy ω has the energy of a core-level of the studied material and q is of a sufficiently low angle, the X-ray Raman scattering gives the same information as the X-ray absorption spectrum.[33]

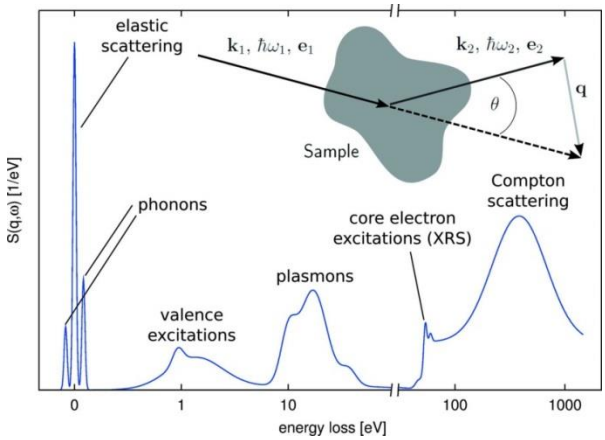

Figure 1.11. NRIXS spectrum showing all the different electronic excitations that can be measured from an inelastic scattering experiment.[34]

The XRS spectrum is denoted in energy loss, it is lost from the incoming ω_1. Since only a small percentage of the incoming photons will result in inelastic scattering events and an even smaller percentage has the right energy to excite the element of interest, the overall intensity of an XRS experiment is low and the signal-to-noise ratio is high. X-ray Raman scattering has a much lower intensity than standard XAS experiments and therefore needs a very large X-ray flux and very sensitive detectors compared to normal XAS. Data analysis for XRS experiments is still in the developing phase, background subtraction is not straightforward and the data often gives a XANES-type spectrum, where data cannot directly be related to a physical formula.[34]

The advantage of XRS is that it can use high energy X-rays to probe soft energy edges, such as the oxygen and the carbon K edge. Due to its inherent low energy X-ray source, soft X-ray XAS has to be performed under vacuum and the low energy X-rays have a small penetration depth, making the technique only suitable for surface studies.

1.2.5 Cell design for electrochemical operando studies

Operando spectroscopic studies are often highly individual for their research aims. This makes the demands to the cell design in many cases also unique. For electrochemical operando XAS studies, a number of cell designs exist that, when compared to each other, can provide a useful set of design rules that will benefit future studies.

Hard X-rays ($E>10^3$ eV) offer a unique possibility for operando studies. The higher energy is not absorbed by many light materials such as carbon or oxygen, offering the possibility to create cells that encase the sample of interest with a wider variety of materials. Synchrotrons also offer a very high flux compared to conventional X-ray characterisation techniques, improving the signal-to-noise ratio even more. The penetration depth of X-rays depends on the energy of the incident beam and the materials that have to be crossed before entering the material of interest.

When adding additional cell components it is important to understand the relation between X-ray beam intensity and its attenuating properties, shown in equation 1.16.[35] When the X-rays pass through several materials, their absorption coefficients and thicknesses should all be taken into account by a summation of equation 1.16. The attenuation coefficient μ is then the sum of the absorption coefficient and the scattering coefficient, and can be found through the mass attenuation coefficient (μ/ρ, where ρ is the density of the absorber material), which is a tabulated value. From the tabulated values it follows that higher Z absorber materials decrease the beam intensity. Equation 1.16 also predicts that when the X-ray beam passes through a thick sample, it will have a lower intensity I. This means that when the angle of incidence is very shallow and the beam path length through the material is thus increased, the beam intensity decreases significantly. The centre for X-ray optics has a database that includes all relevant tabulated values. It also provides calculators for the transmission of X-rays through solids and gasses and allows to calculate the attenuation length through a specified material as a function of X-ray energy and angle of incidence.[36] These calculators are very important to help assess whether a certain cell design will allow for a high enough XAS yield.

The most simple cell design for a cell enabling operando XAS experiments, is a single reactor tube of any material with a window cut out where the electrode of interest is mounted. The sample is covered by Kapton tape to avoid leaking. The measurements are performed in a fluorescence geometry where there is a 45° angle between the X-ray beam source and the sample, and a 45° angle between the sample and the fluorescence detector. All cells that are discussed in this section are measured in fluorescence mode, unless specified otherwise.

Soft X-rays ($<10^3$ eV) are only suitable for operando applications in certain configurations. Since they probe the K edge of carbon and oxygen, their application in

operando studies is desirable. Velasco-Velez, Salmeron et al. designed an electrochemical cell (Figure 1.12) to study the O K edge using a Si_3N_4 membrane that separated the cell from a vacuum needed to improve the signal.[37] On the membrane, a 20 nm gold electrode was deposited. This allowed the ability to study the orientation of water molecules facing the gold electrode by sending the X-rays through the vacuum, membrane, gold and water layers consecutively.

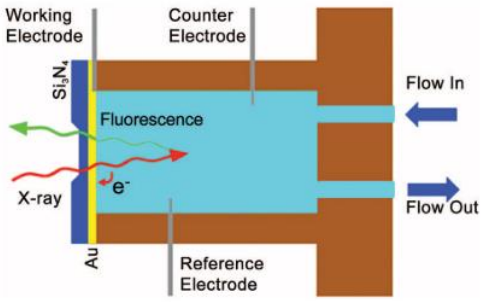

Figure 1.12. Lay-out of the Salmeron cell, suitable for operando electrochemical studies where soft edges are studied. Reprinted from Velasco-Velez et al.[37]

The same cell was later employed to study CO_2 reduction on copper electrodes.[38] The flow cell design is necessary to ensure unobstructed electrochemistry. The drawback of the Salmeron cell design is that when the electrode rather than the electrolyte is to be studied, the X-rays need to enter the electrode through its back-side. This implies that the probed area is mostly the back-side of the electrode, whereas electrochemistry, and thus the part of the electrode of interest, is on the front-side: the electrode/electrolyte interface. Besides this, the electrode has to be very thin in order for the X-rays to probe the entire thickness of the sample. Instead, a cell design where the X-rays enter through the front could be used.

A front design was developed by Trześniewski et al., to study both NiOOH and $BiVO_4$ as oxygen evolution catalysts (Figure 1.13).[39,40] To ensure that the X-rays can reach the electrode through the electrolyte, the electrolyte layer needs to be kept very thin. In the case of $BiVO_4$, the vanadium K-edge (9 keV) was studied through a Kapton window and an electrolyte layer of ~30 µm. The electrolyte channel was made by Kapton tape.

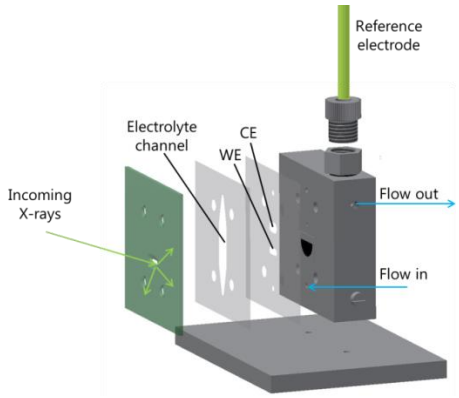

Figure 1.13. The Trześniewski cell is designed so that X-rays penetrate the sample after passing through a window and a thin electrolyte layer at the front of the cell.

The Trześniewski front design cell addresses the issue of sample substrate flexibility: since the X-rays enter through the front, the sample substrate can be made of anything, thick glass or metal foil substrates can be used. However, the X-rays will still penetrate deeper into the sample than solely the region of interest, namely the electrode/electrolyte interface. In order to ensure surface sensitivity, the incident beam angle can be adjusted. A low angle of incidence ensures shallow penetration of the substrate. However, it does pose a problem for the cell design. With a sandwich design where window, electrolyte and electrode are simply stacked on top of each other and the beam passes all layers, such as in the Trześniewski design, the beam path length will increase with decreasing angle of incidence according to Pythagoras' theorem. The longer the beam path length, the more intensity the beam will lose, both entering and leaving the electrochemical cell. Also, positioning can become very tricky to ensure the beam eventually hits the sample when the sample is small in the beam direction dimension.

To overcome these issues, Farmand et al., recently demonstrated the design of a dome-shaped electrolyte channel (Figure 1.14).[41] In this design, the X-ray beam still passes the window and electrolyte before reaching the electrode, but their distance to the electrode is now constant at every angle of incidence. Extremely low angles of incidence of up to 0.1° can be reached with this cell design. The drawback is the complicated design. To ensure this constant path length at all angles, mounting the cell is a very time consuming process and once a sample is mounted it cannot be taken apart, i.e. it is a single-use cell. This greatly diminishes the range of possibilities for this cell since more intricate electrode designs often require replacement to ensure the sample is fresh and not contaminated or restructured by high cell voltages.

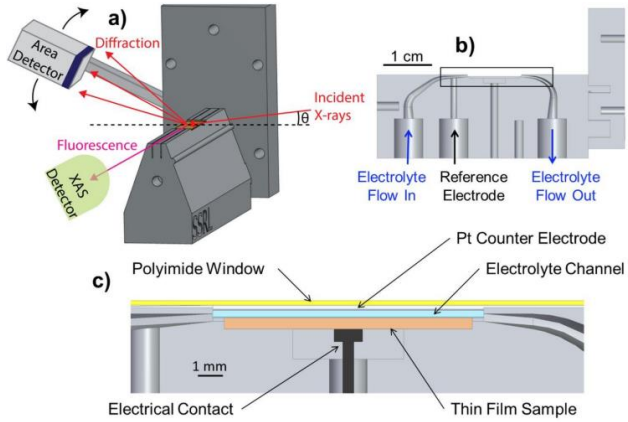

Figure 1.14. The Farmand cell facilitates low angles of incidence to ensure surface-sensitive XAS spectra while maintaining a flow cell design with good electrochemistry. Reprinted from Farmand et al.[41]

Firet et al. designed a shallow incidence cell that facilitates sample replacement (Figure 1.15). The cell has a flow cell design and ensures the ability to take front-side measurements. A drawback is the minimum angle of incidence, 6°. For a nanostructured silver cathode this is acceptable, since at 6° a penetration depth of a few microns can be reached, and a nanostructured sample often has a roughness of similar dimension.

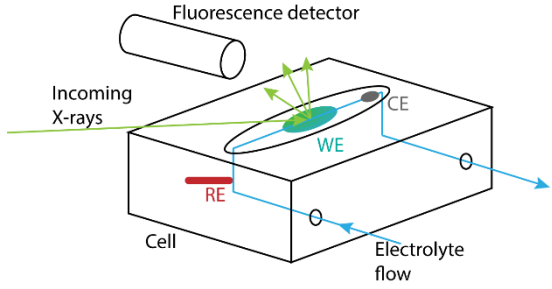

Figure 1.15. The Firet cell combines user-friendliness and surface-sensitive front-illumination in a flow cell design.[42]

For some experiments it is possible to measure in transmission mode, rather than in fluorescence mode.[43] In transmission mode the outgoing X-ray signal is collected behind the sample, there is a 180° angle between the incident X-ray beam and the outgoing signal. This means that the catalyst, its substrate, the electrolyte and the cell casing need to be very thin to allow the X-ray beam to pass all these layers. Since this is often not possible, fluorescence mode is the most widely used for operando XAS experiments.

The above-mentioned cell designs offer some design rules that should be followed when deciding on the most adequate cell configuration for a specific experiment. First of all, the type of sample should be considered to determine whether the experiment has to be surface sensitive or not. Then, depending on the sample thickness, front- or back-irradiation has to be selected. The type of element that is studied determines whether hard X-rays are possible, which allow some flexibility in cell design. If light elements such as oxygen or carbon are studied, soft X-rays are required, and the cell should be designed without any cell parts in the way of the X-ray beam. A vacuum then has to be applied between the X-ray source and the sample. In most cases, a flow cell design is desired, both to improve the electrochemistry and to avoid beam radiation damage to the electrolyte. A chart was composed based on these previous results and analysis, in order to determine which cell design is most suitable for a particular electrochemical operando XAS experiment (Figure 1.16).

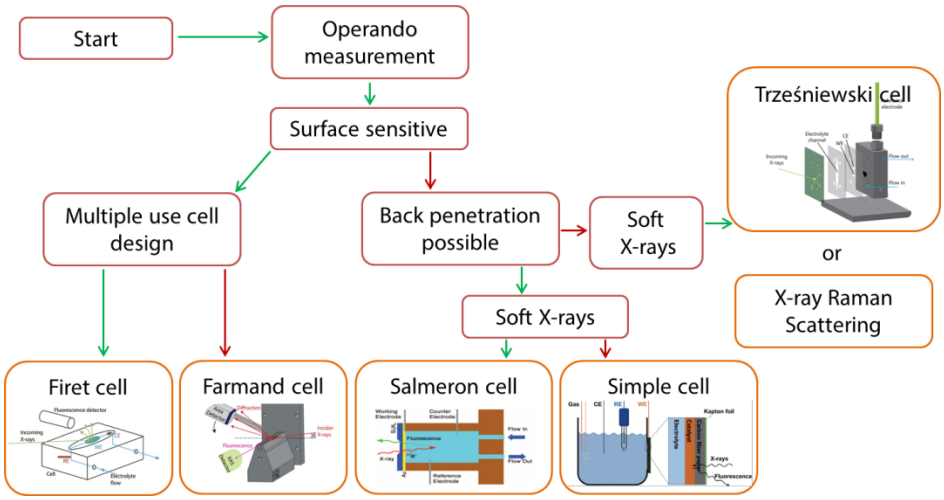

Figure 1.16. Follow the cell design decision making scheme to determine which cell design suits your experiment, where a green arrow indicates yes and a red arrow no.

1.3 Aim of this thesis and research questions

The aim of this thesis is to combine operando characterisation techniques and electrochemistry in order to improve the existing fundamental knowledge on electrochemical processes. Two important electrochemical processes were investigated in this study, CO_2 reduction and solar water splitting. The first part of this thesis (Chapter 2, 3 and 4) deals with studying CO_2 reduction. In Chapter 2, the reaction mechanism on a silver cathode is studied using SEIRA ATR-FTIR. Chapter 3 explores the use of a grazing-incidence cell design used to study the surface of an oxide-derived silver cathode with XAS. The presence of oxygen was studied in this work using EXAFS. For GDE cells, a new cell design was designed and discussed in Chapter 4. Both copper

and silver films sputtered on GDEs were evaluated as CO_2 reduction cathodes in this work.

The second part of the thesis studies $BiVO_4$, a photoanode used for photoelectrochemical (PEC) water splitting into hydrogen and oxygen using sunlight. In Chapter 5, XRS is used to study the electronic effects of photocharging on bismuth vanadate ($BiVO_4$). The oxygen K edge and vanadium L_2 and L_3 edges were studied using XRS rather than XAS since XAS would require vacuum conditions to study such light elements. Measuring under operando conditions was not possible in this work, but valuable insights were gained that can aid in future PEC cell design.

1.3.1 Research questions

How can we use existing operando characterisation techniques to study electrochemical systems?

- How does the reaction mechanism of CO_2 reduction on a silver cathode change as a function of applied potential?
- How can XAS, a bulk technique, be used to study the surface of a nanoporous silver catalyst during CO_2 reduction?
- Is there oxygen present in oxide-derived silver during CO_2 reduction and if so, what is its role in the reaction?
- What is a practical design for a spectro-electrochemical cell for XAS studies on GDEs?
- How does the structure of copper and silver GDEs change as a function of applied current density, catalyst thickness and electrolyte type?
- What is the electronic effect of photocharging on bismuth vanadate?

1.4 References

(1) https://www.iea.org/weo/.

(2) https://thefederalist.com/2015/11/20/great-news-americans-dont-really-care-about-climate-change/.

(3) BP. BP Energy Outlook 2019 Edition; 2019.

(4) https://www.iea.org/weo2018/scenarios/.

(5) Hori, Y. Electrochemical CO2 Reduction on Metal Electrodes. In Modern Aspects of Electrochemistry No. 42; Vayenas, C. G., Gamboa-Aldeco, M. E., White, R. E., Eds.; Springer: New York, 2008; pp 89–189.

(6) De Luna, P.; Hahn, C.; Higgins, D.; Jaffer, S. A.; Jaramillo, T. F.; Sargent, E. H. What Would It Take for Renewably Powered Electrosynthesis to Displace Petrochemical Processes? Science (80-.). 2019, 364, 3506.

(7) Kuhl, K. P.; Hatsukade, T.; Cave, E. R.; Abram, D. N.; Kibsgaard, J.; Jaramillo, T. F. Electrocatalytic Conversion of Carbon Dioxide to Methane and Methanol on Transition Metal Surfaces. J. Am. Chem. Soc. 2014, 136, 14107–14113.

(8) Hoshi, N.; Kato, M.; Hori, Y. Electrochemical Reduction of CO2 on Single Crystal Electrodes of Silver. J. Electroanal. Chem. 1997, 440, 283–286.

(9) Lee, H. E.; Yang, K. D.; Yoon, S. M.; Ahn, H. Y.; Lee, Y. Y.; Chang, H.; Jeong, D. H.; Lee, Y. S.; Kim, M. Y.; Nam, K. T. Concave Rhombic Dodecahedral Au Nanocatalyst with Multiple High-Index Facets for CO2 Reduction. ACS Nano 2015, 9, 8384–8393.

(10) Huang, Y.; Handoko, A. D.; Hirunsit, P.; Yeo, B. S. Electrochemical Reduction of CO 2 Using Copper Single-Crystal Surfaces: Effects of CO* Coverage on the Selective Formation of Ethylene. ACS Catal. 2017, No. 100, 1749–1756.

(11) Mistry, H.; Choi, Y.-W.; Bagger, A.; Scholten, F.; Bonifacio, C.; Sinev, I.; Divins, N. J.; Zegkinoglou, I.; Jeon, H. S.; Kisslinger, K.; et al. Enhanced Carbon Dioxide Electroreduction to Carbon Monoxide over Defect Rich Plasma-Activated Silver Catalysts. Angew. Chemie Int. Ed. 2017, 56, 1–6.

(12) Lim, H. K.; Shin, H.; Goddard, W. A.; Hwang, Y. J.; Min, B. K.; Kim, H. Embedding Covalency into Metal Catalysts for Efficient Electrochemical Conversion of CO2. J. Am. Chem. Soc. 2014, 136 (32), 11355–11361.

(13) Kim, C.; Jeon, H. S.; Eom, T.; Jee, M. S.; Kim, H.; Friend, C. M.; Min, B. K.; Hwang, Y. J. Achieving Selective and Efficient Electrocatalytic Activity for CO2 Reduction Using Immobilised Silver Nanoparticles. J. Am. Chem. Soc. 2015.

(14) Zhou, Y.; Che, F.; Liu, M.; Zou, C.; Liang, Z.; Yuan, H.; Li, J.; Wang, Z.; Luna, P. De; Yuan, H.; et al. Dopant-Induced Electron Localization Drives CO2 Reduction to C2 Hydrocarbons. Nat. Chem. 2018, 1–20.

(15) Yoon, Y.; Hall, A. S.; Surendranath, Y. Tuning of Silver Catalyst Mesostructure Promotes Selective Carbon Dioxide Conversion into Fuels. Angew. Chemie - Int. Ed. 2016, 128, 15508–15512.

(16) Ma, M.; Trzesniewski, B. J.; Xie, J.; Smith, W. A. Selective and Efficient Reduction of Carbon Dioxide to Carbon Monoxide on Oxide-Derived Nanostructured Silver Electrocatalysts. Angew. Chemie - Int. Ed. 2016, 55, 9748–9752.

(17) Burdyny, T.; Smith, W. A. CO 2 Reduction on Gas-Diffusion Electrodes and Why Catalytic Performance Must Be Assessed at Commercially-Relevant Conditions. Energy Environ. Sci. 2019, Advance Ar.

(18) Gabardo, C. M.; Seifitokaldani, A.; Edwards, J. P.; Dinh, C.-T.; Burdyny, T.; Kibria, M. G.; O'Brien, C. P.; Sargent, E. H.; Sinton, D. Combined High Alkalinity and Pressurization Enable Efficient CO 2 Electroreduction to CO. Energy Environ. Sci. 2018, 11, 2531–2539.

(19) Verma, S.; Lu, X.; Ma, S.; Masel, R. I.; Kenis, P. J. A. The Effect of Electrolyte Composition on the Electroreduction of CO2 to CO on Ag Based Gas Diffusion Electrodes. Phys. Chem. Chem. Phys. 2015, 18, 7075–7084.

(20) Higgins, D.; Hahn, C.; Xiang, C.; Jaramillo, T. F.; Weber, A. Z. Gas-Diffusion Electrodes for Carbon Dioxide Reduction: A New Paradigm. ACS Energy Lett. 2019, 4, 317–324.

(21) Handoko, A. D.; Wei, F.; Jenndy; Yeo, B. S.; Seh, Z. W. Understanding Heterogeneous Electrocatalytic Carbon Dioxide Reduction through Operando Techniques. Nat. Catal. 2018, 1, 922–934.

(22) Gao, D.; Zegkinoglou, I.; Divins, N. J.; Scholten, F.; Sinev, I.; Grosse, P.; Roldan Cuenya, B. Plasma-Activated Copper Nanocube Catalysts for Efficient Carbon Dioxide Electroreduction to Hydrocarbons and Alcohols. ACS Nano 2017, 11, 4825–4831.

(23) Baruch, M. F.; Pander, J.; White, J. L.; Bocarsly, A. B. Mechanistic Insights into the Reduction of CO2 on Tin Electrodes Using In Situ ATR-IR Spectroscopy. ACS Catal. 2015, 150413134326004.

(24) Bohra, D.; Ledezma-Yanez, I.; Li, G.; de Jong, W.; Pidko, E. A.; Smith, W. A. Lateral Adsorbate Interactions Inhibit HCOO − While Promoting CO Selectivity for CO 2 Electrocatalysis on Silver. Angew. Chemie - Int. Ed. 2019, 58 (5), 1345–1349.

(25) Mahoney, M. R.; Howard, M. W.; Cooney, R. P. Carbon Dioxide Conversion to Hydrocarbons at Silver Electrode Surfaces. Chem. Phys. Lett. 1980, 71, 59–63.

(26) Rosen, J.; Hutchings, G. S.; Lu, Q.; Forest, R. V.; Moore, A.; Jiao, F. Electrodeposited Zn Dendrites with Enhanced CO Selectivity for Electrocatalytic CO 2 Reduction. ACS Catal. 2015, 5, 4586–4591.

(27) Osawa, M.; Ataka, K. ichi; Yoshii, K.; Yotsuyanagi, T. Surface-Enhanced Infrared ATR Spectroscopy for in Situ Studies of Electrode/Electrolyte Interfaces. J. Electron Spectros. Relat. Phenomena 1993, 64–65, 371–379.

(28) Osawa, M. Surface-Enhanced Infrared Absorption. In Near-Field Optics and Surface Plasmon Polaritons; 2001; Vol. 81, pp 163–187.

(29) Neubrech, F.; Huck, C.; Weber, K.; Pucci, A.; Giessen, H. Surface-Enhanced Infrared Spectroscopy Using Resonant Nanoantennas. Chem. Rev. 2017, 117, 5110–5145.

(30) Pascarelli, S. X-Ray Absorption Spectroscopy: Fundamentals and Simple Model of EXAFS. European Synchrotron Radiation Facility 2016.

(31) Tröger, L.; Arvanitis, D.; Baberschke, K.; Michaelis, H.; Grimm, U.; Zschech, E. Full Correction of the Self-Absorption in Soft-Fluorescence Extended x-Ray-Absorption Fine Structure. Phys. Rev. B 1992, 46, 3283–3289.

(32) Sahle, C. J.; Mirone, A.; Niskanen, J.; Inkinen, J.; Krisch, M.; Huotari, S. Planning, Performing and Analyzing X-Ray Raman Scattering Experiments. J. Synchrotron Radiat. 2015, 22, 400–409.

(33) Tohji, K.; Udagawa, Y. Novel Approach for Structure Analysis by X-Ray Raman Scattering Kazuyuki. Phys. Rev. B 1987, 36 (17), 9410–9412.

(34) Sahle, C. J.; Mirone, A.; Vincent, T.; Kallonen, A.; Huotari, S. Improving the Spatial and Statistical Accuracy in X-Ray Raman Scattering Based Direct Tomography. J. Synchrotron Radiat. 2017, 24 (2), 476–481.

(35) Henke, B. L.; Gullikson, E. M.; Davis, J. C. X-Ray Interactions: Photoabsorption, Scattering, Transmission, and Reflection at E = 50-30, 000 EV, Z = 1-92. At. Data Nucl. Data Tables 1993, 54, 181–342.

(36) Gullikson, E. M. http://henke.lbl.gov/optical_constants/.

(37) Velasco-Velez, J.-J.; Pascal, T. A.; Wan, L. F.; Guo, J.; Prendergast, D.; Salmeron, M. The Structure of Interfacial Water on Gold Electrodes Studied by X-Ray Absorption Spectroscopy. Science (80-.). 2014, 346, 831–834.

(38) Velasco-Vélez, J. J.; Jones, T.; Gao, D.; Carbonio, E.; Arrigo, R.; Hsu, C. J.; Huang, Y. C.; Dong, C. L.; Chen, J. M.; Lee, J. F.; et al. The Role of the Copper Oxidation State in the Electrocatalytic Reduction of CO2 into Valuable Hydrocarbons. ACS Sustain. Chem. Eng. 2019, 7 (1), 1485–1492.

(39) Trześniewski, B. J.; Diaz-Morales, O.; Vermaas, D. A.; Longo, A.; Bras, W.; Koper, M. T. M.; Smith, W. A. In Situ Observation of Active Oxygen Species in Fe-Containing Ni-Based Oxygen Evolution Catalysts: The Effect of PH on Electrochemical Activity. J. Am. Chem. Soc. 2015, 137 (48), 15112–15121.

(40) Trześniewski, B. J.; Digdaya, I. A.; Nagaki, T.; Ravishankar, S.; Herraiz-Cardona, I.; Vermaas, D. A.; Longo, A.; Gimenez, S.; Smith, W. A. Near-Complete Suppression of Surface Losses and Total Internal Quantum Efficiency in BiVO 4 Photoanodes. Energy Environ. Sci. 2017, 10, 1517–1529.

(41) Farmand, M.; Landers, A. T.; Lin, J. C.; Feaster, J. T.; Beeman, J. W.; Ye, Y.; Clark, E. L.; Higgins, D.; Yano, J.; Davis, R. C.; et al. Electrochemical Flow Cell Enabling: Operando Probing of Electrocatalyst Surfaces by X-Ray Spectroscopy and Diffraction. Phys. Chem. Chem. Phys. 2019, 21 (10), 5402–5408.

(42) Firet, N. J.; Blommaert, M. A.; Burdyny, T.; Venugopal, A.; Bohra, D.; Longo, A.; Smith, W. A. Operando EXAFS Study Reveals Presence of Oxygen in Oxide-Derived Silver Catalysts for Electrochemical CO 2 Reduction. J. Mater. Chem. A 2019, 7, 2597–2607.

(43) Binninger, T.; Fabbri, E.; Patru, A.; Garganourakis, M.; Han, J.; Abbott, D. F.; Sereda, O.; Kötz, R.; Menzel, A.; Nachtegaal, M.; et al. Electrochemical Flow-Cell Setup for In Situ X-Ray Investigations. J. Electrochem. Soc. 2016, 163 (10), H906–H912.

2

Probing the reaction mechanism of CO_2 electroreduction over Ag films via operando infrared spectroscopy

This chapter is based on the following publication:

N.J. Firet, W.A. Smith. Probing the reaction mechanism of CO_2 electroreduction over Ag films via operando infrared spectroscopy. ACS Catal. 2017, 7, 606−612

2.1 Foreword

The following chapter was published in late 2016 after a peer-review process with ACS Catalysis. We later co-authored a review paper on operando infrared spectroscopy which discussed some of the potential errors in the current work. We chose to keep this chapter largely the same as the original publication because it is in the nature of science to always change insights. In the words of Jules Verne: 'Science, my boy, is composed of errors, but errors that it is right to make, for they lead step by step towards the truth.' (From: Journey to the centre of the earth, 1864).

The conclusion of the chapter that the reaction mechanism of lower applied potential is different than at higher applied potential still stands since the spectra are different. The exact differences between these mechanisms could be in the configuration of bicarbonate molecules or the presence of a formate intermediate, but this was not investigated further at the time this study came out.

2.2 Abstract

The electrocatalytic reduction of CO_2 to chemical fuels has attracted significant attention in recent years. Amongst transition metals, silver shows one of the highest faradaic efficiencies for CO formation as the main reaction product, however the exact mechanism for this conversion is not fully understood. In this work, we study the reaction mechanism of silver as a CO_2 reduction catalyst using in situ Attenuated Total Reflection Fourier Transform Infrared spectroscopy (ATR-FTIR) during electrochemical cycling. Using ATR-FTIR it is possible to observe the reaction intermediates on the surface of Ag thin films formed during the CO_2 electroreduction reaction. At a moderate overpotential, a proton coupled electron transfer reaction mechanism is confirmed to be the dominant CO_2 reduction pathway. However, at a more negative applied potential, both the COO^- and the COOH intermediate are detected using ATR-FTIR, which indicates that individual proton and electron transfer steps occur, offering a different pathway than at lower potentials. These results indicate that the CO_2 reduction reaction mechanism can be potential dependent and not always involving a concerted proton coupled electron transfer, opening alternative pathways to optimise efficient and selective catalysts for desired product formation.

2.3 Introduction

There is an immediate need to develop CO_2-neutral energy technologies to replace fossil fuels. One of the most attractive solutions is to store renewable energy in the form of a chemical fuel made from abundant resources.[1,2] Synthetic fuels can be made using electricity from a renewable energy source, such as solar and wind, to electrochemically reduce water and CO_2. This process forms high energy density compounds that can either be directly used as fuels (methanol and methane), or as fuel precursors such as synthesis gas ($CO + H_2$). A suitable catalyst that is stable, active and selective for a specific product is needed for this process. Most of the transition metals studied for CO_2 electroreduction show a preferred product formation for either hydrogen (Ni, Fe, Pt and Ti), carbon monoxide (Au, Ag, Zn, Pd and Ga) or formic acid (Pb, Hg, Tl, In, Sn and Cd).[3] Copper is an exception as it forms up to 18 different compounds including complex hydrocarbons.[4] While the reaction products formed on certain metals are well known, the reaction pathways to form the products are not understood as clearly. It is essential to understand the reaction mechanism in order to find ways to optimise catalysts to form specific products. Specifically, it is vital to know which intermediates are present on a given catalyst surface during the reaction, especially under operational conditions.

To provide a solid platform to study the reaction intermediates of CO_2 conversion, it is useful to observe a catalyst that is not only selective, but also stable during electrochemical testing. Ag is an ideal material to study as a catalytic surface since it is known to produce mainly CO with small amounts of hydrogen and formic acid as by products.[5] The reaction pathway of the electrochemical reduction of CO_2 to CO on silver electrodes has been proposed to consist of either three or four elementary reaction steps, as outlined in equations 2.1-2.5. In the first reaction step, CO_2 adsorbs to the metal surface in the form of COOH* (equation 2.1).

$$CO_2(g) + * + H^+(aq) + e^- \leftrightarrow COOH* \qquad 2.1$$

According to Kortlever et al.[6] this step occurs either as a proton coupled electron transfer (PCET), as shown in equation 2.1 or in two separate steps (shown in equation 2.2 and 2.3). In the two-step mechanism, first the CO_2 binds to the metal surface with an electron to form COO*, and after this a proton reacts with the adsorbed molecule to form COOH*. This reaction pathway decouples the proton and electron transfer steps and may give flexibility in designing surfaces and electrochemical (i.e. pH and electrolyte composition/flow) conditions, which take advantage of this feature.

$$CO_2(g) + * + e^- \leftrightarrow COO^-* \qquad 2.2$$

$$COO^-* + H^+ \leftrightarrow COOH* \qquad 2.3$$

Regardless if the initial step occurs in one PCET or two uncoupled steps, a COOH* intermediate is formed and reacts with another proton and electron to form CO* and H_2O (equation 2.4). The final step is the desorption of CO from the catalyst surface (equation 2.5).[5]

$$COOH^* + H^+(aq) + e^- \leftrightarrow CO^* + H_2O(l) \quad 2.4$$

$$CO^* \leftrightarrow CO(g) + * \quad 2.5$$

Theoretical calculations using density functional theory (DTF) have shown that of the three elementary reaction steps, the formation of CO* from COOH* (eq. 4) requires the lowest overpotential on an Ag catalytic surface.[7] The other two steps have catalyst dependent limiting potentials, as shown extensively by Nørskov et al. through DTF calculations.[7,8] For Ag catalysts, this means that the first binding of CO_2 to the Ag surface (either equation 2.1 or equation 2.2) is the rate limiting step. As mentioned above, reaction conditions such as the (local) pH,[9] the electrolyte concentration[10] or grain boundaries on the catalyst[11,12,13] could be altered to improve the binding of this first intermediate. To be able to properly optimise the binding of this first reaction intermediate, it is vital to know exactly what the first intermediate is, i.e. if it is a PCET or a single electron transfer.

The first CO_2 to COOH* step has been computationally examined in detail, but still no conclusive evidence is given to conclude if it occurs in one or two steps. While many studies have focused on theoretical/simulational work to explore this initial step, experimental observation of the reaction intermediates to directly probe the reaction pathway are importantly lacking.

One potential method to observe reaction intermediates on a catalyst surface during electrocatalysis is via in situ electrochemical Attenuated Total Reflectance Fourier Transform Infrared spectroscopy (ATR-FTIR). Using this technique, it is possible to directly observe the intermediates that form on the surface of a catalyst during electrochemical CO_2 reduction. ATR-FTIR is a surface technique and therefore suitable to probe intermediates that are bound to a catalyst surface. While the vibrations of molecular bonds present near the ATR crystal can be detected, molecules that are also present in the electrochemical cell but farther away from the crystal are not detected due to the fast decaying evanescent infrared wave coming from the crystal surface. Figure 2.1 schematically depicts how the IR beam enters and leaves the ATR crystal.

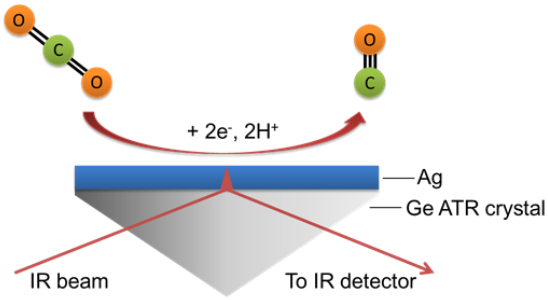

Figure 2.1. Schematic representation of the ATR crystal and how the path of the infrared beam is affected by the crystal. The red triangle starting at the surface of the crystal and passing through the Ag thin film represents the evanescent wave and how it decays when it is further away from the crystal surface.

In situ reflectance spectroscopy has been used to observe catalysts for several chemical reaction such as the oxidation of methanol[14], reduction of CO_2,[15] and oxidation of ethanol[16]. The electrochemical reduction of CO_2 was also studied on In and Sn electrodes by the group of Bocarsly to observe the mechanisms of the formation of formic acid on these electrodes.[17,18] Baruch et al.[18] show the presence of Sn-bound carbonate species using in situ ATR-FTIR measurements and claim that this carbonate is an intermediate in the reduction mechanism from CO_2 to formic acid. The carbonate forms when a CO_2 molecule binds to the native oxide present on the Sn electrode. These results imply that instead of the metallic Sn surface, rather the native oxide on the Sn is the catalytic surface during the formation of formic acid. The research by Baruch et al. shows that different reaction intermediates can form than what was expected by product detection studies.[19] ATR-FTIR can thus be a valuable tool in understanding the CO_2 electroreduction mechanism in more detail, and can help to guide rational pathways to create a more selective and efficient catalyst.

In this work, we use ATR-FTIR to directly observe the reaction intermediates of CO_2 electroreduction on Ag thin film electrodes. Experiments were performed in a KCl environment in order to eliminate the signal from the electrolyte that can adsorb to the catalyst surface and amplify the presence of surface bound species. Using this technique, specific reaction intermediates for the formation of CO and H_2 are shown as a function of applied potential, and a reaction scheme is developed that is consistent with these findings. Our results indicate that the first step in the CO_2 reduction mechanism on a sputtered Ag thin film and with a KCl electrolyte proceeds via a PCET under potentials that favour CO formation. At higher overpotentials (> -1.55 V), the indication of a de-coupled electron then proton transfer is also observed, showing that the applied potential can play a critical role in the reaction pathway for CO_2 electroreduction. For the first time, experimental evidence is shown that proves the existence of the COOH* intermediate on a Ag catalytic surface, and that the reaction mechanism is dependent

on the applied potential of the catalyst. Overall, we present a detailed reaction mechanism for the reduction of CO_2 to CO over Ag thin film electrodes.

2.4 Results and discussion

Characterisation of the silver thin film. To perform efficient and selective CO_2 electroreduction, a 50 nm Ag thin film was sputtered on the Ge ATR crystal. The Ag thin film was characterised using X-ray Diffraction (XRD), Atomic Force Microscopy (AFM) and X-ray Photoelectron Spectroscopy (XPS). The XRD data confirmed that a polycrystalline Ag film was sputtered on the Ge ATR crystal (Figure A1, this can be found in Appendix A). With an AFM it was found that Ag 10-20 nm crystallites uniformly covered the Ge crystal surface and that the roughness of the sputtered film was around 5.6 nm (Figure A2a). After a CO_2 reduction experiment, the surface morphology remains the same (Figure A2b-c and Table A1). The XPS data showed that the Ag thin film was metallic apart from a very thin layer of native oxide on the surface (Figure A3).

Operando electrochemical ATR-FTIR study of the Ag catalyst. The electrochemical ATR-FTIR experiments were performed in a home-made cell (Figure A4). The CO_2 reduction reaction occurs at the working electrode (WE) which is the Ag layer sputtered on top of the ATR crystal. A Pt counter electrode (CE), a Ag/AgCl reference electrode (RE) and a gas in- and outlet to purge either N2 and CO_2 are also present in the cell. The IR beam travels through the ATR crystal and at the location where it touches the crystal surface, an evanescent wave is formed that can probe the species present in this location (Figure 2.1). The electrolyte used was KCl due to its invisibility for infrared radiation, making it very suitable for these measurements in order to isolate the intermediate species formed during CO_2 reduction on the catalyst surface. It is important to note that any species present in the rest of the path of the IR beam will also be visible in the IR spectrum. To reduce the amount of signal coming from outside the CO_2 reduction area, the chamber below the ATR crystal was continuously purged with nitrogen.

Electrochemical response of Ag thin films. The ATR-FTIR measurements were performed at the following potentials: -1.40 V, -1.45 V, -1.50 V, -1.55 V and -1.60 V vs. Ag/AgCl because they are known from literature to produce a favourable CO yield (Figure A5).[5,20] The reference potential was not converted to the more commonly used reversible hydrogen electrode (RHE) because the pH of the measured system changes slightly due to the addition of CO_2 to the system.

During the infrared measurements, the cell was connected to a potentiostat that supplied a fixed potential to the working electrode. When the electrochemical cell was purged with nitrogen, the output current density was lower than when the cell was flushed with CO_2 as can be seen in Figure 2.2. These results indicate that when CO_2 is

introduced in the system, a higher product output is reached and thus both the CO_2 purged into the system and its aqueous derived forms like HCO_3^- and H_2CO_3 are indeed electrochemically active.

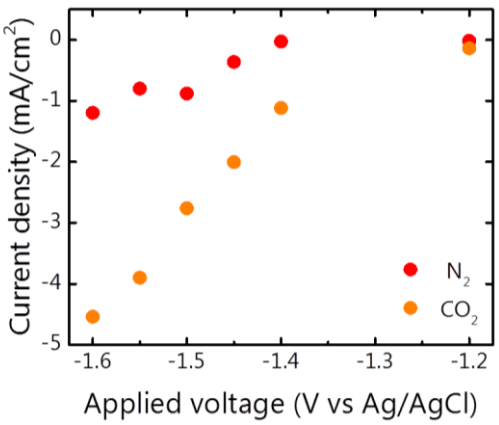

Figure 2.2. The average current density measured during the ATR-FTIR experiments at different potentials under both N_2 (red) and CO_2 (orange) flush.

Operando ATR-FTIR results at -1.45 V vs. Ag/AgCl. To properly assign all IR vibrations to the corresponding CO_2 reduction intermediates, ATR-FTIR spectra were recorded in systematically different conditions, first by flowing different gases (N_2 and CO_2), and by applying different potentials. Nitrogen was flowed through the cell for at least 30 minutes to remove any air from the cell compartment. A background IR spectrum was taken followed by a measurement 10 minutes later to ensure the system was at equilibrium. Then a new background spectrum was taken, a fixed potential was applied and a spectrum was recorded 1, 5, 10, 15, 20, 25 and 29 minutes after the potential was first applied. Then a new background spectrum was taken (with applied potential still on), CO_2 was purged to the cell and a spectrum was taken 1, 5, 10, 15, 20, 25 and 29 min after the CO_2 purge was first started. See Experimental section and Table A2 for further details. The signals that are relevant for this research are very small compared to the entire IR signal, therefore a new background had to be taken just before the CO_2 purge in the cell was started in order to better see the peaks relevant to CO_2 reduction. Only the spectra taken at 20 min after new conditions were installed are shown in this paper, unless stated otherwise.

The assignments of the infrared signals were based on values found in literature.[21,22,23,24,25,26,27,28,29,16,30] Since the current experiment (CO_2 reduction on a sputtered silver thin film) has never been measured in situ using an infrared technique before, literature values cannot be matched exactly to the data we observe in our study. Instead, literature values were taken from systems reported on silver that were observed not in situ and do not have an applied potential, or from experiments that were

conducted on different catalytic surfaces. Figure 2.3 gives an overview of where, based on literature, we expect to find the reactants, products, and intermediates that are present during the electrocatalytic reduction of CO_2 on silver.

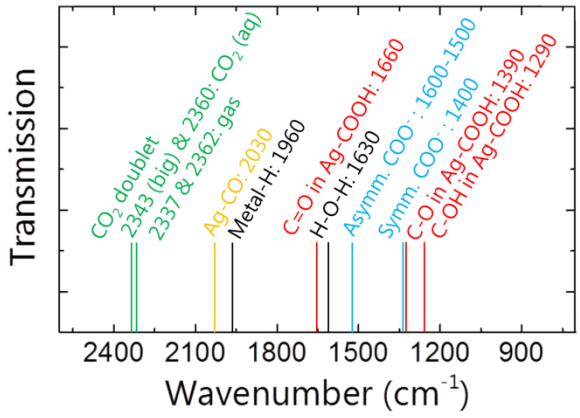

Figure 2.3. Predicted locations for the different reactants, products, and intermediates that are present during the ATR-FTIR experiments. The CO_2 doublet is shown in green, CO is shown in yellow, the COOH intermediates are shown in red, the COO^- intermediates signals are shown in blue, and black represents water and hydrogen.

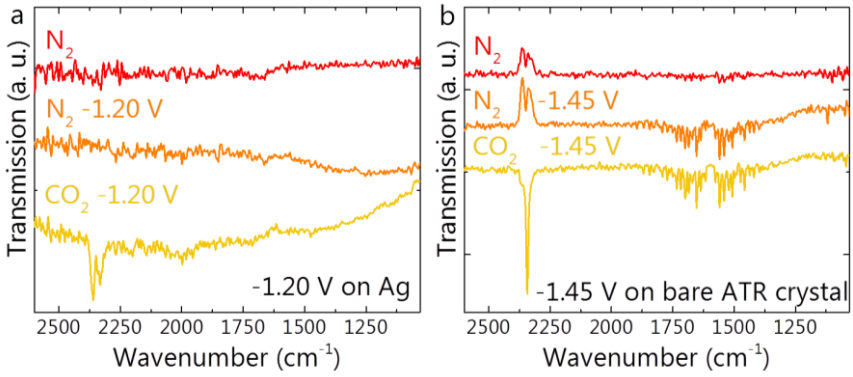

Figure 2.4. Control experiments (a) ATR spectra collected at -1.2V on a Ag catalyst. The background was not changed between the N_2 -1.20 V and the CO_2 -1.20 V spectra, to make sure no small IR signals could go undetected. (b) ATR spectra collected at -1.45 V without catalyst on the Ge ATR crystal.

To make sure that the peaks assigned to COOH do not belong to CO_2 molecules physisorbed on the Ag surface, several control experiments were performed. The physisorption of CO_2 molecules is also possible at an applied negative potential that is not negative enough to start the CO_2 reduction reaction. Therefore, ATR-FTIR data was collected while the cell was operating at -1.20 V vs Ag/AgCl (Figure 2.4a), which is not

a negative enough potential to evolve CO. These spectra show no sign of peaks in the region between 1800 and 1000 cm^{-1}, where the COOH vibrations are assigned.

To eliminate the possibility of seeing any signal from molecules attached to the germanium surface, a control experiment was carried out on a bare Ge ATR crystal (Figure 2.4b). The ATR-FTIR spectra do not show any peaks in the 1800-1000 cm^{-1} region.

A typical set of ATR-FTIR data during electrochemical measurements is given in Figure 2.5. This figure shows an FTIR spectrum with only N2 flowing in the system (red/top), with N_2 flowing and an applied potential of -1.45V vs Ag/AgCl (orange/middle), and with CO_2 flowing and an applied potential of -1.45V vs Ag/AgCl (yellow/bottom). All spectra were recorded when the gas flush was on for 20 minutes. The large peak at 1965 cm^{-1} is assigned to the Ag-H vibrational mode.[25,24] When the CO_2 begins flowing, the Ag-H feature became slightly positive, meaning that part of the Ag-H species disappeared from the Ag surface and a new feature at 2034 cm^{-1} appeared. The 2034 cm^{-1} feature is assigned to the Ag-CO vibrational mode.[22,23] The Ag-CO peak is small compared to the Ag-H since CO readily desorbs from an Ag surface.[22]

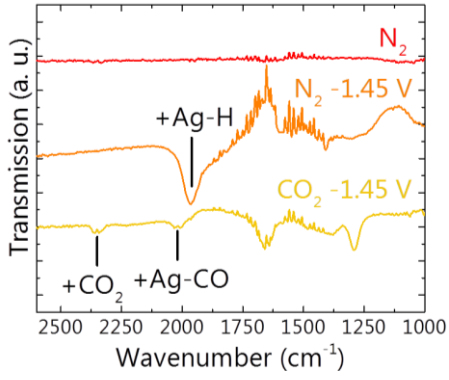

Figure 2.5. Assignments of reactants and products present during ATR-FTIR experiments in 0.1 M KCl. A full experimental procedure is shown: the red line is a spectrum taken during N_2 flow where the background was also taken during N_2 to make sure the system is in equilibrium. The orange spectrum is taken 20 min after a potential of -1.45 V is applied with the red line as background spectrum. The red spectrum is taken 20 min after CO_2 is introduced to the cell with 30 min N_2 at -1.45 V as background spectrum.

ATR-FTIR spectra as a function of applied potential. To determine if the reaction intermediates were formed uniformly under different conditions, ATR-FTIR spectra were recorded at different applied potentials, as shown in Figure 2.6. From Figure 2.6 it is clear that the peak location of the C-OH stretch is not fixed at a specific wavenumber. This is a strong indication that this signal belongs to a surface bound species, since a difference in potential will lead to a difference in surface coverage which changes the exact location of the molecular vibration.[30] Table 2.1 specifies the peak positions in

Figure 2.6 per applied potential and as an average value. The average values are used in the rest of the text when general assignments are mentioned, for assignments at specific potentials the average value is not used.

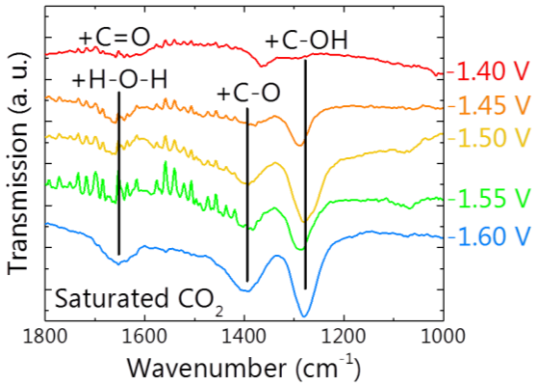

Figure 2.6. ATR transmission spectra in saturated CO_2 0.1 M KCl electrolyte at different potentials showing the peaks that belong to the CO_2 reduction intermediates. The background for these spectra was taken after 30 min at the same potential under a nitrogen purge.

Table 2.1. Peak positions (cm^{-1}) as a function of applied potential after 20 min of CO_2 flow and their assignments.

-1.40 V	-1.45 V	-1.50 V	-1.55 V	-1.60 V	Average[a]	Assignment[b]
1297	1291	1284	1288	1280	1288	ν COOH: OH-deformation
1366	1383	1394	1387	1399	1386	ν COOH: C-O stretch
				1410		ν_s COO-: symm. stretch
1635	1643	1645			1641	H-O-H bend
1660	1660	1664	1660	1654	1660	ν COOH: C=O stretch
	2005					Ag-CO
	2034	2034		2032	2033	Ag-CO
	2038		2038		2038	Ag-CO
		2341		2339		CO_2 (g)
2345	2345					CO_2 (aq)
	2360					CO_2 (aq)
	2366	2364	2362	2364		CO_2 (g)

[a] The average peak positions are used in the text. [b] References for the assignments can be found in the text.

The ATR-FTIR spectra in Figure 2.6 feature a large peak at 1288 cm^{-1} belonging to the C-OH stretch of COOH.[27,28] The inverse water peak (H-O-H bend)[31,32] that was present

in the N_2 at -1.45V spectrum at 1652 cm^{-1} seemed to broaden with the presence of flowing CO_2 at -1.45V, to show a combination of the H-O-H bend and a C=O asymmetric stretch at 1660 cm^{-1} that is assigned to the COOH* intermediate.[29,28,27] The peaks at 1288 cm^{-1} and 1660 cm^{-1} combined indicate that the COOH* intermediate is present during the CO_2 reduction on the Ag film.

Another peak at 1386 cm^{-1} is more difficult to assign. Literature suggests that this is a symmetric stretch of COO^-.[26,27,29] However, according to these studies, when only the symmetric stretch is visible and not accompanied by the asymmetric stretch, COO^- is most likely adsorbed to the Ag through both its oxygen atoms (Figure 2.7a). The asymmetric COO^- is invisible in the ATR configuration because the electric field of the silver film cancels out the dipole of COO^-*. Nonetheless, COO^-* bound through the oxygen atoms seems to be a very unlikely intermediate for the current experiment since this orientation of the first intermediate towards the catalytic surface determines whether the product will be formic acid (Figure 2.7a) or carbon monoxide (Figure 2.7b).[6] When oriented as in Figure 2.7a, the COO^-* intermediate will not be able to form COOH*, which we clearly do observe, and can only form formic acid. According to Figure 2.6, we see that the ratio between the 1288 and the 1386 cm^{-1} signals is fixed, which seems to indicate that these signals belong to the same intermediate species. Therefore, by considering the multiple peaks associated with the COOH intermediate, we rule out the possibility of the oxygen bonded to the Ag catalyst surface orientation (Figure 2.7a) as a possible intermediate, and we can say that the carbon atom is bonded directly to the Ag surface, as shown in Figure 2.7b.

The combination of the 1281 cm^{-1}, 1370 cm^{-1} and 1713 cm^{-1} peaks was assigned to the OH-deformation, C-O stretching and C=O stretch of a COOH intermediate bound to Pt by Xia et al. in their observation of ethanol oxidation over Pt catalysts.[16] The catalyst in our study is different than that studied by Xia et al., therefore the peak values are slightly shifted compared to the current work on a Ag catalyst. We therefore assign the 1288 cm^{-1}, 1386 cm^{-1} and 1660 cm^{-1} peaks to the COOH intermediate.

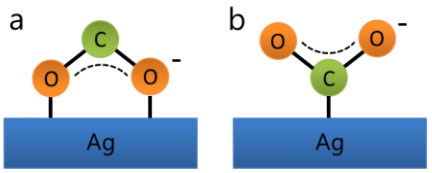

Figure 2.7. The two possible configurations of a COO^- intermediate bound to an Ag catalyst are depicted: bound to the surface through (a) the oxygen atoms or (b) the carbon atom.

At an applied potential of -1.60 V vs. Ag/AgCl, the 1399 cm^{-1} peak broadens compared to smaller applied potentials. This seems to indicate that the peak here is a combination

of two peaks, the 1386 cm^{-1} peak that belongs to the COOH intermediate, but also a peak at a higher wavenumber, that indicates a COO^- intermediate.

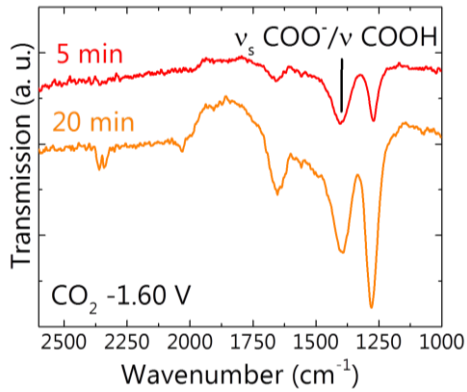

Figure 2.8. ATR transmission spectra in saturated CO_2 0.1 M KCl electrolyte at different potentials showing the overlapping peaks that belong to the CO_2 reduction intermediates. The background for these spectra was taken after 30 min at the same potential under a nitrogen purge.

In multiple proton and electron transfer reactions, an optimum must be found between the concentration of protons (pH), the electron affinity (affected by the applied potential) and the proton affinity or concentration of reactants (pK_a).[33] When we consider the evolution of the ATR spectra recorded at various potentials during CO_2 flushing over time, we can see the influence of the CO_2 concentration in solution on the reaction mechanism. The ATR-FTIR spectra recorded after 5 minutes of CO_2 flushing (Figure A6) are very similar to the spectra in Figure 2.6 (taken after 20 min). The only clearly different spectrum is the spectrum recorded at an applied potential of -1.60 V, where the 1404 cm^{-1} peak is larger than the 1273 cm^{-1} peak (Figure 2.8). This implies that the 1404 cm^{-1} peak consists of both the C-O stretch of COOH* and the COO^-* symmetric stretch.

Implications for the CO_2 reduction reaction mechanism. At an applied potential of -1.60 V, both the electron affinity and the pH are fixed. The concentration of the reactant CO_2 is however not fixed when we compare the spectra given in Figure 2.8. These conditions change the pK_a for the reaction in equation 2.2, and the reaction proceeds slower when less CO_2 is present (red spectrum) because the mass transfer of CO_2 to the Ag surface is too slow when the CO_2 concentration in the electrolyte is low. Therefore the COO^-* intermediate has a longer residence time at the Ag surface and gives a relatively larger IR signal compared to when the solution is saturated with CO_2 (orange spectrum in Figure 2.8).

For all other potentials, no sign of the COO^-* intermediate is found. These results indicate that the PCET mechanism is the dominant reaction mechanism in the potential

range -1.40 to -1.55 V and the 2-step mechanism including the COO^{-}* intermediate is present at a more negative potential. When -1.60 V is applied to the catalyst, the silver becomes so negatively charged that CO_2 binds to the catalyst immediately, and no proton coupling is required for the first reaction step. The Ag-COO^{-} intermediate can be stabilised by K^{+} ions that are drawn to the very negatively charged Ag surface. When the applied potential is not very negative the first reaction step is the PCET. In this case the potential barrier for CO_2 to bind to the catalytic surface is relatively high and slow enough for protons to always be close enough to the catalytic surface to join the reaction and form COOH* rather than COO^{-}*.

The results found in the present work confirm the presence of the COOH* intermediate at all applied potentials. The COOH molecule is not a carbonate form as detected by Baruch et al. on Sn.[18] According to the XPS data, a native oxide layer on Ag is present, but during the first minutes when a negative potential is applied, this oxide is reduced (Figure A7).[34] Therefore, no carbonate species can form on the Ag surface during the CO_2 reduction reaction.

At most of the applied potentials (-1.40 V to -1.55 V vs. Ag/AgCl) Ag-COOH and Ag-CO are the only detected intermediates for the CO_2 reduction reaction. For these potentials it can be concluded that that the PCET mechanism (Figure 2.9) is the dominant reaction pathway.

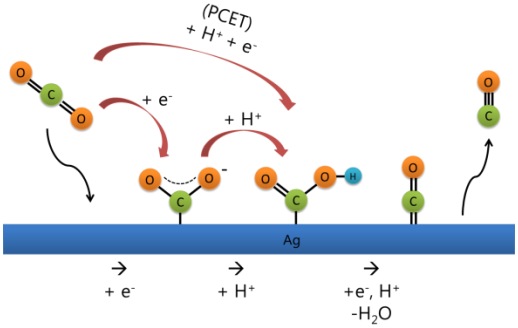

Figure 2.9. Schematic depiction of proposed reaction mechanism of CO_2 reduction to CO on a thin film Ag catalyst. At most applied potentials, the 1 step PCET mechanism leads to the formation of CO on the Ag thin film catalyst. At -1.6 V the 2-step reaction mechanism is dominant.

When the applied potential becomes more negative (-1.60 V vs. Ag/AgCl), the peak at 1399 cm^{-1} broadens. In this case both COO^{-}* and COOH* are reaction intermediates and the 2-step reaction mechanism is also present. The only other intermediates that were detected are Ag-CO and Ag-H. The rest of the mechanisms as proposed in literature can therefore be confirmed for the currently studied system. We can learn from these results

that both COO^{-}* and COOH* are important intermediates and that the pH, the applied potential and their binding energy to the catalyst surface are very important parameters in the design and optimisation of future CO_2 reduction catalysts.

2.5 Conclusions

The exact mechanism for CO_2 reduction on Ag catalysts has for a long time remained unclear. Two possible mechanisms (the PCET mechanism and the sequential electron then proton transfer mechanism) are often proposed in literature. In our study we have conducted operando ATR-FTIR experiments to give insight into the mechanism on a Ag thin film catalyst using KCl as the electrolyte.

The operando ATR-FTIR measurements in an electrochemical cell with the Ag working electrode deposited directly onto the ATR crystal, allowed us to determine the surface bound intermediates of the electrocatalytic CO_2 reduction reaction on a Ag thin film catalyst. Since the Ag catalyst was deposited directly on the ATR crystal, the IR signals of the reaction intermediates were large enough to discern. In this system, it was possible to detect both Ag-H and Ag-CO intermediates that lead directly to the formation of H_2 and CO, respectively. In the potential range between -1.40 V to -1.55 V vs. Ag/AgCl. COOH* was observed as the only reaction intermediate. At an applied potential of -1.6 V vs. Ag/AgCl, COO^{-}* was also observed.

From these results we can say that the CO_2 reduction mechanism on a sputtered Ag film in KCl electrolyte is a PCET mechanism when the applied potential is between -1.40 V to -1.55 V vs. Ag/AgCl. At more negative applied potential (-1.60 V) the reaction follows the 2-step mechanism were COO^{-}* is formed before COOH*. The more negative potential overcomes the potential barrier that CO_2 has for binding to the Ag surface, therefore the CO_2 will bind to Ag, independent of the presence of a proton. This means that the COO^{-}* intermediate is more easily formed in these conditions.

These results show that operando ATR-FTIR can be a very valuable tool in understanding the interplay between the catalyst and the applied potential during the electrochemical CO_2 reduction reaction. To further improve the CO_2 reduction process, spectroscopic techniques should be used to elucidate the different effects of varying reaction parameters on the CO_2 reduction reaction mechanism such as pH, electrolyte concentration and composition.

2.6 Experimental section

Catalyst preparation on ATR crystal. Silver thin films (50 nm) were sputtered at 20 W using an ultra-high vacuum magnetron sputtering PREVAC system onto a rotating Ge ATR crystal. The sides of the ATR crystal were covered during sputtering so only the top would be covered with Ag. After each electrochemical test, a redeposition of the Ag

thin film was performed. The crystal was first cleaned by a presputter procedure: the crystal surface was bombarded with argon ions to remove the top layer, i.e. the previously used Ag film, and then a subsequent fresh film was deposited.

Structural characterisation of catalyst. XRD patterns (10° – 90° 2θ) were collected using a Bruker D8 Advance X-ray diffractometer in Bragg-Brentano configuration with a cobalt source (λ=1.7889 Å). The surface topology of the catalyst was determined by AFM recorded in semi-contact mode with a NT-MDT Ntegra apparatus equipped with a NTMDTP8 XPM controller and a NT-MDT NSG30 cantilever. XPS experiments were conducted using a Thermo Scientific K-alpha apparatus equipped with an Al K-alpha X-ray Source and a Flood Gun to avoid charging of the sample. Parameters used for the measurements were: spot size of 400 μm, pass energy of 50 eV, energy step size of 0.1 eV, dwell time of 50 ms, 20 scans in the vicinity of Ag 3d, Ge 3d, O 1s and C 1s orbitals binding energy. XPS spectra were corrected using the atmospheric carbon C peak position (284.8 eV).

Operando ATR-FTIR electrochemical measurements. ATR-FTIR experiments were performed on a Bruker Vertex 70 equipped with a liquid nitrogen cooled LN-MCT detector and a Veemax III ATR accessory (Kromatek) and a home-made spectro-electrochemical cell (Figure A4). A Teflon cell was mounted onto a single bounce 45^0 Ge ATR crystal and used in a three-electrode configuration with a sputtered Ag thin film as the working electrode (working electrode area is 1.79 cm^2), a coiled Pt wire as counter electrode and a Ag/AgCl reference electrode (saturated KCl, XR300, Radiometer Analytical). A potentiostat MODEL283 (Princeton Applied Research) was used to apply a potential to the cell. A gas in- and outlet were connected at the top of the cell, both N_2 and CO_2 could be bubbled at 3 ml/min through the 0.1 M KCl (Acros Organics, >99% purity) in deionised water electrolyte.

We measured the uncompensated resistance (R_u) for our spectro-electrochemical cell using a PARSTAT 4000 potentiostat and the standard iR determination procedure of the VersaStudio software. While purging the cell with nitrogen, R_u was determined to be 5.4 Ω. For the highest current measured during a nitrogen purge, the iR_u at -1.6 V vs. Ag/AgCl was 2.1 mA * 5.4 Ω = 11.6 mV. When the R_u was determined during the CO_2 purge, it was found to be negligible.

Prior to and during the electrochemical measurements, the ATR accessory was purged with nitrogen. The electrolyte volume (5 ml) was purged with nitrogen for at least 30 min to remove oxygen from the water (the electrolyte was saturated with N_2 or CO_2 after 20 min) prior to the ATR-FTIR measurements. A background spectrum was then taken and a spectrum was recorded using this background 10 min later to make sure the system was in equilibrium. A new background was recorded 1 min before the desired potential was set. To diminish the possibility of delamination of the Ag thin film, the

desired potential was not reached at once, but slowly increased over a period of 3 min. once the desired potential was reached, an ATR-FTIR spectrum was recorded at 1, 5, 10, 15, 20, 25 and 29 min to monitor the trend in peak growth. After 30 min, a new background spectrum was taken and after this, the gas was switched from N_2 to CO_2 while the flow rate was maintained at 6.5 ml/min. The potential was not switched off when the gasses were switched. One minute after the CO_2 was turned on, a first ATR-FTIR spectrum was recorded, followed by a spectrum at 5, 10, 15, 20, 25 and 29 min. An overview of the different background scans that are used during a single set of experiments is given in Table A2. All stated potentials are referenced to the Ag/AgCl reference electrode. The ATR-FTIR spectra were collected with OPUS software, 64 scans were collected for each spectrum at a resolution of 4 cm^{-1} in the range 600-5000 cm^{-1} without any amplification of the IR signal or atmospheric compensation. The baselines were corrected with either a linear or quadratic fit by custom-written software. The spectra are presented as transmittance spectra, meaning that negative and positive peaks represent an increase and decrease in signal, respectively. For clarity, some of the spectra are also presented in absorbance and ATR in Figure A8. Over time, the quality of the ATR crystal degrades slightly due to the presputter treatment. Therefore the aperture of the IR beam was adjusted before each set of experiments to allow a maximum IR signal to reach the detector. The pH of the electrolyte in the cell was measured with a WRW pH/Cond 340i meter connected to a SenTix 41 Electrode, and found to be 5.9 ± 0.1 after the experiment was finished, which is consistent with the previous work of Hori.[35]

2.7 References

(1) Martín, A. J.; Larrazábal, G. O.; Pérez-Ramírez, J. Green Chem. 2015, 17, 5114–5130.

(2) Dahl, S.; Chorkendorff, I. Nat. Mater. 2012, 11, 100–101.

(3) Hori, Y. In Modern Aspects of Electrochemistry No. 42; Vayenas, C. G., Gamboa-Aldeco, M. E., White, R. E., Eds.; Springer: New York, 2008; pp 89–189.

(4) Kuhl, K. P.; Cave, E. R.; Abram, D. N.; Jaramillo, T. F. Energy Environ. Sci. 2012, 5, 7050–7059.

(5) Hatsukade, T.; Kuhl, K. P.; Cave, E. R.; Abram, D. N.; Jaramillo, T. F. Phys. Chem. Chem. Phys. 2014, 16, 13814–13819.

(6) Kortlever, R.; Shen, J.; Schouten, K. J. P.; Calle-Vallejo, F.; Koper, M. T. M. J. Phys. Chem. Lett. 2015, 6, 4073–4082.

(7) Peterson, A. A.; Nørskov, J. K. J. Phys. Chem. Lett. 2012, 3, 251–258.

(8) Shi, C.; Hansen, H. A.; Lausche, A. C.; Nørskov, J. K. Phys. Chem. Chem. Phys. 2014, 16, 4720–4727.

(9) Ma, M.; Djanashvili, K.; Smith, W. A. Angew. Chemie - Int. Ed. 2016, 55, 6680–6684.

(10) Kas, R.; Kortlever, R.; Yilmaz, H.; Koper, M. T. M.; Mul, G. ChemElectroChem 2015, 2, 354–358.

(11) Rosen, J.; Hutchings, G. S.; Lu, Q.; Rivera, S.; Zhou, Y.; Vlachos, D. G.; Jiao, F. ACS Catal. 2015, 5, 4293–4299.

(12) Chen, Y.; Li, C. W.; Kanan, M. W. J. Am. Chem. Soc. 2012, 134, 19969–19972.

(13) Lee, H. E.; Yang, K. D.; Yoon, S. M.; Ahn, H. Y.; Lee, Y. Y.; Chang, H.; Jeong, D. H.; Lee, Y. S.; Kim, M. Y.; Nam, K. T. ACS Nano 2015, 9, 8384–8393.

(14) Beden, B.; Lamy, C.; Bewick, A.; Kunimatsu, K. J. Electroanal. Chem. 1981, 121, 343–347.

(15) Oda, I.; Ogasawara, H.; Ito, M. Langmuir 1996, 12, 1094–1097.

(16) Xia, X. H.; Liess, H.-D.; Iwasita, T. J. Electroanal. Chem. 1997, 437, 233–240.

(17) Detweiler, Z. M.; White, J. L.; Bernasek, S. L.; Bocarsly, A. B. Langmuir 2014, 30, 7593–7600.

(18) Baruch, M. F.; Pander III, J. E.; White, J. L.; Bocarsly, A. B. ACS Catal. 2015, 5, 3184–3156.

(19) Chen, Y.; Kanan, M. W. J. Am. Chem. Soc. 2012, 134, 1986–1989.

(20) Hoshi, N.; Kato, M.; Hori, Y. J. Electroanal. Chem. 1997, 440, 283–286.

(21) Kumar, R.; Lang, S.; Englezos, P.; Ripmeester, J. J. Phys. Chem. A 2009, 113, 6308–6313.

(22) Gravejat, P.; Derrouiche, S.; Farrussengn, D.; Lombaert, K.; Mirodatos, C.; Bianchi, D. J. Phys. Chem. C 2007, 111, 9496–9503.

(23) Marinkovic, N. S.; Wang, J. X.; Marinkovic, J. S.; Adzic, R. R. J. Phys. Chem. B 1999, 103, 139–144.

(24) Collins, S. E.; Baltanas, M. A.; Bonivardi, A. L. J. Catal. 2004, 226, 410–421.

(25) Collins, S. E.; Baltanas, M. A.; Garciafierro, J. L.; Bonivardi, A. L. J. Catal. 2002, 211, 252–264.

(26) Smith, E. L.; Porter, M. D. J. Phys. Chem. 1993, 97, 8032–8038.

(27) Lee, S. J.; Han, S. W.; Yoon, M.; Kim, K. Vib. Spectrosc. 2000, 24, 265–275.

(28) Garand, E.; Wende, T.; Goebbert, D. J.; Bergmann, R.; Meijer, G.; Neumark, D. M.; Asmis, K. R. J. Am. Chem. Soc. 2010, 132, 849–856.

(29) Han, S. W.; Ha, T. H.; Kim, C. H.; Kim, K. Langmuir 1998, 14, 6113–6120.

(30) Vigier, F.; Coutanceau, C.; Hahn, F.; Belgsir, E. M.; Lamy, C. J. Electroanal. Chem. 2004, 563, 81–89.

(31) Loring, J. S.; Thompson, C. J.; Wang, Z.; Joly, A. G.; Sklarew, D. S.; Schaef, H. T.; Ilton, E. S.; Rosso, K. M.; Felmy, A. R. Environ. Sci. Technol. 2011, 45, 6204–6210.

(32) Mizaikoff, B. Chem. Soc. Rev. 2013, 42, 8683–8699.

(33) Koper, M. T. M. Chem. Sci. 2013, 4, 2710–2723.

(34) Wei, W.; Mao, X.; Ortiz, L. A.; Sadoway, D. R. J. Mater. Chem. 2011, 21, 432–438.

(35) Hori, Y.; Murata, A.; Takahashi, R. J. Chem. Soc. Faraday Trans. 1 1989, 85, 2309–2326.

Appendix A

Structural characterisation of the Ag catalyst surface deposited on the ATR crystal

Silver thin films were sputtered directly onto the (111) Ge ATR crystal. The XRD results in Figure A1 show that the preferred orientation of silver is also (111) when grown on the Ge crystal surface. A very small (200) Ag reflection was also visible on the as-deposited Ag layer. Since XRD is a bulk technique, this does not necessarily mean that the (111) or (200) planes are the surface exposed facets. We can conclude from the XRD data that the Ge crystal is covered with Ag and that the studied Ag surface is polycrystalline.

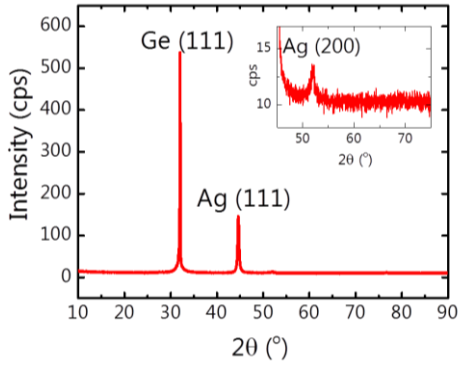

Figure A1. XRD pattern of a 50 nm Ag film sputtered on a Ge (111) ATR single crystal. The inset shows the small reflection at 51.9^0 2θ.

The AFM data of the sputtered Ag showed a very smooth surface (Figure A2a). The Ag grains are around 10 to 20 nm in size and form a continuous layer on the germanium surface. The Ge crystal was very smooth and the root mean square surface roughness (R_{RMS}) was 5.6 nm (Figure A2a and Table A1). After a CO_2 reduction experiment, the roughness of the Ge crystal increased slightly but still showed the same uniform coverage of sputtered Ag particles. An increased applied potential does not influence the surface morphology as can be seen when Figure A2b and c are compared.

Table A1. Average root mean square roughness per sample calculated over 5 different points after CO_2 reduction and 3 different points before CO_2 reduction.

	Average R_{RMS}	St. deviation R_{RMS}
After Ag deposition	5.6 nm	0.3 nm
Post -1.45V vs RHE	10.3 nm	5.0 nm
Post -1.60V vs RHE	8.6 nm	2.8 nm

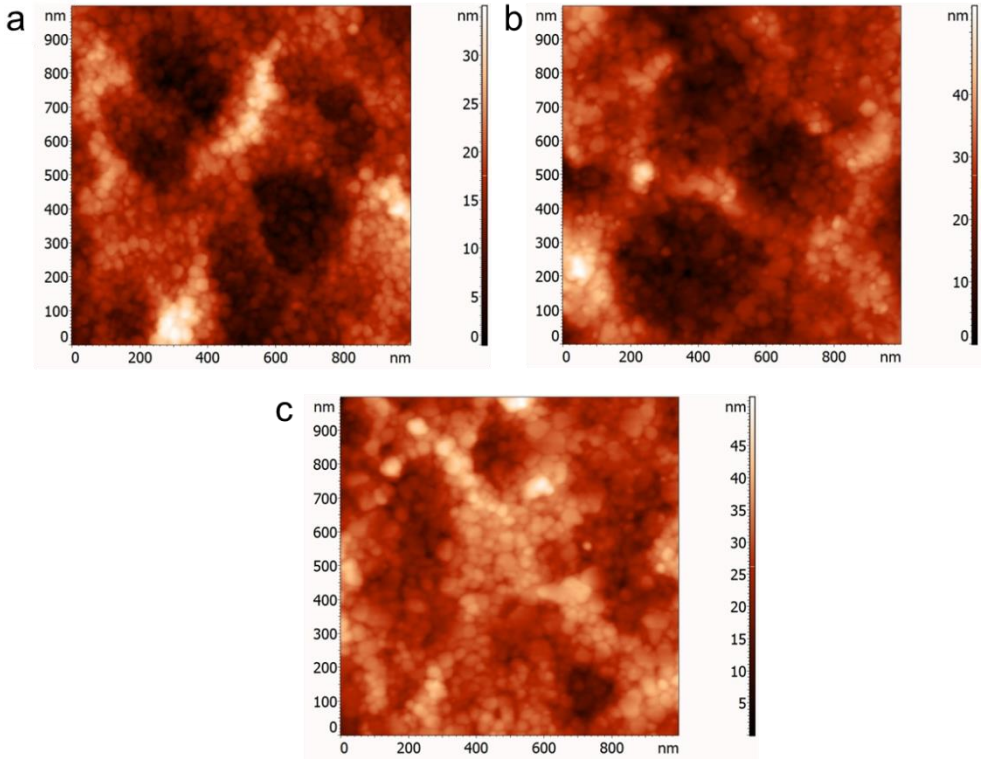

Figure A2. AFM images of sputtered Ag film on Ge ATR crystal (a) before CO_2 reduction and after CO_2 reduction at (b) -1.45 V vs. Ag/AgCl and (c) -1.60 V vs. Ag/AgCl.

To confirm the presence and composition of Ag on the Ge crystal, XPS measurements were performed on a Ge crystal with a 50 nm Ag thin film (Figure A3a and b). The Ag doublet was fitted as one peak that was not bonded to oxygen, i.e. metallic Ag. The oxygen 1s signal was deconvoluted to 2 peaks, one peak (531.0 eV) bonds to silver as a native oxide,[1] the other peak (532.1 eV) is an organic carbon bond. The oxygen-silver fit is relatively small, therefore it seems likely that this bond was not found in the Ag3d peak.

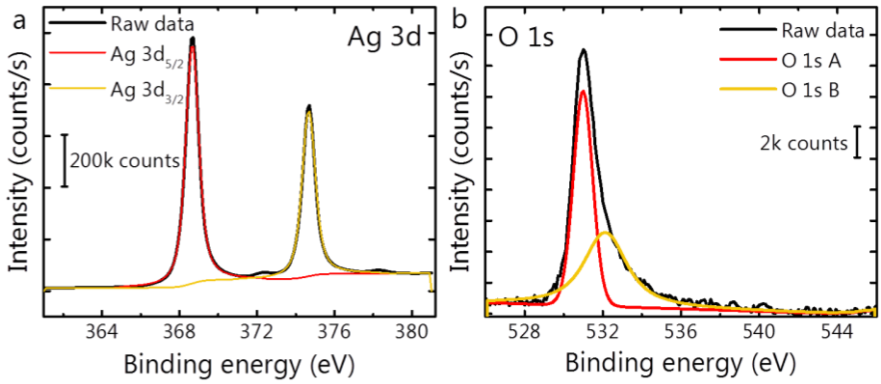

Figure A3. XPS spectra of the (a) Ag 3d and (b) the O 1s peak of a sputtered Ag thin film (50 nm) on a Ge ATR crystal. The raw data (black line) was fitted with two peaks (red and yellow lines). In the case of Ag 3d, the $3d_{5/2}$ (368.7 eV in red) and $3d_{2/3}$ (374.7 eV in yellow) were identified as single peaks. The O 1s peak was deconvoluted into a peak at 531.0 eV (A, red) bound to Ag as a native oxide and a peak at 532.1 eV (B, yellow) bound to organic carbon.

Spectro-electrochemical cell lay-out and IR background procedures

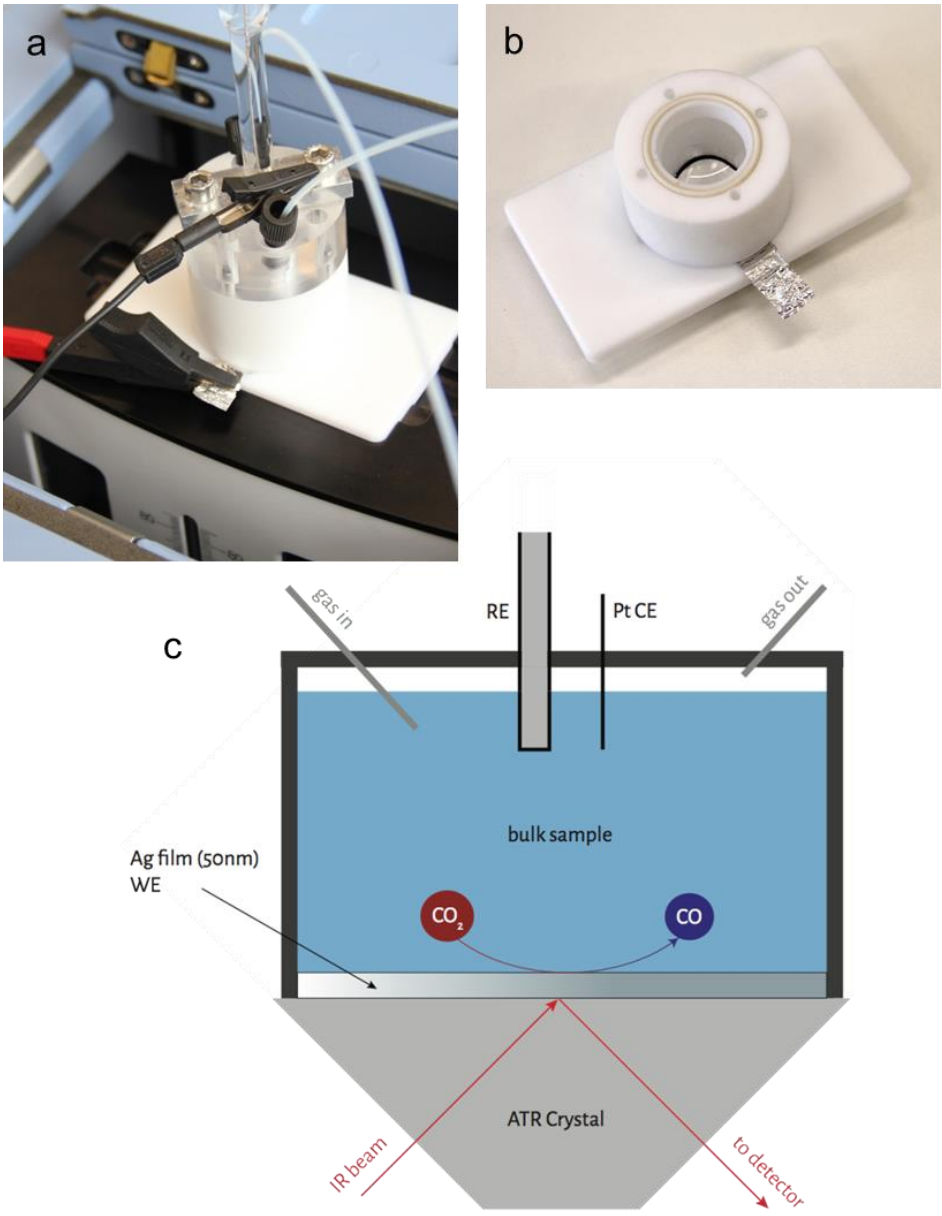

Figure A4. Pictures of the electrochemical cell used for ATR-FTIR measurements. (a) Cell in use, (b) Open cell: bottom of the cell is the Ag working electrode, (c) Schematic of the cell.

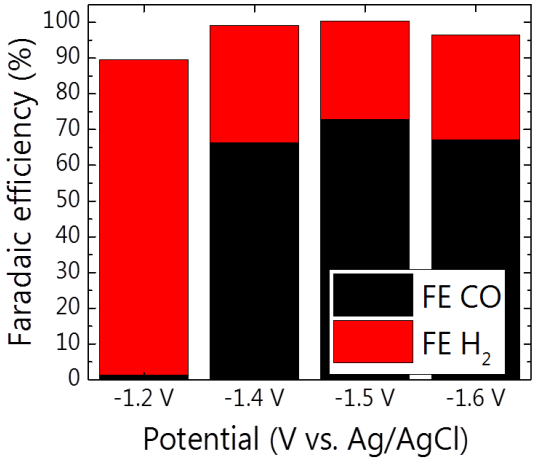

Figure A5. Faradaic efficiency for Ag foil in 0.1 M KCl saturated with CO_2. Experimental details can be found in papers published previously by our group.[2,3]

Table A2. An overview of the backgrounds that belong to the different ATR-FTIR measurements.

System	Background	Comment
N_2 flush	N_2 flush	New backgrounds are taken until the spectrum becomes a flat line, and the system has reached equilibrium
N_2 flush and potentiostat on	N_2 flush	
CO_2 flush and potentiostat on	N_2 flush and potentiostat on for 30 min	The formation of hydrogen still occurs in this system but is no longer visible in the spectra because of the background used

ATR-FTIR results

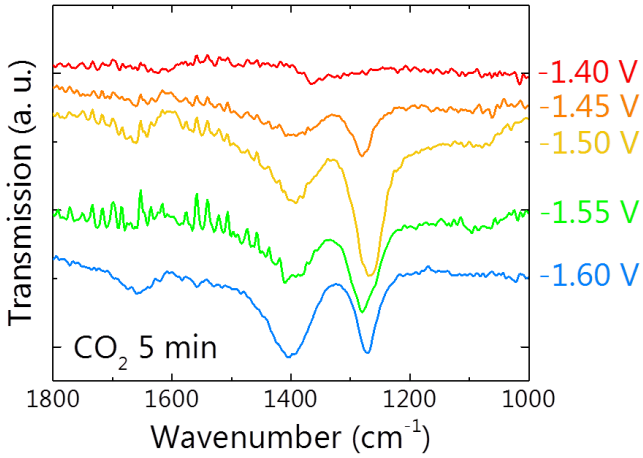

Figure A6. ATR transmission spectra in CO_2 0.1 M KCl electrolyte at different potentials 5 min after the CO_2 purge was turned on.

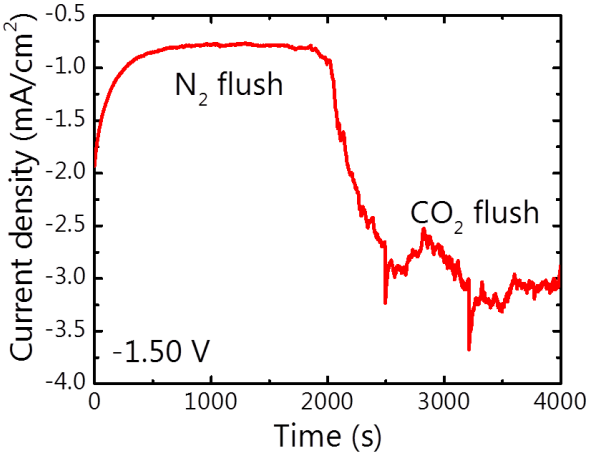

Figure A7. Current density versus time at an applied potential of -1.50 V vs. Ag/AgCl. During the first few minutes the native oxide is reduced, as can be seen from the quickly decreasing current density in the first minutes.

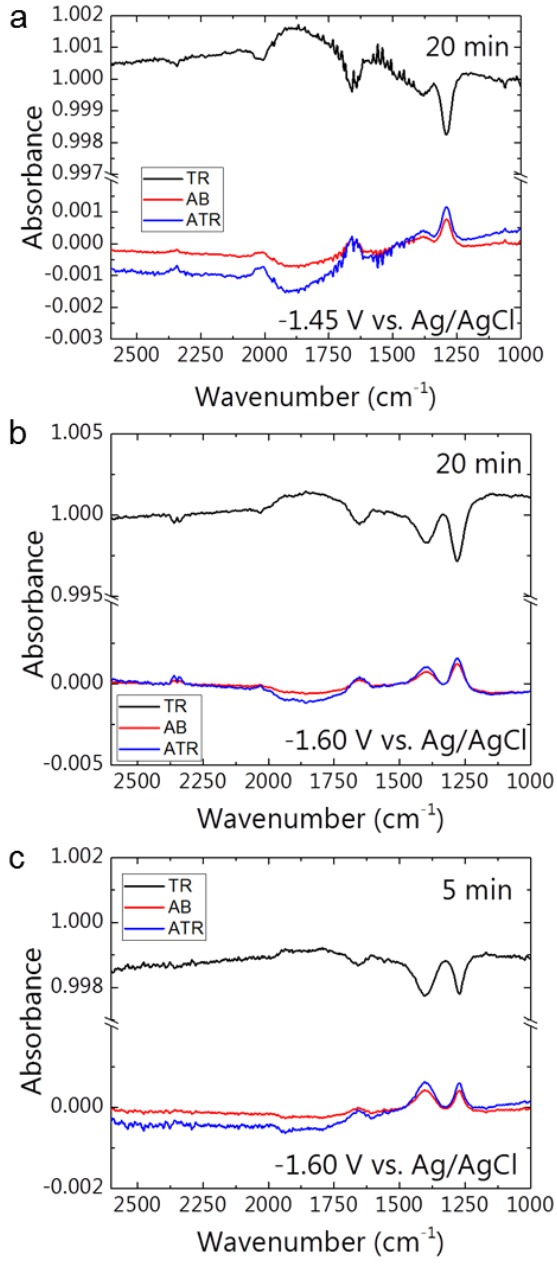

Figure A8. ATR-FTIR spectra shown in transmission (TR), absorbance (AB) and attenuated total reflectance (ATR). (a) spectra measured at -1.45 V at saturated CO_2, (b) spectra measured at -1.60 V at saturated CO_2 and (c) spectra measured at -1.60 V at low CO_2 concentration.

References

(1) Hatsukade, T.; Kuhl, K. P.; Cave, E. R.; Abram, D. N.; Jaramillo, T. F. Phys. Chem. Chem. Phys. 2014, 16, 13814.

(2) Ma, M.; Djanashvili, K.; Smith, W. A. Phys. Chem. Chem. Phys. 2015, 17, 89.

(3) Ma, M.; Djanashvili, K.; Smith, W. A. Angew. Chemie - Int. Ed. 2016, 55, 6680.

3

Operando EXAFS study reveals presence of oxygen in oxide-derived silver catalysts for electrochemical CO_2 reduction

This chapter is based on the following publication:

N.J. Firet, M.A. Blommaert, T. Burdyny, A. Venugopal, D. Bohra, A. Longo, W.A. Smith. Operando EXAFS study reveals presence of oxygen in oxide-derived silver catalysts for electrochemical CO_2 reduction. J. Mater. Chem. A. 2019, 7, 2597-2607

Electrocatalysis of carbon dioxide can provide a valuable pathway towards the sustainable production of chemicals and fuels from renewable electricity sources. One of the main challenges to enable this technology is to find suitable electrodes that can act as efficient, stable and selective CO_2 reduction catalysts. Modified silver catalysts and in particular, catalysts electrochemically derived from silver-oxides, have shown great promise in this regard. Here, we use operando EXAFS analysis to study the differences in surface composition between a pure silver film and oxide-derived silver catalysts - a nanostructured catalyst with improved CO_2 reduction performance. The EXAFS analysis reveals the presence of trace amounts of oxygen in the oxide-derived silver samples, with the measured oxygen content correlating well with experimental studies showing an increase in CO_2 reduction reactivity towards carbon monoxide. The selectivity towards CO production also partially scales with the increased surface area, showing that the morphology, local composition and electronic structure all play important roles in the improved activity and selectivity of oxide-derived silver electrocatalysts. Earlier studies based on X-ray photoelectron spectroscopy (XPS) were not able to identify this oxygen, most likely because in ultra-high vacuum conditions, silver can self-reduce to Ag^0, removing existing oxygen species. This operando EXAFS study shows the potential for in situ and operando techniques to probe catalyst surfaces during electrolysis and aid in the overall understanding of electrochemical systems.

3.1 Introduction

In recent years, several research efforts have been made to expedite the implementation of renewable energy into society. While renewable electricity can be generated at large scales through solar and wind energy with continually decreasing costs, challenges remain in effectively utilizing the intermittent electricity that is generated. Storing energy in the form of chemicals is one means of using this electricity that may both increase its value and provide an energy-dense transportable product. The conversion of renewable electricity into carbon-based chemicals and fuels via electrochemical CO_2 reduction can directly help both these efforts.

Depending on the composition and structure of the catalyst used in the electrochemical CO_2 reduction reaction, the product formed from CO_2 can be tuned towards different carbon-based compounds. In particular, d-band metals such as gold, silver and zinc are suitable for the selective production of CO, whereas copper binds the CO reaction intermediate more strongly, enabling further proton/electron transfers that drive the formation of higher order products.[1] Among these metals, silver is a promising candidate for the industrial synthesis of CO since it has a good balance between its relatively low cost and reasonable performance and stability.[2] To improve the performance of silver, a number of modified silver catalysts have been investigated which show significantly improved selectivity, activity, onset potential and stability versus their pure metallic counterpart. Strategies to improve the catalytic performance of silver have included doping with p-block elements and various nanostructuring approaches, among others.[3,4,5] Among these promising candidates are oxide-derived silver (ODAg) catalysts.[6] During the fabrication of oxide-derived silver, an anodic pulse is applied to the silver electrode, creating an oxide layer on top of the bulk metal. During CO_2 reduction, the silver oxide layer at the surface rapidly reduces back to metallic silver. For other metals, such as gold, copper and lead, oxide-derived techniques have also demonstrated improved performance metrics including increased CO_2 reduction selectivity and reduced overpotentials required to reach >1 mA/cm^2.[7,8,9] These treatments result in highly-porous electrode surfaces which impact the mass transport of reactants and products while altering the local pH and buffering abilities of the electrolyte near the catalyst's surface. Other research has suggested that the intrinsic activity of the oxide-derived metals are affected by sub-surface oxides[10,11] or new coordination sites[12] due to the formation of preferably-oriented surfaces and defect sites that form as a result of the OD treatment.

In the case of silver, a higher local pH near the electrode surface is further thought to influence the selectivity for CO formation over that of hydrogen.[6,13] When mass transport is limited by the porous nature of the electrode, hydroxide ions (OH^-) that are formed as a result of CO_2 and H_2O reduction accumulate near the surface resulting in a higher local pH than that of a flat surface. While a high local pH favours the CO_2

reduction reaction, it simultaneously supresses hydrogen evolution, providing an avenue to improve product selectivity on roughened nanoporous silver electrodes.

Apart from the changed electrolyte transport dynamics at the catalysts' surface, an alteration in the material properties as a result of the oxide-derived treatment, such as electronic, structural or compositional changes, can also give rise to the improved catalytic properties. Since oxide-derived silver catalysts are formed from a silver oxide, the potential presence of traces of oxygen and its role in improving the CO_2 reduction reaction were proposed in several papers.[11,10] If present, oxygen could help stabilise the CO_2 molecule when it arrives at the electrode surface, and thus may contribute to the enhanced selectivity towards CO_2 reduction. Since the rate-determining step for CO_2 reduction to CO on silver is the adsorption of CO_2, reducing the overpotential of this reaction step is then very important for increasing the overall efficiency and activity of the reaction.

Controversy exists regarding this hypothesis, however, as other studies using surface-characterisation techniques found no traces of oxygen in oxide-derived silver catalysts.[12] It is important to emphasise that many techniques capable of measuring trace amounts of elements, such as XPS, do so under high vacuums, which can remove oxygen from a silver oxide species. Other techniques such as Kelvin probe force microscopy (KPFM) that measure the work function can only give an indication as to whether trace amounts of oxygen might exist, but do not provide definitive proof or indications of how oxygen may be incorporated into the Ag catalyst. In situ and operando techniques are therefore needed to probe the catalyst's electronic, compositional, and atomic structure during electrolysis to distinguish any surface related affects that may lead to improved performance, from the beneficial effects caused by the nanostructured morphology and high local pH.

In this work, we use a combination of operando extended X-ray absorption fine structure (EXAFS), electrochemical methods, DFT calculations and ex situ characterisation such as grazing incidence X-ray diffraction (GIXRD) to examine the surface properties and catalytic activity of both silver and oxide-derived silver catalysts for electrochemical CO_2 reduction. We find a correlation between the Faradaic efficiency for CO formation with the measured concentration of oxygen in the silver lattice. These results suggest that the improved performance for oxide-derived silver catalysts may arise from a combination of increased activity of Ag induced by the presence of surface oxygen, and from a high local pH created through the nanostructured morphology. From these results, we propose several mechanisms via which the inclusion of atomic oxygen near the surface can aid the CO_2 reduction reaction over silver electrodes. In operando EXAFS data shows how vital in situ and operando techniques are to properly understand electrochemical systems.

3.2 Results and discussion

Catalyst characterisation. Oxide-derived silver catalysts were fabricated according to an earlier published method (Figure 3.1).[6] All experimental details are presented in appendix B. From electrochemical measurements, the ODAg catalyst has a lower onset potential, higher CO selectivity, higher activity (current density at a given potential) and improved stability compared to silver foil catalysts (Figure B2a and b). To make ODAg, a Ag foil is strongly oxidised by an oxidation/reduction-cycling treatment in an alkaline electrolyte. This treatment produces a silver oxide that quickly reduces back to metallic silver once a reducing potential is applied to perform CO_2 reduction. The initial few seconds of the CO_2 reduction experiment thus produces the final oxide-derived silver catalyst. In Figure 3.1a, the progression of the oxide-derived treatment is shown schematically (Ag foil, silver oxide and ODAg). We will denote the oxide precursor as AgO_x, since this oxide consists of a mixture of Ag_2O, AgO and Ag as appears from the XRD pattern (Figure B3).

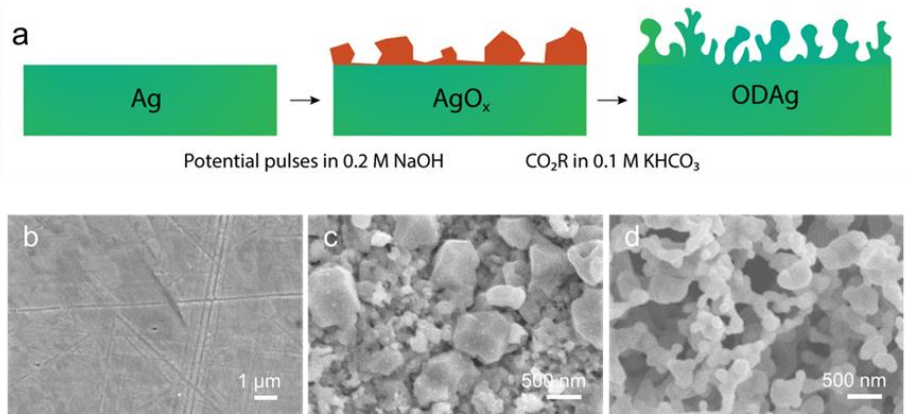

Figure 3.1. (a) Fabrication scheme of oxide-derived silver (ODAg), silver is denoted by green, silver oxide by dark orange. SEM images show how the surface morphology changes drastically when (b) silver is (c) oxidised to AgO_x and (d) reduced to form ODAg.

To understand the underlying reasons for the difference in CO_2 reduction performance between Ag and ODAg, a number of materials characterisation techniques were performed. While the morphology of ODAg (Figure 3.1b and d) is vastly different than that of Ag foil, the surface composition as measured by XPS is similar for the two catalysts (Figure 3.2a-d). XPS spectra were recorded ex situ, so contamination from air could not be avoided due to the transport from the electrochemical cell to the XPS instrument.

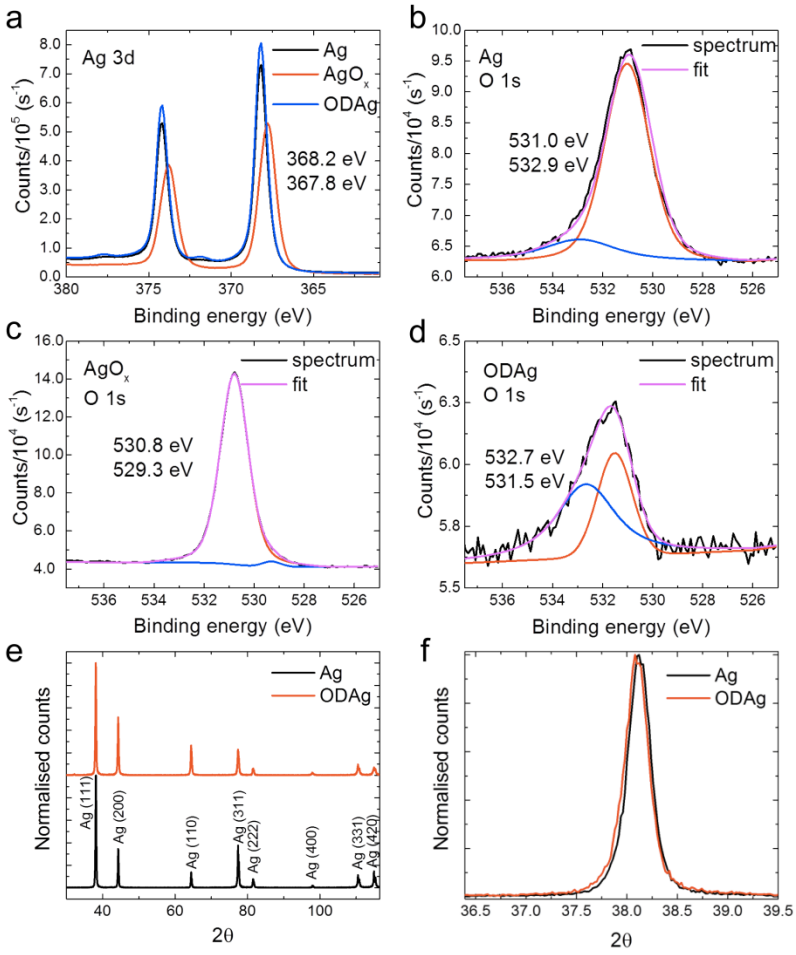

Figure 3.2. (a) Ag 3d XPS spectra of Ag, the silver oxide precursor and ODAg. The precursor is not metallic but an oxide, as can be concluded from the shift in the Ag 3d peak. The O 1s spectrum and its fit of (b) Ag, (c) AgO_x and (d) ODAg, the red and blue lines indicate the deconvoluted peaks. (e) and (f) are GIXRD patterns of Ag and ODAg. (e) When the spectra are normalised it becomes apparent that Ag (220) grows relative to Ag (111). (f) There is no significant strain in the ODAg catalyst.

The silver foil and ODAg have very similar Ag 3d spectra with a peak at 368.2 eV and a satellite peak at 371.9 eV (Figure 3.2a). The combination of these peaks is ascribed to metallic silver.[14] The AgO_x precursor was also examined by XPS, and in this sample the silver binding energy shifted to 367.8 eV, along with a disappearance of the satellite peak. This agrees well with literature values for Ag_2O.[14] Since AgO is notoriously unstable in ultra-high vacuum, its presence cannot be confirmed nor rejected.[14,15] Detailed scans of the O 1s region were also recorded but not very insightful (Figure 3.2b-d), because Ag-O contributions can overlap with carbonate groups from air

contamination in the O 1s region.[16,17] The only definitive assignment that can be made in the O 1s spectrum in Figure 3.2c is the small peak at 529.3 eV, ascribed to Ag_2O.[18] It is surprising that this peak is so small since the shift in the corresponding Ag 3d spectrum seems to indicate pure silver(I) oxide. The larger peak at 530.8 eV of the O 1s spectrum could be ascribed to oxygen chemisorbed on a silver surface[17] or Ag-O-Ag bonds[19] but not to pure Ag_2O. The higher binding energies of the O 1s in the Ag and ODAg sample can mainly be ascribed to contamination from air (note that these peaks are 3 and 10 times smaller than the AgO_x sample, respectively), although their binding energy is also very close to a species described as subsurface O in silver at 531.2 eV.[16] Since the binding energies of contamination and silver-oxygen bonds overlap, it is difficult to draw significant conclusions from the O 1s spectra. It is therefore necessary to use other characterisation techniques to properly investigate the electronic and compositional differences between Ag and ODAg.

To see whether there are any structural changes between Ag and ODAg, grazing incidence X-ray diffraction (GIXRD) patterns were measured and compared. To be more sensitive to the surface of the catalyst and to be able to measure all reflections (not just the reflections parallel to the surface as for the standard Bragg-Brentano XRD configuration), GIXRD was chosen as the most suitable XRD technique. A change in the ratio between (111) and (220) can be observed in the GIXRD data measured at a grazing incidence angle of 4° θ of oxide-derived silver compared to the pure silver foil (Figure 3.2e). For the ODAg films, the ratio (220) over (111) is higher compared to that of untreated Ag. The presence of the (220) peak is an indirect proof of the presence of (110) which is not visible in the XRD pattern since it is a forbidden reflection for a fcc lattice. The increased (220) reflection is already observed in the silver oxide pattern, in addition to several smaller peaks representing both Ag_2O and AgO structures (Figure B3).

The Ag (110) facet was shown by both experimental[20] and theoretical[5] work to be more active than the very stable (111) facet, thus the increased presence of the (220) reflection in the ODAg electrodes could potentially explain the improved electrocatalytic activity and selectivity. However, one should keep in mind that XRD, even when measured in grazing incidence mode, is still a bulk technique that will penetrate several hundreds of nanometres into the catalyst material. This means that even though the facets underlying the surface can be more (110) orientated in the case of ODAg, this does not prove that the actual surface facets are also (110). We can however say from the uniformity found in the peak shape (Figure 3.2f) that the lattice is not strained in a higher or lower degree than the silver foil, nor that the crystallite size seems to have changed.

To better understand the cause of improved electronic, compositional or short-range structural difference between Ag and ODAg, a short-range order characterisation technique that can be used under real operating conditions is required.

Operando X-ray absorption spectroscopy. X-ray absorption fine structure spectroscopy (XAFS) is widely used to study materials and systems operando or in situ due to the high energy X-rays that can be used; the X-rays can easily penetrate through air, water and various soft materials that are generally used to build an electrochemical cell.[21] XAFS is divided into X-ray absorption near-edge spectroscopy (XANES) and extended X-ray absorption fine structure (EXAFS). The XANES spectra provide information on the oxidation state, geometry and electronic configuration of the absorber atom while EXAFS data fitting allows the ability to reconstruct its local environment to give the concentration of neighbouring atoms (N), the absorber atom's distance to the neighbouring atom (R), and disorder (Debye-Waller factor: σ^2) on a short length scale.

X-ray absorption spectra were recorded at the Dutch-Belgian beamline (DUBBLE, 26A) of the European Synchrotron Radiation Facility (ESRF) in Grenoble, France at the silver K-edge (25515.59 eV). Figure 3.3a shows the Fourier transforms of reference transmission EXAFS spectra for a 5 μm Ag thin film and pellets of silver(I) oxide and silver(II) oxide powder dispersed in a cellulose matrix. The EXAFS spectra are extracted and fitted according to the EXAFS equation (Chapter 1, equation 1.10); the data analysis details are reported in Appendix B. Due to the limited energy (k= 2.5-10) range achievable in the operando conditions, the data analysis has been mainly focused on the first two nearest neighbours (coordination shells) of the silver absorber atom: the Ag-O and Ag-Ag coordination shells. The fitting results of the reference metal and oxides in Figure 3.3a are reported in Table 3.1.

The reference samples were measured in transmission mode to ensure optimal data quality and to avoid self-absorption processes.[22] However, for samples measured in an electrochemical cell, the total sample + cell thickness would be too large for the X-rays to travel through, therefore all sample measurements were taken in fluorescence mode. It is common practice to do this at a configuration where the incident X-rays make a 45° degree angle to the sample. However, EXAFS is a bulk technique and high energy X-rays at 45° will penetrate into the sample >10 μm (Figure 3.3b). In order to reduce the penetration depth and give more information from the near surface region, we again used a grazing incidence mode. Using this approach, the X-ray beam is only able to probe the surface of the catalyst and will provide surface-sensitive information.[23]

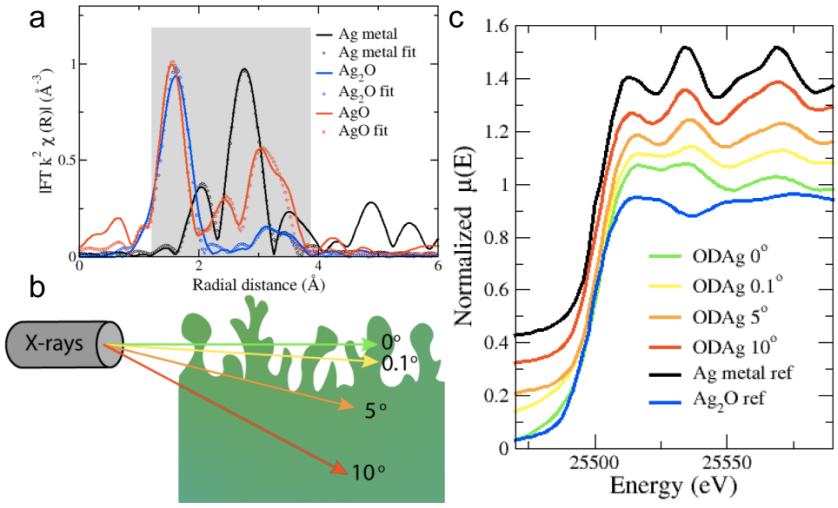

Figure 3.3. (a) k^2 -weighted Fourier transformed EXAFS transmission spectra of silver and silver oxide reference samples. Grey shadow denotes fitted area. (b) A schematic showing how the grazing incidence X-rays penetrate the ODAg. (c) Normalised XANES spectra of the transmission metal and Ag_2O references compared to ex situ oxide-derived silver samples, showing the difference in chemical composition of the film when the X-rays penetrate less deep into the material.

Table 3.1. EXAFS fitting results of Figure 3.3a. Fitted R (Ag-Ag or Ag-O distance), N (coordination numbers) and σ^2 (Debye-Waller factor) of the first shell. Errors in parentheses.

Sample	Bond	R_1 (error R_1)	N_1 (error N_1)	σ^2_1 (error σ^2_1)
Ag metal	Ag-Ag	2.86 (0.001)	12.00 (0.2)	0.007 (0.0003)
Ag_2O	Ag-O	2.06 (0.001)	1.99 (0.4)	0.004 (0.0001)
	Ag-Ag	3.34 (0.02)	7.51 (0.7)	0.036 (0.0009)
AgO	Ag-O	2.02 (0.02)	1.99 (0.5)	0.003 (0.008)
	MS[a]	2.66 (0.09)	5.16 (0.9)	0.04 (0.008)
	Ag-Ag	3.29 (0.005)	11.5 (2.3)	0.02 (0.003)

The probing depth into the sample is demonstrated in Figure B4, which shows the attenuation length of the X-ray beam into silver as a function of the incident angle of the X-rays. The attenuation length is defined as the depth into the material (along the surface normal) where the X-ray beam intensity drops to 1/e of its original value. When the sample is tilted only 0° or 0.1° with respect to the incoming X-rays, for instance, the beam is only expected to penetrate the first 2 or 3 nm of the sample. Figure 3.3c shows the

striking difference in the measured XANES spectra of an ex situ ODAg sample that was used in CO_2 reduction before the EXAFS measurement as a function of varying angles of incidence. Interestingly, when the XANES spectrum is taken at 10° (red line, penetration depth of 3 μm) (Figure 3.3c), the spectrum appears similar to pure metallic silver (black line). The XANES spectra of ODAg obtained at shallow angles (0° and 0.1°), however, are not reminiscent of either a pure metallic compound nor a pure silver oxide (blue line). Instead, the samples seem to be a mixture of both metallic and oxide composition, which can be seen from the second feature after the edge at 25534.1 eV; for metallic silver, this feature is 2 times higher than the first feature at 25512.8 eV, for the ODAg samples at 0° and 0.1° they are similar in size. This can be understood as a mixture of the metallic positive contribution and the oxide depression at the same energy. The spectrum measured at 5° (orange line, penetration depth of 1.7 μm) seems more metallic than the 0° and 0.1° spectra but not as strongly metallic as the 10° spectrum. This result highlights how important it is to measure in grazing incidence mode to ensure we observe mainly the surface of the silver electrocatalysts and to reduce bulk metallic signals as much as possible. These results also conclude that our oxide-derived fabrication method only modifies the first ~2 μm of the Ag foil, while the rest of the 250 μm foil remains pure silver, as can be concluded from Figure B4.

While giving important information, XANES cannot, however, provide enough information to properly understand the electronic, structural or compositional properties of the catalysts. Instead, EXAFS spectra are recorded and fitted to provide this information. To ensure that the oxide-like structure found in ex situ spectra are not just the results of spontaneous self-oxidation in air, the spectra are acquired under electrochemical operating conditions.

A schematic of the custom-made cell used to acquire the operando EXAFS spectra is shown in Figure 3.4a and a photograph of the cell is given in Figure B5. The design consists of a flow cell where the working electrode (WE) (the silver electrocatalyst) faces up. The WE was covered by a 0.5 mm layer of 0.1 M $KHCO_3$ electrolyte which was kept saturated with CO_2 in a reservoir outside of the cell. A 0.5 mm polypropylene (PP) window was clamped on top of the electrolyte allowing for transmission of the X-rays. The reference (RE) and counter electrode (CE) were positioned in the vertical parts of the electrolyte flow; with the RE placed just before and the CE just after the WE. The fluorescence detector was placed in close proximity to the WE. The cell was then mounted on a motorised stage that could rotate with respect to the incoming X-ray beam, to allow full control over the angle of incidence. While we were able to perform ex situ sample measurements at extremely low grazing angles, such low angles are not possible during in situ or operando measurements. At an angle of 0.1°, for example, the distance that the beam would have to travel through the polypropylene window and electrolyte layer becomes almost 60 cm, making cell design and alignment difficult,

while resulting in large signal attenuation before the beam can reach the sample. Therefore the angle was increased to 6° for operando measurements, which results in a beam travelling distance through the electrolyte and polypropylene of roughly 1 cm. In this configuration, the polypropylene window and electrolyte transmit about 70% of the photons while the attenuation length of the X-rays into the silver was 1.9 μm, which closely resembles the previously observed thickness of the ODAg layer. It is quite remarkable that it is possible to measure operando EXAFS under a grazing incidence angle of only 6°, since it creates a beam path length through the electrolyte and polypropylene of 1 cm. The ability to gain meaningful information from this experiment is further made possible because silver is a heavy element: the high energy (25515.59 eV) is able to pass through 1 cm of material while losing only 30 % of its photons.

The results of these 6° measurements are shown in Figure 3.4b where the Fourier transform of an ODAg sample is compared to that of a pure silver foil, both measured under operando conditions. Both spectra are corrected for self-absorption using the transmission spectrum of silver foil (Figure 3.3a) as a reference to obtain reasonable coordination numbers. The EXAFS in K-space $k^2\chi(k)$ and first derivative of $\mu(E)$ are presented in Figure B6a and B6c. Due to the electrolyte layer and the room temperature conditions, the longer range order of the samples could not be properly measured. The Fourier transformed spectra were fit for the first two shells: a Ag-O shell and the first Ag fcc Ag-Ag shell (Table 3.2). For both the transmission foil and the Ag foil measured during CO_2 reduction, the Ag-O shell was not observed during the fitting process. This is expected since oxygen is normally not found in a silver fcc lattice. For the ODAg silver however, a coordination number of 0.69 for the Ag-O shell was obtained. Interestingly, the Ag-O distance in our ODAg is longer then it would be in Ag_2O or AgO: 2.28 Å compared to 2.07 Å.[24] Similar values for the Ag-O distance and coordination number have been shown before in literature where small Ag nanoparticles were deposited on a silica support.[25] In this case, Balerna et al. explain the Ag-O bond as the bond between the oxygen of the silica and the Ag nanoparticles. Note that due to the relatively long interatomic distance, the binding energy is weaker than that of a pure silver oxide and thus the oxidation state of silver will be between Ag^0 and Ag^+.

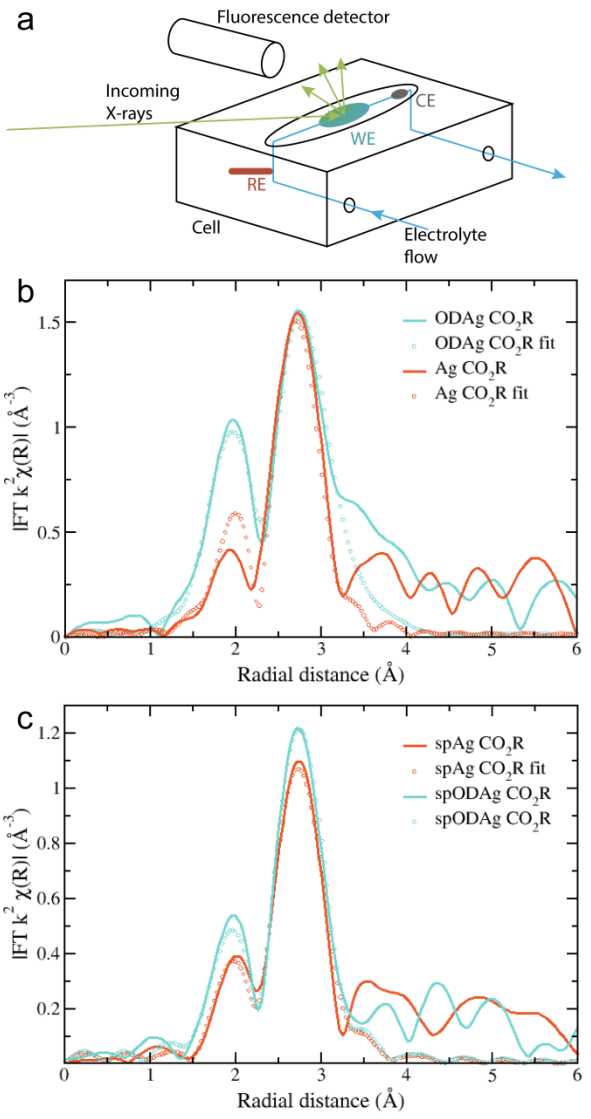

Figure 3.4. (a) A schematic of the home-made flow cell used for the operando EXAFS measurements. (b) k^2-weighted Fourier transformed EXAFS fluorescence spectra of (b) a Ag catalyst and an ODAg catalyst and of (c) a spAg catalyst and a spODAg catalyst during CO_2 reduction. Fitted region is 1.5 to 3.2 Å.

Table 3.2. EXAFS fitting results of Figure 3.4b. Fitted R (Ag-Ag or Ag-O distance), N (coordination numbers) and σ^2 (Debye-Waller factor) of the first shell. Errors in parentheses. When no error is reported, the value was restricted during the fitting process.

Sample	Bond	R_1 (error R_1)	N_1 (error N_1)	σ^2_1 (error σ^2_1)
Ag CO_2R	Ag-O	0	0	0
	Ag-Ag	2.86 (0.07)	12.00	0.013 (0.01)
OD-Ag CO_2R	Ag-O	2.28 (0.05)	0.69 (0.2)	0.001 (0.0006)
	Ag-Ag	2.88 (0.02)	11.44 (2.6)	0.02 (0.0004)

These results are remarkable, especially when compared to the ex situ XPS spectra, which were not able to identify oxygen as part of the oxide-derived silver. The ultra-high vacuum conditions needed to acquire XPS data might make the ODAg self-reduce to Ag^0. Considering the presence of oxygen that was observed in the EXAFS data which has a long bond distance, the electron sharing between the silver and the oxygen is smaller than in a pure oxide, which makes the weakly bound O quite susceptible to removal in vacuum conditions. This could explain why other reports on oxide-derived silver systems have not been able to identify oxygen as an active component in CO_2 reduction.

Sputtered Ag and Ag foil. During previous experiments at -0.8 V vs. RHE, it was noticed that a sputtered silver layer on a Ti foil provided a higher selectivity towards CO of 51% than pure Ag foil with a Faradaic efficiency of 25% (Figure B2). In order to check whether this difference could correlate with the long oxygen bond we found for ODAg, we fabricated sputtered ODAg (denoted as spODAg) and compared the EXAFS spectra of this sample and an otherwise untreated sputtered silver film (spAg) with the Ag and ODAg samples made from Ag foil. The spAg catalyst was made by sputtering a 600 nm layer of Ag on Ti foil (spAg, SEM image in Figure B7a) and the treated catalyst, spODAg, was fabricated through the same method as ODAg but using the sputtered Ag on Ti as the substrate (SEM image in Figure B7c). GIXRD and XPS data on these samples can be found in Figure B8 and B9, respectively. Because the total silver layer for the sputtered catalysts is much thinner, the self-absorption correction for the acquired EXAFS data was not necessary. Accordingly, the spectra were fitted without any self-absorption correction. The EXAFS in K-space $k^2\chi(k)$ and first derivative of $\mu(E)$ are presented in Figure B6b and B6d. Interestingly, whereas the Ag and ODAg show a rather large difference in EXAFS spectra, the sputtered spAg and spODAg are quite similar to each other (Figure 3.4c). They can both be fit by a Ag-O shell and a Ag-Ag shell (Table 3.3). The Ag-O shell gives a very low coordination number of 0.26 for spAg and 0.24 for spODAg. The Ag-O distances are 2.32 and 2.23 Å for spAg and spODAg, respectively. These oxygen species might originate from the sputtering treatment used

to deposit the silver layer. The silver-silver shell of the spAg and the spODAg have coordination numbers of 8.60 and 9.77, respectively, indicating a small reactive silver cluster size.[12,25] These clusters might spontaneously react to air, forming the Ag-O species.

Table 3.3. EXAFS fitting results of Figure 3.4c. Fitted R (Ag-Ag or Ag-O distance), N (coordination numbers) and σ^2 (Debye-Waller factor) of the first shell. Errors in parentheses. When no error is reported the value was restricted during the fitting process.

Sample	Bond	R (error R)	N (error N)	σ^2 (error σ^2)
spAg CO_2R	Ag-O	2.32 (0.03)	0.24 (0.1)	0.005
	Ag-Ag	2.84 (0.02)	8.60 (0.5)	0.013 (0.0005)
spODAg CO_2R	Ag-O	2.23 (0.03)	0.26 (0.02)	0.005
	Ag-Ag	2.85 (0.006)	9.77 (0.7)	0.014 (0.0003)

Model clusters. The absolute amount of oxygen given by the coordination number can be better understood when it is compared to model systems. Metallic silver clusters of different sizes, surrounded by oxygen atoms taken from a silver oxide shell were modelled, and shown in Figure 3.5.

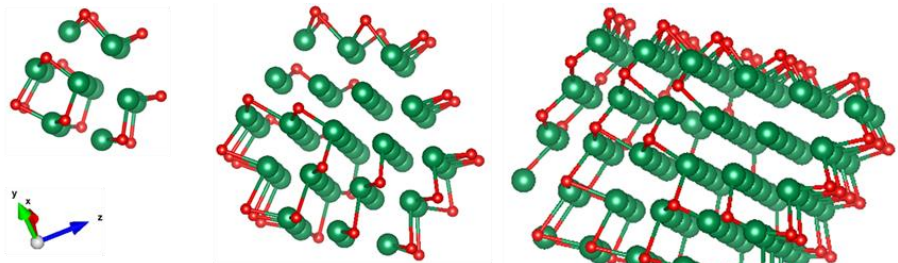

	No. of Ag-Ag shells	Coordination number Ag-O	Oxygen amount
Left	2	1.97	48%
Middle	3	0.37	37%
Right	4	0.21	36%

Figure 3.5. Silver clusters consisting of 2, 3 and 4 Ag-Ag shells were modelled with one Ag-O shell as the outer shell. Note that in this 2D image, the oxygen appears to be dispersed throughout the cluster, in reality it is only present at the outer edge of the cluster. Red is oxygen, green is silver.

These clusters gave an average Ag-O distance of 2.3 Å. The theoretical average coordination number of the Ag-O shell was calculated and can be compared to our experimental data. For a very small cluster consisting of only 2 Ag-Ag shells, the Ag-O coordination number is 1.97, roughly the same as for pure silver oxide. However, when

we increase the cluster size to 3 or 4 Ag-Ag shells, the Ag-O coordination numbers drop to 0.37 and 0.21 respectively. The large decrease in coordination number for these very small clusters shows how quickly the Ag-O component drops to 0 and thus below the EXAFS detection limit. Since our experimental data shows non-zero coordination numbers, we can conclude that we have a polydisperse silver with very small single crystal clusters that contain oxygen. When we compare this to our experimental data, the amount of oxygen we find by fitting is certainly not negligible. The 2-shell cluster contains 48% of oxygen, the 3- and 4-shell clusters contain 37% and 36% oxygen, respectively. Since many of the silver atoms are so far away from the oxygen atoms, the averaged coordination number still decreases quickly with cluster size.

CO_2 electrolysis. All catalysts examined above were also tested for CO_2 reduction, focusing on their activity and selectivity at -0.8 V vs. RHE. The trend in faradaic efficiency for CO is as follows: Ag < spAg < spODAg < ODAg (Figure B2). Since ODAg has a seven times larger electrochemical surface area (ECSA) than Ag (Figure 3.6a), the difference between their CO selectivity can possibly be explained with the local pH-effect: the local pH at the silver surface is increased by the formation of CO and H_2 (since these half reactions consume water molecules and produce hydroxide ions (OH^-)), as shown in reaction 3.1 and 3.2.

$$CO_2 + H_2O + 2e^- \rightarrow CO + 2OH^- \quad 3.1$$

$$2H_2O + 2e^- \rightarrow H_2 + 2OH^- \quad 3.2$$

The hydroxide ions have to travel to the anode to act as reactants in the oxygen producing half reaction. The catalyst's surface porosity inhibits fast OH^- exchange between the reaction site and the bulk electrolyte, thus creating a higher pH at the nanostructured silver surface which favours CO production while supressing H_2 evolution.

However, the pure Ag foil and the spAg have quite a selectivity discrepancy between them, and the local pH effect alone cannot account for this since they are both relatively flat enough to not have any mass transfer limitations based on porosity, in fact their ECSAs are almost identical (Figure 3.6a). Interestingly, the spAg and spODAg have a factor 4 difference in surface area, but only a small difference in FE_{CO}. Whereas some of the differences in CO selectivity can be explained by the local pH effect due to the nanostructured morphology of the samples, there seems to be another factor that also benefits the improvement in CO_2 reduction selectivity. When the CO_2 selectivity is compared with the concentration of Ag-O bonds found by EXAFS fitting, we find similar trends. The O/Ag ratio (defined as the ratio between the Ag-O coordination number and the Ag-Ag coordination number) follows roughly the same trend as the FE of CO

(Figure 3.6b) and may therefore play a critical role in the improved CO selectivity of both sputtered silver and oxide-derived silver as compared to silver foil.

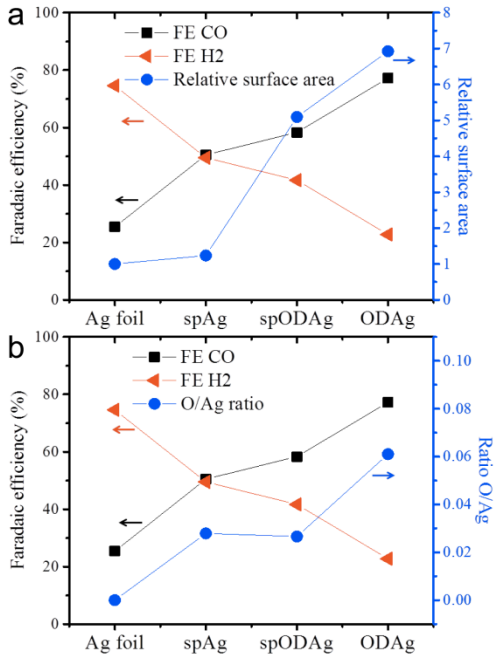

Figure 3.6. (a) The relation between the selectivity of the catalysts and the relative surface area (as determined by the double layer capacitance, where the relative surface area of the Ag foil is taken as 1). (b) The relation between the catalyst selectivity and the O concentration found in the catalyst as calculated by the ratio between the coordination numbers of the Ag-O and Ag-Ag shell found by EXAFS fitting of the operando measurements.

It is necessary to put these results in the context of previous findings in order to extrapolate deeper meaning. Over the past years, a number of reports have been published about silver-based nanostructured electrocatalysts that all have a precursor containing a form of silver oxide.[10,11,12,19,26] During CO_2 reduction these catalysts reduce back to a nanostructured form of metallic silver. All of these catalysts can thus fall within the class of oxide-derived silver catalysts, although they have different fabrication methods and starting morphologies/compositions. Different possible explanations were given in these reports that try to elucidate the active component within these catalysts. It seems quite likely that there are a number of factors that together create such active and selective catalysts; thus it is fair that the effects of local pH, higher surface areas and residual oxygen species are in essence, not mutually-exclusive. Strikingly, whereas some of these previous works claim to have found traces of oxygen in their

catalyst, to which they attribute to the improved catalytic performance, others claim to be certain oxygen has completely disappeared from the catalysts' surface and can therefore not contribute to the reaction. A range of different characterisation techniques were employed to try and find the presence of oxygen. The difficulty with many of these measurement techniques is that they are often recorded ex situ, so the composition of the catalyst may be different during electrolysis than under vacuum/air characterisation. Some of the characterisation techniques give indirect information about the catalyst structure: a change in work function as measured by Kelvin Probe Force Microscopy (KPFM) or Ultraviolet Photoelectron Spectroscopy (UPS) could indicate increased oxygen levels but it could also mean higher impurity levels or a different crystal facet exposure. Another difficulty lies in the bulk sensitivity of some techniques: both X-ray diffraction (XRD) and X-ray absorption spectroscopy (XAS) probe several micrometres far into the bulk, thus the contributions from the surface of the catalyst can be masked by signals from the bulk. An extra complication with XRD is that the presence of certain facets in the bulk has no real link to the presence of that same facet on the surface; often surfaces will rearrange to the most stable formation possible, regardless of their bulk structure. The last issue is the use of ultra-high vacuum characterisation techniques: silver oxides are not very stable, and they can reduce to metallic silver under ultra-high vacuum conditions.[14] This means that a lack of oxygen in an XPS or Auger spectrum is not representative of the state of the same catalyst under ambient or electrochemical conditions. Besides this it can be difficult to obtain conclusive results from XPS spectra. A Ag 3d peak will not shift far from metallic silver when weakly bound to an oxygen atom. As discussed above, the O 1s spectrum has many contributions from both silver and contamination that are hard to assign.

The discrepancy in these previous studies then highlight the importance of techniques that can measure a catalyst's surface under actual reaction environments, either in ambient or under operating conditions. These efforts are important to gain information about the catalyst in its working state.

Based upon the findings of our work, the presence of O in the ODAg catalyst seems to be acting as a dopant, similar to other non-metallic p-type dopants such chloride[27], iodide[4] and even amine or thiol groups[28]. For these doped silver catalysts, it has been shown that trace amounts of non-metallic species such as I or Cl can have a significant effect on the selectivity and activity of CO_2 electroreduction, and therefore most likely impact the reaction mechanism. Therefore, in addition to the impact of the nanostructured morphology on the local reaction environment, the electronic effect of oxygen should also be taken into account. A similar conclusion has been recently found by Zhou et al., who used EXAFS to show how partial positive charges induced by boron doping on copper can stabilise CO_2 reduction intermediates.[29]

Bond length calculations. To strengthen the understanding of the presence of oxygen in a Ag catalyst for improved CO_2 electroreduction, DFT calculations and a Bader charge analysis were performed to determine the bond length and partial charge of the long Ag-O bond, presented in Figure 3.7a. In a low-coverage case on Ag(110), the two most favourable sites for an oxygen atom to sit on are the hollow and the long-bridge site. Of these two different sites, the hollow site provides the most stable configuration. The bond lengths found for these scenarios closely resemble the Ag-O distances that were found in EXAFS fitting. Therefore we assume that the long Ag-O bond is situated in the ODAg in a similar manner to what is calculated here and has a partial charge of $O^{-0.95}$ as calculated from the Bader analysis. The positive charge on the silver is shared by many atoms and is thus small: $Ag^{+0.17}$ for atoms close to the oxygen.

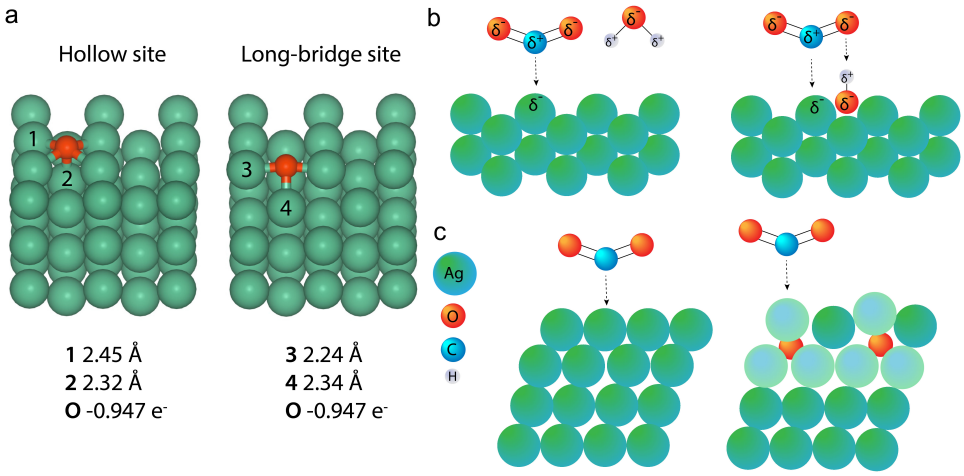

Figure 3.7. (a) DFT calculations and Bader analysis for O on a Ag (110) slab give Ag-O bond lengths very similar to those found in the EXAFS data fitting. (b) Left: a CO_2 molecule binds to a Ag(110) facet in the presence of a water molecule. Right: The presence of oxygen in the cavities of a silver (110) facet can facilitate the binding of CO_2 to the silver through the presence of a shared proton. (c) Left: a CO_2 molecule binding to a Ag(111) surface. Right: subsurface O below Ag (111) facets shift the d-band of silver toward the Fermi level (indicated by a change in color of the affected Ag atoms), increasing the reactivity of the subsurface O-Ag(111) facet compared to Ag(111).

Potential mechanisms as a result of the presence of oxygen. The role of oxygen in the silver lattice can now be explained by several hypotheses. The first hypothesis would be that the observed oxygen is part of a reaction intermediate of the CO_2 reduction. This hypothesis seems unlikely since the Ag-O is also observed in the ex situ samples (Figure 3.7b). In addition, if oxygen were part of a reaction intermediate, this would mean that we are able to observe a single monolayer of material using a bulk technique (EXAFS), which seems unlikely.

Another hypothesis relates to the bond lengths found by the DFT calculations. The hollow or long-bridge site in the silver (110) facet if exposed to the electrolyte can host oxygen atoms, as is shown in Figure 3.6a. If these oxygen atoms bound to CO_2 directly, a stable and thus unreactive carbonate species would formed. If instead a proton would bind to the oxygen on the silver surface first, the combination of a negatively charged silver atom next to a positively charged proton would present the perfect substrate for a CO_2 molecule to bind to. This is schematically presented in Figure 3.6b: the proton can initially be shared between the silver-oxygen and the CO_2-oxygen, but once CO_2 is properly adsorbed on the surface the proton can become exclusively bound to CO_2, forming the well-known COOH intermediate.[30] This hypothesis relies on the presence of oxygen in Ag(110) facets. However, the fact that our GIXRD studies show an increased concentration of silver (110), does not necessarily prove that (110) is present in higher concentrations at the surface of ODAg. Nevertheless, due to the increased roughness on the nanoscale (Figure 3.1d and B6c), we can say with high confidence that the exposed facets will contain many defects, kinks and other types of stepped sites. These sites can also facilitate the presence of oxygen atoms that bind to protons and follow a similar reaction mechanism as explained for the (110) facet. The low coordination number of spAg (Table 3.3) also indicates many such defects exist on this catalyst. Once the atomic oxygen sits at such a site, it also becomes more difficult for the Ag to rearrange to a more stable surface configuration, meaning the presence of the oxygen actually stabilises the defects and the activity of the ODAg can be maintained more easily.

Another hypothesis stems from heterogeneous catalysis. In the field of ethylene epoxidation catalysed by silver, subsurface oxygen is found to have a very important role in increasing the reactivity of the catalyst.[31,32] It was found that the presence of subsurface oxygen shifts the d-band towards the Fermi level, increasing the reactivity of silver as schematically depicted in Figure 3.7c.[31] It is known that for d-band metals, a valence band (i.e. metal d-band centre) closer to the Fermi level increases reactivity for the metal. This effect on CO_2 reduction was demonstrated for gold-copper nanoparticles.[33] Since the (111) facet is the most energetically stable surface facet for silver, it is imaginable that it is still present in large quantities at the rough ODAg surface. When the mixed silver oxide quickly reduces back to form ODAg (Figure 3.1a), some oxygen atoms can become stuck in a potential well, meaning that the energy barrier to reduce the last remaining oxygen atoms can be quite high when there is no other oxygen around to form molecular O_2. Below the surface of the catalyst this seems like a plausible scenario. This creates silver atoms in close proximity to the subsurface O that are more reactive than before the oxide-derived treatment and can more easily bind CO_2 to form COOH.

3.3 Conclusions

We have shown how the use of operando EXAFS has identified the presence of a long Ag-O bond where the oxygen may be a key participant in the reduction of CO_2 to CO on oxide-derived silver catalysts. The silver needs a long and thus atomic oxygen bond in order to alter its reactivity and improve its susceptibility to CO_2 binding. Both the presence of oxygen and nanostructuring of the catalyst to increase the local pH aid the activity and selectivity for CO production on silver electrocatalysts and are therefore vital components of an active and selective CO_2 reduction catalyst. The knowledge gained from this research can hopefully help to design future silver-based CO_2 reduction catalysts.

In recent years, many groups have looked into the possible presence of oxygen species remaining after CO_2 reduction and competing conclusions were drawn from these studies. We hope to positively contribute to the scientific discussion by adding operando results that are surface sensitive enough to measure the catalytically active surface layer.

3.4 References

(1) Hori, Y. Electrochemical CO2 Reduction on Metal Electrodes. In Modern Aspects of Electrochemistry No. 42; Vayenas, C. G., Gamboa-Aldeco, M. E., White, R. E., Eds.; Springer: New York, 2008; pp 89–189.

(2) Kuhl, K. P.; Hatsukade, T.; Cave, E. R.; Abram, D. N.; Kibsgaard, J.; Jaramillo, T. F. Electrocatalytic Conversion of Carbon Dioxide to Methane and Methanol on Transition Metal Surfaces. J. Am. Chem. Soc. 2014, 136, 14107–14113.

(3) Larrazábal, G. O.; Martín, A. J.; Mitchell, S.; Hauert, R.; Pérez-Ramírez, J. Synergistic Effects in Silver–indium Electrocatalysts for Carbon Dioxide Reduction. J. Catal. 2016, 343, 266–277.

(4) Zhang, Y.; Ji, L.; Qiu, W.; Shi, X.; Asiri, A. M.; Sun, X. Iodide-Derived Nanostructured Silver Promotes Selective and Efficient Carbon Dioxide Conversion into Carbon Monoxide. Chem. Commun. 2018, 54.

(5) Rosen, J.; Hutchings, G. S.; Lu, Q.; Rivera, S.; Zhou, Y.; Vlachos, D. G.; Jiao, F. Mechanistic Insights into the Electrochemical Reduction of CO2 to CO on Nanostructured Ag Surfaces. ACS Catal. 2015, 5, 4293–4299.

(6) Ma, M.; Trzesniewski, B. J.; Xie, J.; Smith, W. A. Selective and Efficient Reduction of Carbon Dioxide to Carbon Monoxide on Oxide-Derived Nanostructured Silver Electrocatalysts. Angew. Chemie - Int. Ed. 2016, 55, 9748–9752.

(7) Chen, Y.; Li, C. W.; Kanan, M. W. Aqueous CO2 Reduction at Very Low Overpotential on Oxide-Derived Au Nanoparticles. J. Am. Chem. Soc. 2012, 134, 19969–19972.

(8) Verdaguer-Casadevall, A.; Li, C. W.; Johansson, T. P.; Scott, S. B.; McKeown, J. T.; Kumar, M.; Stephens, I. E. L.; Kanan, M. W.; Chorkendorff, I. Probing the Active Surface Sites for CO Reduction on Oxide-Derived Copper Electrocatalysts. J. Am. Chem. Soc. 2015, 137, 9808–9811.

(9) Lee, C. H.; Kanan, M. W. Controlling H+ vs CO2 Reduction Selectivity on Pb Electrodes. ACS Catal. 2015, 5, 465–469.

(10) Jiang, K.; Kharel, P.; Peng, Y.; Gangishetty, M. K.; Lin, H.-Y. G.; Stavitski, E.; Attenkofer, K.; Wang, H. Silver Nanoparticles with Surface-Bonded Oxygen for Highly Selective CO2 Reduction. ACS Sustain. Chem. Eng. 2017, 5, 8529–8534.

(11) Jee, M. S.; Kim, H.; Jeon, H. S.; Min, B. K.; Hwang, Y. J.; Min, B. K.; Hwang, Y. J.; Chae, K. H.; Min, B. K. Stable Surface Oxygen on Nanostructured Silver for Efficient CO2electroreduction. Catal. Today 2017, 288, 48–53.

(12) Mistry, H.; Choi, Y.-W.; Bagger, A.; Scholten, F.; Bonifacio, C.; Sinev, I.; Divins, N. J.; Zegkinoglou, I.; Jeon, H. S.; Kisslinger, K.; et al. Enhanced Carbon Dioxide Electroreduction to Carbon Monoxide over Defect Rich Plasma-Activated Silver Catalysts. Angew. Chemie Int. Ed. 2017, 56, 1–6.

(13) Yoon, Y.; Hall, A. S.; Surendranath, Y. Tuning of Silver Catalyst Mesostructure Promotes Selective Carbon Dioxide Conversion into Fuels. Angew. Chemie - Int. Ed. 2016, 128, 15508–15512.

(14) Kaspar, T. C.; Droubay, T.; Chambers, S. A.; Bagus, P. S. Spectroscopic Evidence for Ag(III) in Highly Oxidized Silver Films by X-Ray Photoelectron Spectroscopy. J. Phys. Chem. C 2010, 114, 21562–21571.

(15) Lützenkirchen-Hecht, D.; Strehblow, H. H. Anodic Silver (II) Oxides Investigated by Combined Electrochemistry, Ex Situ XPS and in Situ X-Ray Absorption Spectroscopy. Surf. Interface Anal. 2009, 41, 820–829.

(16) Boronin, A. I.; Bukhityarov, V. I.; Vishnevskii, A. L.; Boreskov, G. K.; Savchenko, V. I. XPS and UPS Studies of Oxygen Adsorption over Clean and Carbon-Modified Silver Surfaces. Surf. Sci. 1988, 201, 195–210.

(17) El Mel, A. A.; Stephant, N.; Hamon, J.; Thiry, D.; Chauvin, A.; Chettab, M.; Gautron, E.; Konstantinidis, S.; Granier, A.; Tessier, P. Y. Creating Nanoporosity in Silver Nanocolumns by Direct Exposure to Radio-Frequency Air Plasma. Nanoscale 2016, 8, 141–148.

(18) Wei, W.; Mao, X.; Ortiz, L. A.; Sadoway, D. R. Oriented Silver Oxide Nanostructures Synthesized through a Template-Free Electrochemical Route. J. Mater. Chem. 2011, 21, 432–438.

(19) Zhou, L. Q.; Ling, C.; Jones, M.; Jia, H. Selective CO2 Reduction on a Polycrystalline Ag Electrode Enhanced by Anodization Treatment. Chem. Commun. 2015, 51, 17704–17707.

(20) Hoshi, N.; Kato, M.; Hori, Y. Electrochemical Reduction of CO2 on Single Crystal Electrodes of Silver. J. Electroanal. Chem. 1997, 440, 283–286.

(21) Jeon, H. S.; Sinev, I.; Scholten, F.; Divins, N. J.; Zegkinoglou, I.; Pielsticker, L.; Roldan Cuenya, B. Operando Evolution of the Structure and Oxidation State of

Size-Controlled Zn Nanoparticles during CO 2 Electroreduction. J. Am. Chem. Soc. 2018, 140, 9383–9386.

(22) Tröger, L.; Arvanitis, D.; Baberschke, K.; Michaelis, H.; Grimm, U.; Zschech, E. Full Correction of the Self-Absorption in Soft-Fluorescence Extended X-Ray-Absorption Fine Structure. Phys. Rev. B 1992, 46, 3283–3289.

(23) Maurizio, C.; Rovezzi, M.; Bardelli, F.; Pais, H. G.; D'Acapito, F. Setup for Optimized Grazing Incidence X-Ray Absorption Experiments on Thin Films on Substrates. Rev. Sci. Instrum. 2009, 80, 63904.

(24) Allen, J. P.; Scanlon, D. O.; Watson, G. W. Electronic Structures of Silver Oxides. Phys. Rev. B 2011, 84, 115141.

(25) Balerna, A.; Liotta, L.; Longo, A.; Martorana, A.; Meneghini, C.; Mobilio, S.; Pipitone, G. Structural Characterization of Pumice-Supported Silver-Palladium Metal Clusters by Means of XAFS and AWAXS. Eur. Phys. J. D 1999, 7, 89–97.

(26) Peng, X.; Karakalos, S. G.; Mustain, W. E. Preferentially Oriented Ag Nanocrystals with Extremely High Activity and Faradaic Efficiency for CO 2 Electrochemical Reduction to CO. ACS Appl. Mater. Interfaces 2018, 10, 1734–1742.

(27) Hsieh, Y.-C.; Senanayake, S. D.; Zhang, Y.; Xu, W.; Polyansky, D. E. Effect of Chloride Anions on the Synthesis and Enhanced Catalytic Activity of Silver Nanocoral Electrodes for CO 2 Electroreduction. ACS Catal. 2015, 5, 5349–5356.

(28) Kim, C.; Eom, T.; Jee, M. S.; Jung, H.; Kim, H.; Min, B. K.; Hwang, Y. J. Insight into Electrochemical CO 2 Reduction on Surface-Molecule-Mediated Ag Nanoparticles. ACS Catal. 2016, 779–785.

(29) Zhou, Y.; Che, F.; Liu, M.; Zou, C.; Liang, Z.; Yuan, H.; Li, J.; Wang, Z.; Luna, P. De; Yuan, H.; et al. Dopant-Induced Electron Localization Drives CO2 Reduction to C2 Hydrocarbons. Nat. Chem. 2018, 1–20.

(30) Hori, Y.; Wakebe, H.; Tsukamoto, T.; Koga, O. Electrocatalytic Process of CO Selectivity in Electrochemical Reduction of CO2 at Metal Electrodes in Aqueous Media. Electrochim. Acta 1994, 39, 1833–1839.

(31) Xu, Y.; Greeley, J.; Mavrikakis, M. Effect of Subsurface Oxygen on the Reactivity of the Ag(111) Surface. J. Am. Chem. Soc. 2005, 127, 12823–12827.

(32) Serafin, J. G.; Liu, A. C.; Seyedmonir, S. R. Surface Science and the Silver-Catalyzed Epoxidation of Ethylene: An Industrial Perspective. J. Mol. Catal. A Chem. 1998, 131, 157–168.

(33) Kim, D.; Resasco, J.; Yu, Y.; Asiri, A. M.; Yang, P. Synergistic Geometric and Electronic Effects for Electrochemical Reduction of Carbon Dioxide Using Gold-Copper Bimetallic Nanoparticles. Nat. Commun. 2014, 5, 5948.

Appendix B

Experimental section

Sample fabrication. Ag foils (Mateck, 99.9%, 0.25 mm) and Ti foils (Alfa Aesar, 99.5%, annealed, 0.25 mm) sputtered with 600 nm of silver were treated with potential pulses in a homemade Teflon 2-compartment cell, separated by a Nafion membrane. Both compartments were filled with 0.2 M NaOH (99.9% purity, Boom chemicals). A Pt thin film was used as counter electrode, a glass Redrod electrode (1 M KNO_3, XR440, Radiometer Analytical) was used as reference electrode. The sample fabrication was performed by cycling between 0 and 1.2 V vs. Ag/AgCl at 50 Hz for 5 hours.

Material characterisation. SEM images were collected on a JEOL JSM-6010LA SEM microscope with a tungsten hairpin filament. Images were collected at an accelerating voltage of 10 kV and a working distance of 10 mm. GIXRD patterns (20°−116.5° 2θ) were collected using a Bruker D8 Discover X-ray diffractometer in Grazing incidence mode with a copper source (λ = 1.5418 Å), Göbel mirror and 0.2° Soller slit. XRD patterns (25°−100° 2θ) were collected using a Bruker D8 Advance X-ray diffractometer in Bragg−Brentano configuration with a cobalt source (λ = 1.7889 Å). XPS experiments were conducted using a Thermo Scientific K-alpha apparatus equipped with an Al K-alpha X-ray Source and a Flood Gun to avoid charging of the sample. Parameters used for the measurements were: spot size of 400 μm, pass energy of 50 eV, energy step size of 0.1 eV, dwell time of 50 ms, 10 scans in the vicinity of the Ag 3d and O 1s orbital binding energy.

Electrochemical characterisation. Gaseous products from CO_2 reduction were measured on an online Compact GC (Compact GC 4.0 from Global Analytical Solutions with H2/O2/C1-C5 analyser). The GC took an aliquot every three minutes. CO_2 reduction was performed for one hour at a fixed potential of -0.8 V vs. RHE. The reported faradaic efficiencies are averaged values of at least two samples. The reaction was performed in a homemade PMMA 2-compartment cell. Both compartments were filled with CO_2-saturated 0.1 M $KHCO_3$ (99.995% K_2CO_3 from Sigma Aldrich). A Pt thin film was used as counter electrode, a glass Ag/AgCl electrode (saturated KCl, XR300, Radiometer Analytical) was used as reference electrode. A Nafion membrane separated the two compartments, 11.5 ml/min of CO_2 was continuously bubbled through both compartments. The solvent resistance (R_u) was between 30 and 35 Ω in the experiments.

Electrochemical surface areas were measured through the double layer capacitance method. CVs were taken over a non-Faradaic region (0.51 to 0.61 V vs RHE) in nitrogen saturated 0.1 M $NaClO_4$ at different scan rates (10, 30, 50, 60, 70, 90 and 100 mV/sec). The non-Faradaic region was determined by taking the open circuit value of reduced Ag as the value around which the CV scan was performed. The slope of the total

geometric current versus the scan rate gave the capacitance which was used to determine the relative roughness by normalizing the capacitance of the Ag foil.

DFT calculations. A 2x3x6 slab size was used for Ag(110). The Ag metal slab and surfaces with and without adsorbed intermediates were created using the Atomic Simulation Environment (ASE).[1] All density functional theory (DFT) calculations were carried out with the projector augmented wave (PAW) method as implemented in the GPAW software.[2,3] BEEF-vdW exchange correlation (xc) functional was used to perform all the energy calculations[4,5] with plane-wave (PW) cut-off energy value of 450 eV. Lattice constants for the bulk FCC metal were calculated using the same xc functional and PW cut-off for a residual force on all atoms of less than 0.005 eV $Å^{-1}$. The resulting lattice constant for Ag, 4.1384 Å, was used for all other energy calculations.

For the geometry optimisation, the top two metal layers as well as the adsorbed atoms were allowed to relax until a residual force of less than 0.01 eV $Å^{-1}$ is reached. The self-consistent field (SCF) convergence criterion was set to 5 x 10^{-4} eV for adsorption energy calculations. A 12 Å vacuum layer was placed above the periodically repeating slabs. The Fermi-Dirac method was used to smear the Fermi level with an electronic temperature of 0.1 eV and a Pulay mixing of the resulting electronic density was applied. A (3x3x1) k-point sampling was used and a grid spacing between 0.16 Å and 0.2 Å was used for all calculations.

XAS characterisation. X-ray absorption spectra were recorded at the Dutch-Belgian beamline (DUBBLE, 26A) of the European Synchrotron Radiation Facility (ESRF) in Grenoble, France. Silver K-edge (25515.59 eV) spectra were recorded between 25300 and 26055 eV. The energy of the X-ray beam was tuned by a double-crystal monochromator operating in fixed-exit mode using a Si(111) crystal pair. XANES and EXAFS spectra of the samples were collected in fluorescence mode using a 9-element Ge detector (Ortec Inc.), whereas reference spectra of the metallic Ag foil and the silver oxides were collected in transmission mode using Ar/He-filled ionisation chambers at ambient temperature and pressure. The photon flux of incoming X-rays is ~2.5 * 10^{10} photons/cm^2. Ex situ samples were measured at grazing incidence angles of 0°, 0.1°, 5° and 10° degrees. In operando samples were measured at 6° degrees. EXAFS data analysis was performed on data that was averaged from at least 3 20 minute scans.

For the operando measurements a home-made electrochemical flow cell (Figure B5) was used. The electrolyte was pulled through the cell volume using a peristaltic pump operated at 40 rpm. The cell had a silver catalyst as WE, a coiled Pt wire as counter electrode and a 2 mm diameter PEEK Leakless Ag/AgCl RE (ET072, EDAQ). The electrolyte was CO_2 saturated 0.1 M $KHCO_3$. The headspace of the electrolyte reservoir was purged with CO_2 during measurements to ensure constant CO_2 saturation and avoid bubbles in the incoming electrolyte. A Biologic SP240 potentiostat was used to

control the potential in a three-electrode configuration. The Ag and ODAg samples were all used for 1 hour of CO_2 reduction coupled to the GC prior to their measurements in the XAS cell. This way, the ODAg state was already reached before the sample was measured using XAS.

EXAFS data analysis. Because of the cell design, measurements could not be performed in transmission geometry. Instead, the EXAFS spectra were acquired in fluorescence mode under different angles of incidence. Spectra of non-dilute samples that were measured in fluorescence mode need to be corrected with a self-absorption correction, for instance using the Athena software. We used a transmission EXAFS spectrum of a 5 μm thick pure silver foil to derive the typical coordination number obtained for similar samples. By comparing our self-absorption corrected fluorescence spectra with the transmission spectrum of pure silver we were able to get good estimations for the size of the required corrections. In short, the operando spectra needed a correction of a 0° in and 90° out configuration (Athena software, Fluorescence self-absorption correction option) due to the combination of a thick substrate, low angle of incidence and shielding by the cell. The ex situ samples were not shielded by a cell and therefore only required a mild 45° correction. The sputtered samples could be analysed without any correction since the thin 600 nm sputtered layer falls within the limit of thin samples that do not require a self-absorption correction.

After the correction, the EXAFS data is fitted using Viper software. Since the measurements are performed at room temperature, the higher shells are relatively noisy. We therefore only fit the spectra up to ~ 3 to 4 Å from the absorber atom. For a silver metal, this corresponds to only the first shell, for the silver oxides, the first (Ag-O) and the second (Ag-Ag) shell can be fitted. The k-range is taken from 2.5 to 10 $Å^{-1}$, all Fourier transforms are k^2-weighted. In some cases the error in fitting the coordination number could not be properly estimated by the software. In these cases instead the difference between the normalised and the normalised + smoothed data was taken as the error.

Ag-O model clusters. An fcc cuboctahedral cluster was modelled to calculate a core-shell structure with a metal silver core and a silver oxide shell.[6] the metal cluster was varied in size by adding additional A-Ag shells. The calculations were performed on 2, 3 and 4 Ag-Ag shell cluster, all surrounded by one Ag-O shell. The coordination number of Ag-O for each Ag atom in the cluster was calculated and average over the entire cluster to yield the final Ag-O coordination numbers.

Applied potential during operando EXAFS measurements. A typical CO_2 reduction reaction at an ODAg catalyst is performed at -0.8 V vs. RHE. Hydrogen and CO are formed at this potential at a total current density of around 2 mA/cm^2. When we performed CO_2R at these potentials we generated bubbles that would stick to the catalyst surface. These bubbles strongly interfere with the EXAFS spectra: one spectrum

takes roughly 20 minutes to record, if the amount of bubbles grows in this period of time (which will happen inevitably), the background signal of the EXAFS spectra will shift. This renders the spectrum useless for FT transformation or further data fitting. Therefore we could only generate proper EXAFS spectra by measuring operando at a very low overpotential. We measured at 0 and at -0.12 V vs. RHE. For comparison, an EXAFS spectrum obtained at -0.4 V vs. RHE is shown in Figure B1. When we normalise this spectrum and compare it to the Ag and ODAg used for fitting in the paper, we see how the main feature (the bump at 2 Å) remains the same between the two ODAg measured at different potentials. The signal at 1 Å that is only seen in the -0.4 V vs RHE spectrum most likely stems from noise since even strongly bound O in AgO displays the O-Ag bond at higher values of ~1.5 Å (Figure 3.3a).

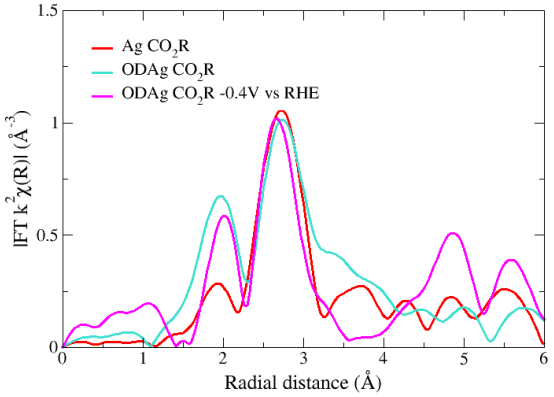

Figure B1. EXAFS spectra as shown in Figure 3.4b together with an ODAg catalyst measured at a higher overpotential to show the minor difference between measuring at 0 and at -0.4 V vs RHE for the fitted region (1.5 – 3.2 Å).

Chronoamperometry and Faradaic efficiency over time

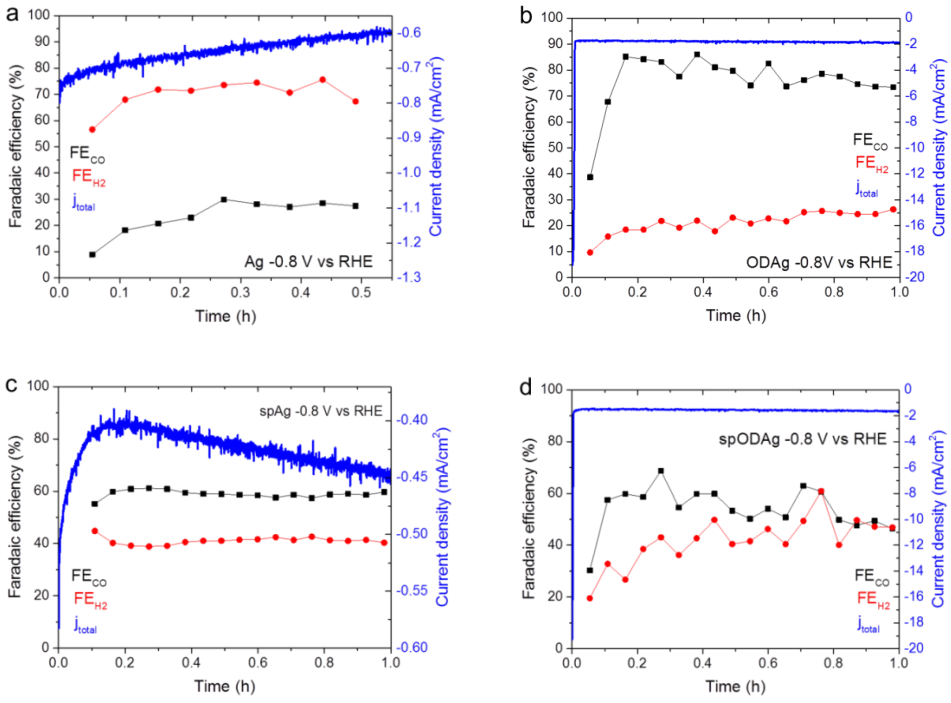

Figure B2. Current density and faradaic efficiency of carbon monoxide and hydrogen recorded for one hour at -0.8V vs RHE for (a) silver, (b) oxide-derived silver, (c) sputtered silver and (d) oxide-derived silver from a sputtered silver substrate.

XRD patterns

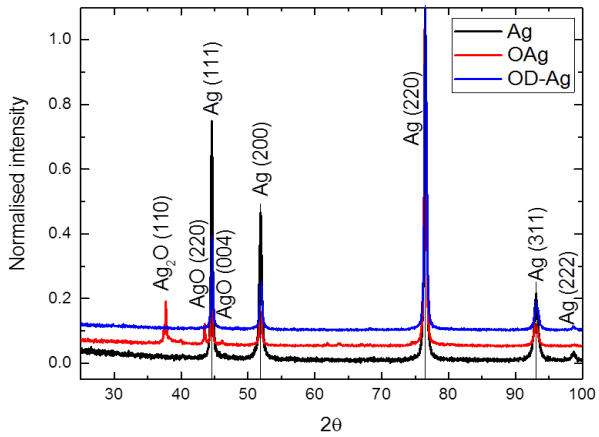

Figure B3. XRD patterns measured in Bragg-Brentano configuration of Ag, AgO_x and ODAg, showing the Ag_2O and AgO XRD reflections in the AgO_x sample. NB the XRD instrument was equipped with a cobalt source, resulting in a different 2θ pattern compared to the GIXRD patterns.

EXAFS cell design

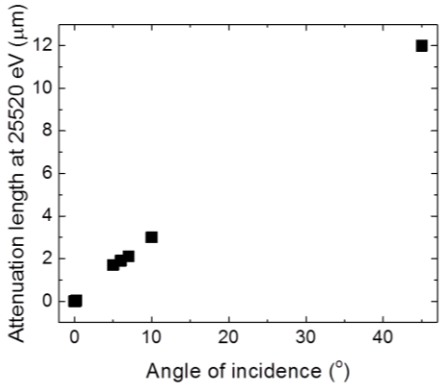

Angle of incidence (°)	Attenuation length
0	1.8 nm
0.1	3.2 nm
0.2	43 nm
5	1.7 μm
6	1.9 μm
7	2.1 μm
10	3 μm
45	12 μm

Figure B8. The attenuation length at the silver K-edge as a function of the X-ray beam incidence angle. The attenuation length is the depth into the probed material (normal to the surface) where the intensity has dropped to 1/e of its value at the surface (calculated without water layer). The adjacent table contains the values used in the graph.

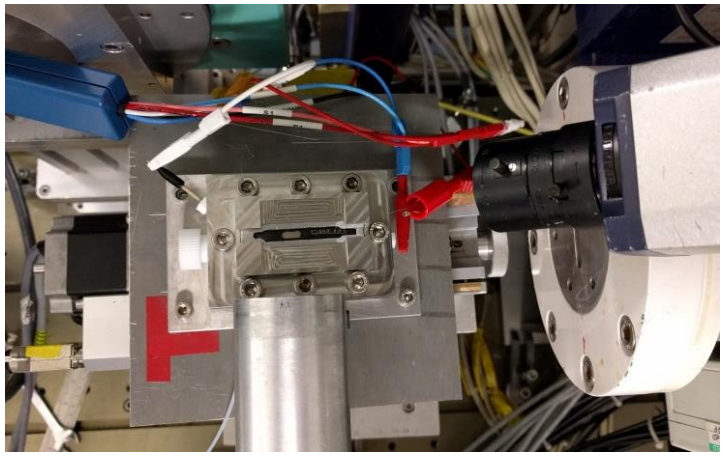

Figure B9. Top view picture of the experimental set-up used for in operando EXAFS data collection. X-ray source is on the left, fluorescence detector on the bottom of the picture.

$k^2\chi(k)$ and first derivative of μ(E)

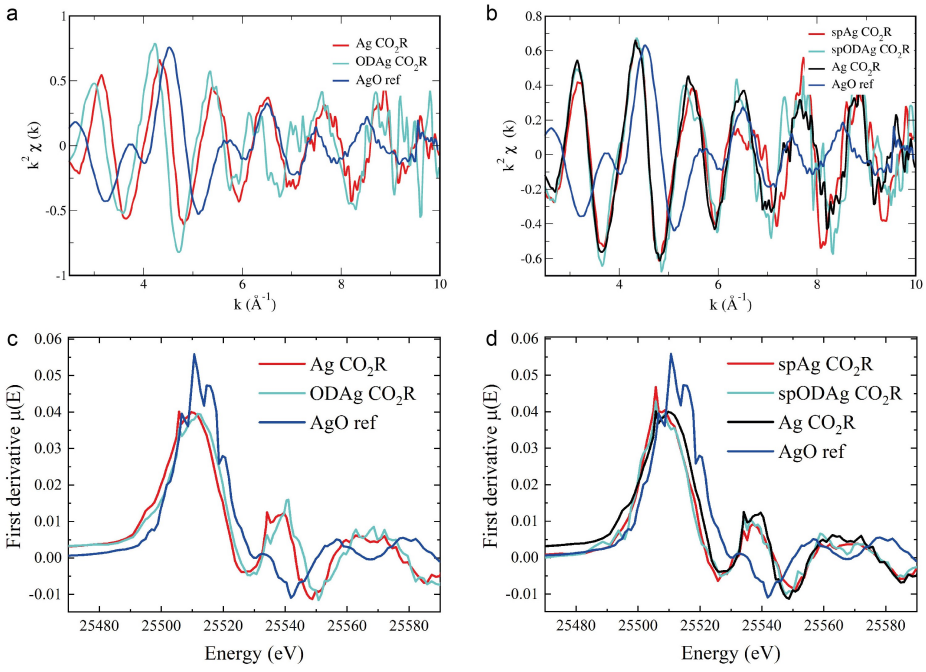

Figure B6. The $k^2\chi(k)$ spectra and first derivative of μ(E) of the data presented in Figure 3.4b and 3.4c. (a) and (c) silver and oxide-derived silver measured in operando are shown together with silver oxide reference to show the distinct difference in $k^2\chi(k)$ between Ag and ODAg in the lower frequency part of the spectrum. (b) and (d) sputtered silver and oxide-derived silver from a sputtered silver substrate are shown with reference to silver and silver oxide. The difference between the sputtered silver samples and pure silver is less strong.

Ex situ characterisation of sputtered samples

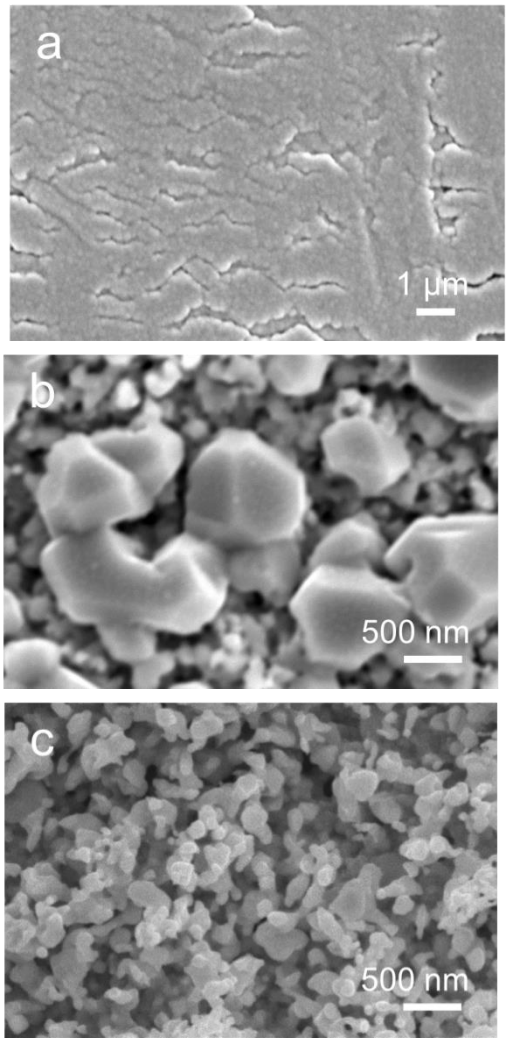

Figure B7. SEM images of sputtered samples: (a) untreated Ag on Ti foil substrate, (b) $spAgO_x$ and (c) spODAg.

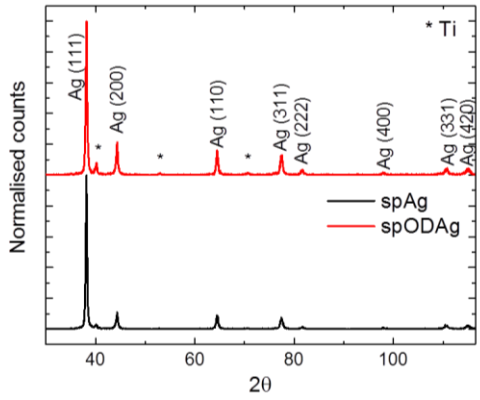

Figure B8. GIXRD patterns of sputtered Ag and oxide-derived silver from a sputtered silver substrate. Titanium reflections denoted by *.

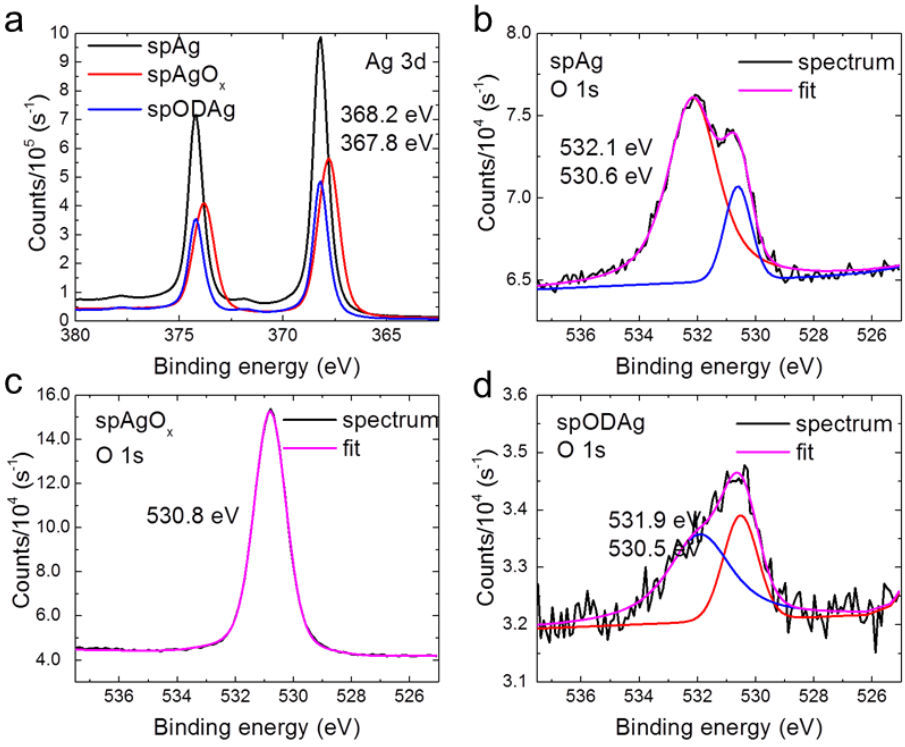

Figure B9. (a) Ag 3d XPS spectra of spAg, spAgO$_x$ and spODAg. The spAgO$_x$ precursor is not metallic but an oxide, as can be concluded from the shift in the Ag 3d peak. O 1s spectrum and fit of (b) spAg, (c) spAgO$_x$ and (d) spODAg, the red and blue lines indicate the deconvoluted peaks.

References

1. Bahn, S. R. & Jacobsen, K. W. An object-oriented scripting interface to a legacy electronic structure code. Comput. Sci. Eng. 4, 56–66 (2002).

2. Enkovaara, J. et al. Electronic structure calculations with GPAW: A real-space implementation of the projector augmented-wave method. J. Phys. Condens. Matter 22, 253202 (2010).

3. Mortensen, J. J., Hansen, L. B. & Jacobsen, K. W. Real-space grid implementation of the projector augmented wave method. Phys. Rev. B 71, 35109 (2005).

4. Wellendorff, J. et al. Density functionals for surface science: Exchange-correlation model development with Bayesian error estimation. Phys. Rev. B 85, 235149(23) (2012).

5. Wellendorff, J. et al. A benchmark database for adsorption bond energies to transition metal surfaces and comparison to selected DFT functionals. Surf. Sci. 640, 36–44 (2015).

6. Longo, A. & Martorana, A. Distorted f.c.c. arrangement of gold nanoclusters: A model of spherical particles with microstrains and stacking faults. J. Appl. Crystallogr. 41, 446–455 (2008).

4

Copper and silver gas diffusion electrodes performing CO_2 reduction studied through operando X-ray absorption spectroscopy

This chapter is based on the following publication:

N.J. Firet, T. Burdyny, N.T. Nesbitt, S. Chandrashekar, A. Longo, W.A. Smith. Copper and silver gas diffusion electrodes performing CO_2 reduction studied through operando X-ray absorption spectroscopy. Catal. Sci. 2019, submitted

X-ray absorption spectroscopy (XAS) offers the unique possibility to study metal electrocatalysts such as silver and copper while they are performing electrochemical carbon dioxide (CO_2) reduction. In this work, we present an approach to perform operando XAS experiments on an electrochemical cell performing CO_2 reduction with a gas diffusion electrode (GDE) as cathode. The experimental set-up, advantages and drawbacks, XAS data analysis, and XAS theory are discussed. Results on copper and silver GDEs obtained through the presented procedures are then presented and discussed. Structural and compositional catalyst data acquired under operando conditions can help further density functional theory calculations, catalytic, and systems studies on CO_2 reduction.

Structural and compositional data including crystallite size was obtained while performing high current density (up to 200 mA/cm^2) CO_2 reduction. On the silver catalysts at higher than 100 mA/cm^2 applied current density, a Ag-X contribution was found and is ascribed to Ag-O. For both silver and copper, the XAS experiments revealed that the crystallite size of the ex situ samples is smaller than the samples during CO_2 reduction. Furthermore, metal particle size polydispersity was found in the silver catalysts by comparing the obtained coordination numbers with theoretical values. The operando EXAFS data was of such high quality (k: 3 - 14 $Å^{-1}$) that four shells could be fitted. The value of combining ex situ material characterisation and electrocatalyst performance data with operando XAS experiments is discussed and found of great importance to further CO_2 reduction research.

4.1 Introduction

Electrochemical CO_2 reduction has the potential to contribute to the storage and use of renewably generated electricity. CO_2 electroreduction can utilise renewable electricity to convert abundant feedstocks into valuable chemicals or fuels and be used as a means to store excess electricity in high energy density chemical bonds which can be used when needed.

A recent progression in the renewable conversion of water and CO_2 has seen the electrochemical reduction of CO_2 move toward more industrially relevant operating conditions, enabled largely by a change in the electrochemical cell configuration. Gas diffusion electrode (GDE) and, to a lesser extent to date, membrane electrode assembly (MEA) configurations have become the cell design of choice over the traditional H-cell system that has dominated literature for most of the last decade.[1,2,3] The performance gains in GDE and MEA architectures have mainly occurred by maintaining high concentrations of CO_2 in the gas phase in close proximity to an immersed catalyst layer. This improved CO_2 access largely eliminates mass transfer limitations that heavily hinder CO_2 reduction in an H-cell architecture, while allowing for higher catalyst surface areas with access to CO_2. The increased concentration of CO_2 accessible to the catalyst surface has resulted in an increase in current density from 1-20 mA/cm^2 to 200-900 mA/cm^2 depending on the product while requiring lower overpotentials and delivering higher CO_2 reduction selectivities when switching from an H-cell configuration to the GDE architecture.[4–6]

As the performance of CO_2 reduction continues to develop closer toward practical industrial applications, it has become more important to assess catalyst properties and functionalities under real and practical operational conditions. This means that the catalyst should be studied while it is being subjected to practical conditions in terms of electrolyte, potential, reaction rate, local reaction environment, substrate and catalyst deposition techniques. Only then is it possible to determine whether the observed catalytic structure and composition are representative of the active catalyst. The resulting analysis can add value to computational studies evaluating the reaction energetics of different catalyst structures and configurations, and to experimental studies designing new catalysts.

Ex situ characterisation of catalysts before and after CO_2 reduction and monitoring of the product output is inadequate to identify catalytic active sites and structures. The structure of a catalyst can have its electronic and structural properties altered by transferring the electrode from an ambient pressure aqueous environment with an applied potential, to a vacuum chamber where most ex situ characterisation occurs.[7] Therefore, it is necessary to study a catalyst under operational conditions to be able to derive strong structure-functionality relationships to determine active site coordination

and relative acidity under realistic conditions. Fortunately, there are several spectroscopic techniques available to perform operando studies on CO_2 reduction systems. For example, in situ transmission electron microscopy (TEM) and in situ X-ray photoelectron spectroscopy (XPS) are able to study the catalyst size and oxidation state, respectively, albeit under low vacuum conditions.[8,9] In the case of TEM, the small reactor chamber required to obtain data poses many issues for electrode design and catalysis, meaning that the range of reaction conditions is generally limited. For ambient pressure studies, attenuated total reflection infrared (ATR-IR) spectroscopy and Raman spectroscopy are useful to study reactive species on the surface or near the catalyst surface during electrocatalysis.[10,11,12] In the case of infrared and Raman spectroscopy, cell design considerations have to be taken into account to make sure the reaction can be observed during electrolysis, posing stringent demands on the experimental data that can be obtained. Finally, X-ray absorption spectroscopy (XAS) has been used to study the physical, compositional and morphological properties of catalysts while performing electrochemical CO_2 reduction at low potentials and reaction rates (< 5 mA/cm^2).[13,14,15,16,17]

X-ray absorption spectroscopy (XAS) is a material characterisation technique that is powerful enough to measure CO_2 reduction catalyst properties under operando conditions, in part enabled by high energy X-rays (E > 7 keV) capable of penetrating different materials and fluids. In recent years, several operando XAS studies on CO_2 reduction catalysts in H-cell type systems were investigated, leading to a large number of unique cell designs necessary to obtain meaningful data. Interestingly, studies using frontal irradiation of the catalyst were often limited to low current densities and applied potentials since gaseous products evolving from the catalyst surface in the liquid electrolyte strongly distort the measured spectra, due to the different X-ray absorption cross-sections of the electrolyte and gas phase products.[15,18] A number of researchers have subsequently used different architectures based on X-ray irradiation through the back of the sample, which alleviated the issue of reaction rate and gas formation from disrupting the signal.[14,16,17] Since many CO_2 reduction catalysts designed for H-cells have a relatively thick and opaque substrate which blocks the incoming X-rays from reaching the surface, not all catalysts are suitable for the back irradiation geometry. Similarly, in many studies a large fraction of the signal is likely to come from the bulk material, rather than the active surface in contact with the electrolyte, resulting in a dampening of the surface features of interest. Thus, despite its powerful capabilities to probe catalysts under operando CO_2 reduction conditions, an XAS cell design and technique that is capable of operating over a wide range of practical reduction conditions and catalysts has yet to be demonstrated and discussed in detail for CO_2 reduction.

Typical gas diffusion electrodes are made of porous carbon-based substrates with a carbon nanoparticle surface (also called a microporous layer) that offers surface area on

the nanoscale and roughness on the microscale.[19,20] A catalyst deposited on top of the carbon support then forms a porous electrode layer with a higher electrochemically active surface area to volume ratio than planar electrodes, which suffer from CO_2 diffusion limitations.[21] As long as the catalytic layer is not more than a few hundred nanometres thick, X-rays can then easily penetrate not only the carbon support, but the entire catalyst layer. Recent electrochemical CO reduction work has demonstrated that this approach can yield high quality operando XAS spectra on copper catalysts under different potentials and reaction environments.[20,22] These reports show the power of operando studies to give insights into the catalyst's compositional, structural, and electronic properties under operational conditions that cannot be observed with ex situ characterisation techniques alone. A comprehensive analysis and guide to perform operando XAS studies for CO_2 reduction catalysts under representative reaction conditions can therefore be helpful to researchers in the field by introducing a relatively new tool to understand and evaluate CO_2 reduction catalysts.

Here, we provide a general guide to show the capabilities and shortcomings of operando XAS and how it can be used to evaluate catalyst properties under high current density electrochemical reactions in a GDE cell. First, we describe the experimental technique and setup in detail that was used for operando XAS analysis of CO_2 reduction on gas diffusion electrodes, and compare the signal quality and capabilities for a variety of reaction conditions. We then showcase the technique for an operando XAS study of a copper catalyst deposited on a GDE, varying the catalyst thickness, reaction rate, electrolyte and overpotential, highlighting the experimental robustness of the approach. Finally, we provide a similar analysis for a silver catalyst deposited on a GDE.

4.2 Results – Guide to operando XAS on a GDE

X-ray absorption spectroscopy measures the X-ray absorption coefficient μ(E) as a function of energy. It is a chemically selective, element-specific technique. X-rays with an energy equal to or greater than that of the specific absorber atom excite the core electron which then goes to the continuum as a photoelectron. The photoelectron wave is then scattered by the surrounding atoms. The absorption coefficient of the X-rays is determined by the local environment of the absorber atom and is therefore always unique, providing physical and compositional information of the local environment of a specific chemical element in terms of distances, Debye-Waller factors and coordination numbers. Since the energy of these electrons is so high (the 1s electron of silver needs to be excited by a 25515 eV X-ray) it makes the X-rays capable of traveling through materials of lower elemental mass without losing much of their intensity: the technique can therefore be used under operating conditions (*operando*) because it will be able to penetrate the electrolyte, catalyst support, and cell window.

Hard X-rays (E > 7 keV) are needed to probe the most active metal catalysts for electrochemical CO_2 reduction (gold, silver, copper, tin), and offer a unique possibility for operando studies. The higher energies needed to excite the electrons of these metals are not absorbed by light materials such as carbon or oxygen (since their core electron energies are so much lower), offering the possibility to create operational cells that encase the metal of interest. The penetration depth of X-rays depends on the energy of the incident beam and the materials (electrolyte, cell window, catalyst support) that have to be crossed before being absorbed by the material of interest. Synchrotrons in particular offer a high flux of high energy X-rays compared to conventional X-ray characterisation techniques, improving the signal-to-noise ratio even more. A clear signal then allows for X-ray Absorption Near Edge Structure (XANES) and Extended X-Ray Absorption Fine Structure (EXAFS) data to be extracted, which can then be processed and analysed to provide information about the probed material. More information on typical EXAFS data analysis can be found in Appendix C.

Valuable information can be obtained from XANES data, including the oxidation state of the catalyst during the reaction. Fitting of the EXAFS data can reveal the coordination number (concentration of chemical bonds), crystallite size, disorder, atom-to-atom distance and the type of atoms in the immediate vicinity of the probed element. This information can be obtained under different reaction conditions, allowing for changes in the structure of the catalyst to be measured and compared as a function of operating conditions. Furthermore, the stability of the catalyst material can be monitored during a reaction by comparing consecutive spectra, which for CO_2 reduction can be useful to determine if changes in observed product selectivities over time are a result of the catalyst itself changing. In order to collect and use this data for analysis alongside typical electrochemical performance metrics (selectivity, potential, current density, stability), an electrochemical cell is required which allows for the input and output of X-ray signals, while functioning as close as possible to correlating electrochemical experiments.

Cell design. While GDE and MEA based electrochemical cells for CO_2 reduction have gained attention for their demonstrated performance benefits, these architectures also provide an optimal configuration for operando XAS studies. For example, commonly used GDEs are made of carbon-based materials that only require a thin (~100 nm) layer of catalyst to show highly selective, stable and efficient CO_2 reduction performance.[6] Meanwhile, the GDE substrate is ~300 µm thick and made of carbon, allowing X-rays to pass through easily. This allows for a back-irradiation geometry without compromising the catalyst design, as shown in Figure 4.1a.[23] A simple GDE cell design used in many recently published GDE-based CO_2 reduction performance papers can then be easily modified to accommodate XAS measurements.[24,25] The chamber used to continuously flush CO_2 over the back of the GDE needs to be opened to allow the X-rays to enter and the produced fluorescent signal to leave the cell (Figure 4.1a). The cell opening can be

covered by a thin X-ray transparent window such as polyimide (Kapton) tape to allow X-rays to reach the GDE while confining CO_2 within the reaction chamber. The opening should have wide angles to facilitate a 45° geometry between incoming X-rays and outgoing fluorescence, ensuring that a large signal reaches the detector.

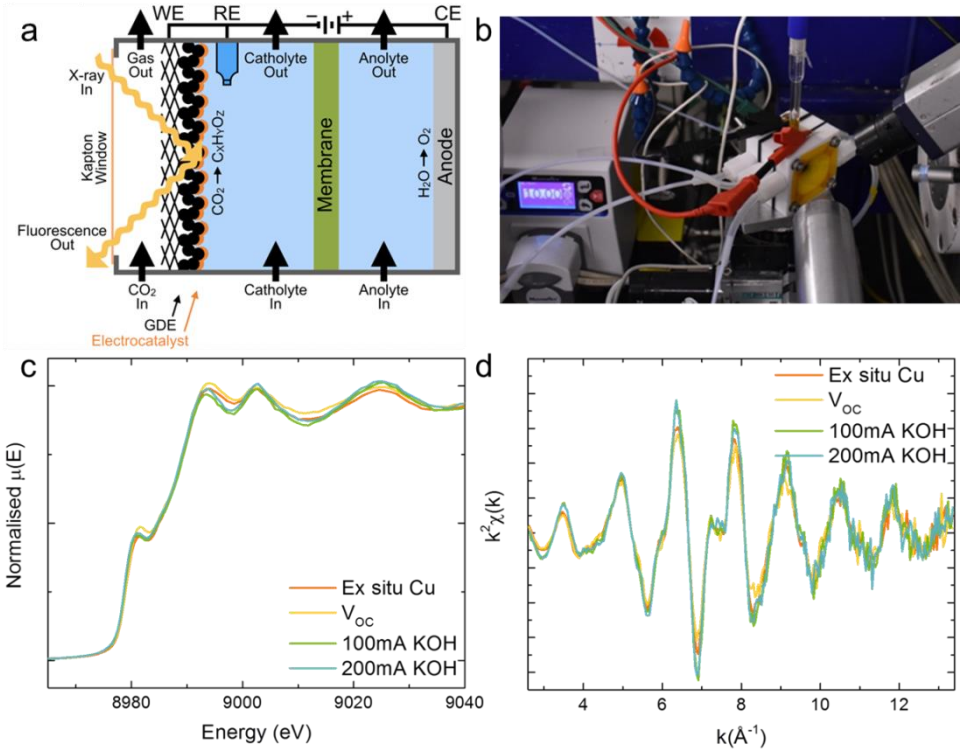

Figure 4.1. (a) Schematic and (b) picture of the cell used for operando XAS experiments described here. (c) Normalised absorption coefficient (μ(E)) and (d) EXAFS ($k^2\chi(k)$) data of a 100 nm thick Cu catalyst on a gas diffusion layer in various operating conditions: ex situ (orange), at open circuit potential in 1 M KOH (yellow), under 100 mA/cm² (green) and 200 mA/cm² (turquoise) in 1 M KOH. Note that the 100mA and 200mA labels in the figures correspond to 100 and 200 mA/cm² current density.

The other components of the cell can be left exactly as they would be in a normal electrochemical performance study including a membrane, counter electrode, reference electrode and flowing anolyte and catholyte. Some of these components are typically absent in most XAS studies to minimise complexity and maximise signal, but their absence could also influence the activity and selectivity of the reactions taking place. The cell is also equipped with a peristaltic pump to ensure constant liquid flow throughout the cathode and anode chambers. Care should be taken to dampen or control the flow, however, as pulsations of the fluid flow can disrupt the gas-liquid interface formed by the gas diffusion electrode. A dual piston pump (a pump used for

high performance liquid chromatography (HPLC)) can be used to reduce the peristaltic pressure on the GDE.

An operational issue that can arise during electrochemical testing of a GDE is flooding, or perspiration, of the liquid electrolyte crossing through the gas diffusion layer into the gaseous CO_2 chamber. This can occur during electrochemical operation when the pressure in the catholyte compartment is higher than in the gas compartment. Flooding can also occur when the hydrophobicity of the GDE is affected by prolonged exposure to a high applied potential: this should be ruled out before the XAS experiments. Flooding will cause electrolyte droplets to appear on the gas side of the GDE, and possibly distort the XAS signal. To minimise this effect during XAS measurements, the pressure in the liquid (catholyte) compartment and the CO_2 gas compartment should be controlled carefully. When a Kapton window is used, the pressure in the gas compartment could be lower than in other operational conditions, and therefore care must be taken to keep the experimental conditions of the XAS-modified cell as close as possible to the cell used for performance characterisation in order to draw strong structure-functionality relationships.

While GDEs are often treated with very simple catalyst deposition techniques such as drop-casting, air spraying, evaporation, sputtering or electrodeposition, which allow for a thin catalyst layer to be deposited, more intricate catalyst design methods can be used as well, as long as the catalyst layer remains thinner than ~500 nm. The thickness of the catalyst layer can affect the signal quality in two major ways. First, the incoming X-rays are ultimately absorbed by the material of interest, and if the layer is too thick they will not be able to penetrate through the entirety of the catalyst layer. The received signal could then disproportionately be probing the material closest to the gas channel, rather than the whole layer. Second, fluorescence XAS is based on the assumption that the probed material is either a low concentration species or thin film compared to its environment. When this assumption is not met, the XAS signal will be dampened and a self-absorption correction has to be applied during data analysis.[26] When the catalyst layer is sufficiently thin, XAS is highly suited to study complex catalysts such as alloys or metal-organic catalysts.[17,27] In this regard, MEA cell architectures would then also be very suitable to study using a cell design similar to the one described above. A MEA consists of a catalyst layer deposited directly on, or adjacent to, the membrane, removing any resistance losses from the catholyte.[28] In the following section, the operation of a GDE cell in an operando XAS setup will be discussed.

Setup and operation of a GDE cell for operando XAS measurements. In addition to cell design and catalyst preparation, a number of other issues are important to consider in order to ensure a high signal-to-noise ratio of the desired active materials. For example, the sample alignment and electrochemical operating conditions are important for achieving the best XAS signals and resulting data.

To ensure easy changeover and alignment of sequential samples, and to keep similar signal strength and quality over extended operation, sample alignment for the XAS experiments is extremely important. It is advised to mount the cell on a motorised x-, y- and z-stage that can be used to align the cell with respect to the incident X-ray beam and the fluorescence detector. After an initial alignment, during a more accurate alignment the sample should be scanned at a fixed energy in the absorption window of the element of interest, while moving the cell with sample to find the location that gives the highest detection signal.

For the cell to be controlled operando while taking active synchrotron measurements, the potentiostat should also be operated from the control room rather than the experimental room to ensure that the applied potentials and current densities can be varied in real-time. Here, the cell displayed in Figure 4.1a and 4.1b was used to collect operando XANES and EXAFS spectra during CO_2 reduction on both copper and silver films that were sputtered on a GDE. Figure 4.1c shows normalised absorption coefficient spectra that were recorded under various experimental conditions (ex situ, under open circuit potential (V_{OC}), and at applied current densities of 100 mA/cm^2 and 200 mA/cm^2) on a GDE coated with a Cu catalyst. In Figure 4.1d, the data of Figure 4.1c was converted into the k^2-weighted EXAFS (k$^2\chi$(k)) by converting the x-axis from energy to wavenumber and the absorption coefficient into χ(k) by dividing by the absorption coefficient of a Cu atom in vacuum (details can be found in the experimental section and Appendix C). The EXAFS is measured up to 13.4 Å^{-1} and shows high quality spectra, which can be seen from the high signal-to-noise ratio even at high k (>11 Å^{-1}) and without any smoothing techniques applied to it. The y-axis in Figure 4.1c and 4.1d shows k^2 χ(k), rather than simply χ(k). The k^2 multiplication is performed because the EXAFS oscillations diminish quickly at larger distances from the absorber atom and become harder to interpret.

Characterizing crystallite size. In any XAS study, the post-processing and analysis of the collected data is as important as obtaining a quality signal. The processed data can subsequently be used to provide structural information such as the catalyst crystallite size, which directly relates to the number of undercoordinated metal atoms. These atoms have often been identified as active sites in computational studies.[29] In this study, we demonstrate operando electrochemical CO_2 reduction on two catalysts, copper and silver, which are both metals with a face centred cubic (fcc) crystal structure. In an ideal bulk structure, any atom of a fcc material has 12 nearest neighbouring atoms that are all the same distance (R) away from the absorber atom. When crystallites (the smallest defect-free grains in a material) of a sample are less than 5 nm, the average amount of neighbouring atoms becomes smaller than 12 because some atoms are close to or at the surface of the crystallite where there are fewer neighbours due to the termination of the lattice. This correlation implies that the amount of neighbours in a fcc structure directly

relates to the size of the smallest single crystal grains.[30,31] The number of neighbouring atoms is called the coordination number (N_i, where i is the shell number), which can be derived by fitting EXAFS data. The next nearest neighbour has a distance R_2 and a coordination number N_2. This neighbour is part of the second shell, whereas R_1 and N_1 are part of the first shell.

When depositing catalysts onto a GDE, the sample preparation plays a large role in the nanostructure and crystallite size of particles in the catalyst layer. When sputtering is used as the deposition technique, for example, a broad distribution of crystallite sizes typically exists, varying from a half to tens of nanometres. In XAS studies, the EXAFS data will give the dimension of the smallest crystallites, which may not be representative of the overall distribution of crystallite sizes in the catalyst layer. Microscopy such as high resolution scanning electron microscopy (HR-SEM) or TEM can potentially give a qualitative indication of the range of crystallite sizes in a sample. However, as mentioned above, operando TEM for electrochemical applications is severely limited in its experimental conditions and therefore not suitable for high current density studies. Furthermore, the Scherrer formula used in combination with X-ray diffraction (XRD) data can give an estimate of the size of the larger crystallites since it overestimates the crystallite size by neglecting polydispersity.[32]

Using EXAFS data as an input, equation 4.1 can derive small crystallite sizes from the coordination number (N) and distance (R).[30,31]

$$N_{\text{crystallite}} = \left[1 - \frac{3}{4}\left(\frac{R}{R_c}\right) + \frac{1}{16}\left(\frac{R}{R_c}\right)^3\right] N_{\text{bulk}} \qquad 4.1$$

where $N_{\text{crystallite}}$ is the coordination number of the sample, R is the distance between the absorber atom and the neighbouring atom, R_c is the radius of the crystallite and N_{bulk} is the coordination number of a bulk fcc crystal.

Shortcomings of operando XAS. Despite its unique capabilities to characterise material properties under operando conditions, X-ray absorption spectroscopy is inherently a bulk averaging technique in both location and time. The data acquired is highly localised, and the information obtained is on the angstrom length scale. Variations in the sample properties over space and time can however be difficult to assess. To address these shortcomings, X-ray micro-tomography can be used to image smaller sections of the sample one by one in the x and y direction, and then an overall image of the sample can be constructed.[33] X-ray tomography is still limited to the smallest resolution of the beam, which is in the range of 300 nm/pixel at specialised beam lines. This is considerably larger than the length scale of expected catalyst variation in common electrodes, such as the ones we investigate in this work. Therefore, it is necessary to combine ex situ imaging techniques such as high resolution SEM or TEM with operando

XAS to more accurately observe the sample homogeneity. The averaging of XAS measurements applies to the lateral x and y directions across the surface and to the height in the z direction between the surface and further into the sample. The z direction is of interest regarding the catalyst thickness, as mentioned above, which should be kept sufficiently thin to make sure the surface and not just the bulk of the catalyst layer is probed. Therefore, the cell design described here is not suitable for thick (>500 nm) catalysts, which includes metal mesh catalysts that can be used instead of a GDE.

On specialised beam lines, the acquisition time for a XANES spectrum can be as low as a few seconds.[22] While this acquisition time is incredibly fast, molecular dynamics and possible surface restructuring can be orders of magnitude faster and might not be captured using XAS. Therefore, it is important to keep these dynamic processes in mind when attempting to correlate structure-functionality relationships. Standard acquisition time XAS can, however, provide information regarding steady-state operation on the order of minutes, as is common in electrochemical CO_2 reduction systems.

4.3 Results – operando XAS on copper GDEs

Copper is a versatile and interesting catalyst for electrochemical CO_2 reduction. It is the only transition metal catalyst known to produce higher order carbon-based products in appreciable quantities, including ethylene and ethanol, and has been shown to restructure surface facets under different reductive conditions.[34] In addition, copper produces a wide range of products, where the selectivity varies greatly with applied potential, current density, electrolyte composition, and surface morphology.[35] Furthermore, with the increased use of GDE-based systems, Cu catalysts have been able to achieve extremely high partial current densities for CO_2 reduction (>800 mA/cm^2).[6] In addition to testing the effects of alkaline electrolytes (1 to 10 M KOH), Dinh et al. also observed that changing the thickness of the catalyst layer impacted performance.[6] All of these different operating conditions that are investigated in literature, and the subsequent changes in observed performance as a result, make copper an interesting catalyst to study with operando XAS.

Varying current density and catalyst thickness. In this section, we show how the above-mentioned parameters can easily be incorporated into operando XAS studies to examine operation-induced changes in the structure of the catalyst. We examine copper catalysts (see experimental section for details) under a broader range of conditions including different cell architectures (H-cell vs. GDE), applied current densities (1, 100 and 200 mA/cm^2), electrolyte (1 M $KHCO_3$ and 1 M KOH) and catalyst layer thickness (20 and 100 nm). A fresh Cu GDE was used for each new set of operational conditions. The spectra shown in Figure 4.1 and 4.2 are the results of averaging 3 individual 20 min XAS scans that were taken consecutively on the same sample. More details on data extraction can be found in the experimental section. Figure 4.2 shows the k^2-weighted EXAFS

($k^2\chi(k)$) (Figure 4.2a and 4.2b) and the Fourier transformed EXAFS spectra (Figure 4.2c and 4.2d) of Cu GDE samples subjected to these various reaction conditions.

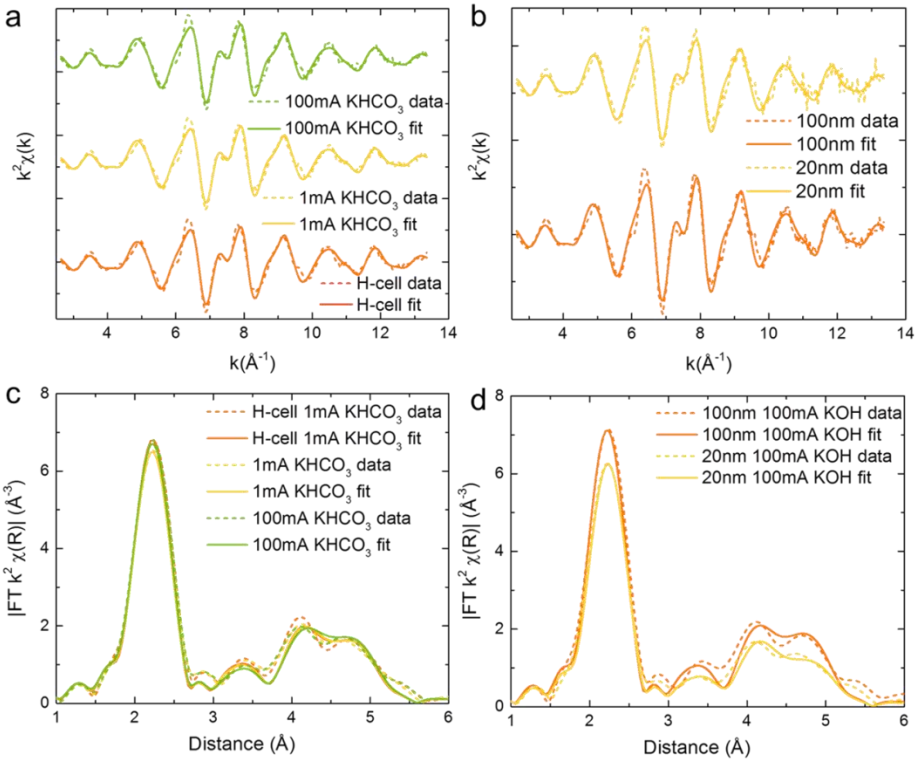

Figure 4.2. k^2-weighted EXAFS data and fits of (a) several copper samples in a 1M $KHCO_3$ electrolyte: a Cu GDE at 1 mA/cm² in an H-cell configuration (orange) and in GDE configuration (yellow). And a sample at 100 mA/cm² (green). (b) Comparison between 100 nm (orange) and 20 nm (yellow) Cu films on GDEs at 100 mA/cm² in 1M KOH. (c) and (d) k^2-weighted Fourier transformed EXAFS data of the spectra shown in (a) and (b) respectively. Note that the 1mA and 100mA labels in the figures correspond to 1 and 100 mA/cm² current density.

Figure 4.2a shows the XAS results from a 100 nm thick Cu catalyst measured under different applied current densities in both the standard GDE-cell configuration (yellow and green lines) and in a modified H-cell (orange lines). To mimic an H-cell configuration, the GDE-cell was transformed by covering the back-side of the GDE with Kapton tape. This allowed X-rays to pass through to the sample, but prevented CO_2 or other gasses from reaching the catalyst through the GDE substrate. Instead, the only CO_2 that could be reduced was supplied from the liquid phase by keeping the electrolyte saturated with CO_2 via bubbling. Figure 4.2a shows that although the reaction conditions and even the cell configuration differ between these samples, the XAS spectra are nearly identical.

Since χ(k) plots are difficult to directly interpret, the spectra were also converted via Fourier transformation (FT), shown in Figure 4.2c. Here, it is possible to see the different Cu-Cu distances present in the sample. The shortest Cu-Cu distance has the highest peak at 2.2 Å. Note that the actual first Cu-Cu distance is 2.534 Å just like the data presented in Table 4.1, but the FT gives a lower number due to the phase-shift (see Chapter 1 for further details). The other peaks arise from the longer Cu-Cu distances. Figure 4.2c also shows that no other atoms than Cu atoms are present in this sample since all distances match only those expected for fcc copper.[36]

Table 4.1. EXAFS fitting results of Figure 4.2b. Fitted R (Cu-Cu distance), N (coordination numbers) and σ^2 (Debye-Waller factor) of first to fourth shell. The EXAFS diameter is calculated using equation 4.1 with N_1 and the Scherrer diameter using the Scherrer formula based on XRD data from the Cu(220) facet at 59.9° 2θ in Figure 4.3a. Note that the 100mA label in the table corresponds to 100 mA/cm² current density. The errors to the last digit are reported in parentheses.

	100nm Cu 100mA KOH	**20nm Cu 100mA KOH**
R_1 (Å)	2.534(5)	2.542(5)
N_1	8.1(7)	7.6(7)
σ^2_1 (Å²)	0.0056(4)	0.006(4)
R_2 (Å)	3.58(3)	3.59(2)
N_2	3.2(5)	2.9(7)
σ^2_2 (Å²)	0.0056(5)	0.0066(4)
N_3	8.6(4)	8.2(6)
σ^2_3 (Å²)	0.010(5)	0.010(5)
N_4	4.2(6)	3.1(6)
σ^2_4 (Å²)	0.011(6)	0.012(7)
EXAFS diameter (Å)	11.6(5)	10.3(5)
Scherrer diameter (Å)	80	0

Another benefit of using XAS is that this technique can examine samples that are very thin. This allows for the effect of different crystallite sizes or interactions with the substrate to be detected. Studying very thin catalysts is especially relevant for industrial applications where the use of (expensive) catalyst materials is preferably kept to a minimum, showing a need for studies evaluating the structural properties of different catalyst thicknesses under electrocatalytic conditions.

Figure 4.2b compares the XAS spectra from a 100 nm Cu film with a 20 nm Cu film during CO_2 reduction at 100 mA/cm² in 1 M KOH. These reaction conditions are representative of other studies performed in this field and were therefore chosen to

study the effect of catalyst thickness under identical reaction conditions.[6,37] The FT in Figure 4.2d reveals a reduction in the height of all individual peaks for the 20 nm sample compared to the 100 nm. Interestingly, the XRD diffractograms of the 100 and 20 nm Cu catalysts on the GDEs (taken ex situ, before CO_2 reduction, Figure 4.3a) show no crystallinity in the 20 nm film as evidenced by the lack of peaks at 50.9° and 59.5° 2θ. The Scherrer formula shows a crystallite size (sometimes referred to as grain size) of 80 Å (8 nm) for the 100 nm sample based on the Cu(200) facet at 59.5° 2θ, and shows a completely amorphous film for the 20 nm sample (Figure 4.3a). However, by fitting the XAS data from Figure 4.2b, it is possible to extract local-range information and the crystallite size can be determined from equation 4.1.[30] As shown in Table 4.1, the crystallite sizes are found to be 10.3 Å and 11.6 Å in diameter for the 20 nm and for the 100 nm sample, respectively.

To understand the discrepancy in crystallite size between the two techniques, the difference between the characterisation methods becomes helpful to discuss. Both the XAS and the XRD data give averaged spatial data, however XAS provides an estimate of the lower crystallite sizes while XRD provides an estimate of the larger crystallite sizes.[32] The XRD diffractogram of the 20 nm sample shows no defined crystallite size or structure, so it appears that even the larger particles of the 20 nm sample are below the detection limit of the XRD apparatus. Since the FT spectrum of the 20 nm sample maintains the fcc shape (same shape as the 100 nm GDE spectrum) the sample seems to not be truly amorphous. The 100 nm Cu electrode has nanoparticles that range from 12 to 80 Å and the 20 nm sample consists of particles ranging from 10 Å to a value below 80 Å.

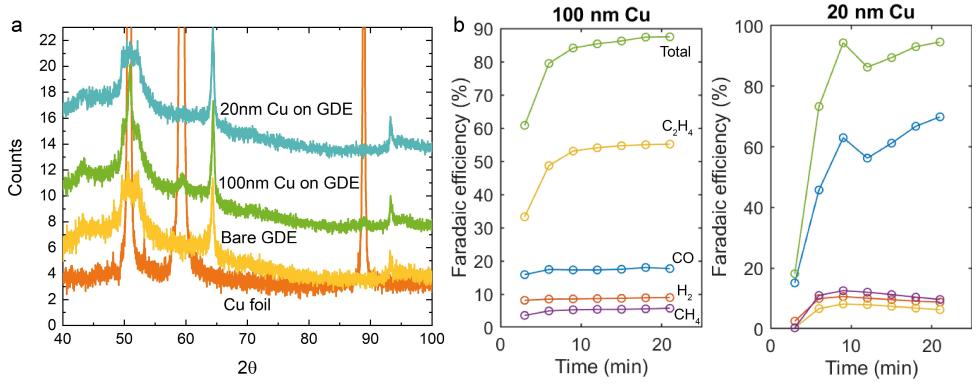

Figure 4.3. (a) XRD diffractograms of a bare GDE, a copper foil, a 100 and a 20 nm Cu film on a GDE substrate. (b) Faradaic efficiency data for a 100 nm and 20 nm thick Cu sample at 100 mA/cm² in 1M KOH.

The Cu-Cu distances (R) and Debye-Waller factors (σ^2) are different for the two thicknesses, with the 20 nm film having larger Cu-Cu distances and a higher Debye-

Waller factor compared to the 100 nm catalyst. The Debye-Waller factor is a measure of disorder in the crystal lattice; when atoms are not perfectly aligned according to the fcc structure, the Debye-Waller factor increases. Since the 20 nm sample is an amorphous film, meaning no long-range ordering was found in the XRD data, it seems likely that under applied potential the catalyst will restructure, causing disorder and altered Cu-Cu distances, as can be seen from the higher σ^2 and R in Table 4.1 for the 20 nm sample. Potential-dependent restructuring of Cu catalysts was also found by Huang et al.[34] This structural disorder in the catalyst does not seem particularly beneficial for the CO_2 reduction performance in terms of selectivity, however, as can be seen in the measured products in Figure 4.3b. Most notably, the ethylene (C_2H_4) selectivity is considerably higher for the more ordered 100 nm Cu sample and the carbon monoxide (CO) selectivity is higher for the 20 nm Cu catalyst. Whereas copper is normally known to produce C_2-products, with the 20 nm Cu catalyst very little C_2-products were detected. A higher degree of the variation between the first and second EXAFS scans was observed for the 20 nm sample compared to the 100 nm sample (Figure C1). This result seems to imply that the restructuring of the 20 nm sample takes quite long. These data are similar to the results found by Huang et al. where restructuring processes were also slow (minutes and even hours) and still strongly influenced the hydrogen evolution reaction (HER) compared to CO_2 reduction selectivity.[34]

Effect of applied current density. As copper is known to readily restructure during CO_2 reduction as well as form oxides in air or at a positive applied potential, it is necessary to examine its surface structure and composition under a wide variety of conditions. It is critical to know whether the changes in the reaction environment as a function of applied current density or potential might change the structure of the catalyst, and if this may contribute to a variation in product distribution.

To probe this question directly, we compared the XAS spectra obtained under ex situ, open circuit potential and two applied current densities (100 and 200 mA/cm^2) in 1 M KOH. In Figure 4.4 and Table 4.2 the change in the catalyst structure between the ex situ and open circuit cases is shown. Note that this graph is the FT of the data in Figure 4.1c and 4.1d. From the FT spectra it can be observed from the peak at 2.2 Å that the ex situ Cu film has a smaller crystallite size than Cu during CO_2 reduction, but is larger compared to the sample under open circuit conditions (V_{OC}). In V_{OC} (+0.7 V vs. RHE), the potential is close to an oxidising potential, making the sample less resistant against restructuring induced by a combination of potential and a highly alkaline environment. For example, during all XAS experiments on the Cu GDEs, a restructuring of the Cu was observed to either smaller crystallites or slightly oxidised copper after the negative applied potential was turned off and the sample was left in open circuit conditions. This restructuring seemed to take place immediately as the copper was kept

in open circuit conditions (the V_{OC} measurement was started directly after the applied current density experiment).

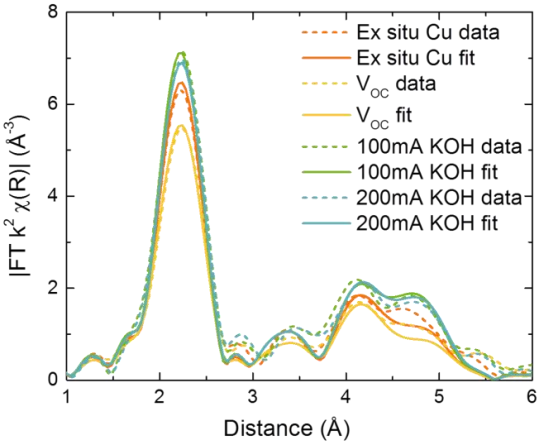

Figure 4.4. FT graphs of EXAFS data shown in Figure 4.1 of a 100 nm Cu film under various conditions: ex situ (orange), under open circuit potential (yellow), at 100 and 200 mA/cm² (green and blue) applied current density. Note that the 100mA and 200mA labels in the figure correspond to 100 and 200 mA/cm² current density.

Table 4.2. EXAFS fitting results of Figure 4.4. Fitted R (Cu-Cu distance), N (coordination numbers) and σ^2 (Debye-Waller factor) of first to fourth shell and the EXAFS diameter calculated using equation 4.1 with N_1. Note that the 100mA and 200mA labels in the table correspond to 100 and 200 mA/cm² current density. The errors to the last digit are reported in parentheses.

	Ex situ Cu	**V_{oc}**	**100mA KOH**	**200mA KOH**
R_1 (Å)	2.537(5)	2.54(2)	2.534(5)	2.54(2)
N_1	7.4(7)	7.5(7)	8.1(7)	8.2(7)
σ^2_1 (Å²)	0.0057(6)	0.007(6)	0.0056(7)	0.0059(5)
R_2 (Å)	3.59(1)	3.59(2)	3.58(2)	3.59(2)
N_2	2.8(7)	2.8(8)	3.2(7)	3.3(7)
σ^2_2 (Å²)	0.0045(5)	0.0062(8)	0.0056(5)	0.0057(7)
N_3	8.0(7)	8.1(7)	8.6(7)	8.7(7)
σ^2_3 (Å²)	0.009(4)	0.010(3)	0.010(3)	0.009(3)
N_4	2.8(8)	3.1(8)	4.2(8)	4.5(7)
σ^2_4 (Å²)	0.011(5)	0.014(5)	0.011(5)	0.012(5)
EXAFS diameter (Å)	10(1)	10(1)	12(1)	12(1)

Although the exact amount of polydispersity is difficult to obtain directly from EXAFS data, some important observations can be made. It can be argued that a high degree of polydispersity in a fcc structure would produce a strong suppression of the coordination number of the higher (third and fourth at 4 - 5 Å) shells. The Cu thin films presented in this work have a similar intensity ratio between the different shells as a bulk metal foil would have, indicating a rather monodisperse material once held under fixed reaction conditions.

In summary, the Cu gas diffusion electrode-based cell design for operando XAS allows the ability to obtain quantitative XANES and EXAFS data for a wide variety of operating conditions. Differences in crystallite size between the 20 and 100 nm Cu films during CO_2 reduction were observed under reaction conditions. Significant changes were found for a 100 nm Cu GDE between the ex situ, open circuit and applied current density conditions. This is very important to note since not all catalyst characterisation can be performed under operando conditions, while it clearly does influence the catalyst's electronic and structural properties. Interestingly, a strong difference was not found between the samples that had an applied current density of 100 and 200 mA/cm^2. Likewise, the spectra in Figure 4.2a of 1 and 100 mA/cm^2 in 1 M $KHCO_3$ are very similar as well. Surprisingly, no clear correlation between material properties and product selectivity as a function of current density was found on the sputtered copper samples.

4.4 Results – operando XAS on silver GDEs

Silver is an excellent catalyst for the selective reduction of CO_2 to CO, showing the ability to operate at low overpotentials and remain highly selective and stable especially when used in a GDE configuration.[25,38] Similar to copper, silver can be deposited on a GDE by various techniques such as sputtering, air brushing or electrodeposition and needs no additional pre-treatment to be highly active. Nonetheless, these single metal catalysts reach a selectivity for CO_2 reduction over the hydrogen evolution reaction (HER) that is many times higher than in an aqueous H-cell configuration that is constrained to limited current densities by the concentration and transport of CO_2.[25] On silver based GDEs, 99% Faradaic efficiency toward CO_2 reduction products is easily reached, whereas only with intricate or highly nanostructured catalyst designs was it possible to reach close to 90% FE in H-cells, at a far lower current density (~1 mA/cm^2) and higher overpotentials.[38,39,40] For H-cell configurations, it has been speculated that the low buffer capacity in nanostructured catalysts enables the local pH in the near vicinity of the electrode to rise, suppressing HER and reaching higher FEs for CO_2 reduction products.[41] In addition, material changes invoked by the catalyst fabrication method in the form of exposing specific crystal facets, defects or dopant insertion, can play a role in making the catalyst electrode more selective.[15,29,42,43] In the case of Ag GDE systems, the pH is responsible for the change in product selectivity. The HER is a pH-dependent

reaction, whereas CO_2 reduction is not, making alkaline conditions a suitable environment to favour CO_2 reduction over the HER.

Figure 4.5a shows the Fourier transformed spectra of several 100 nm silver samples deposited on GDEs and tested under various reaction conditions. An ex situ measurement (orange) is compared to operando samples held at 1 mA/cm^2 (yellow), 100 mA/cm^2 (green) and 200 mA/cm^2 (blue) in 1 M KOH, performed under CO_2 reduction conditions. The FT spectra of these measurements show a strong Ag-Ag signal in the first shell at 2.5 Å, but the higher shells have a relatively dampened signal. This implies that the sample is very polydisperse in crystallite size and it could also account for the mismatch in the FT fits. Notably, the fit in $k^2\chi(k)$ (Figure 4.5b) is quite good, however, so the distances and Debye-Waller factors seem to be reasonable. The $k^2\chi(k)$ spectra corresponding to all FT spectra in Figure 4.5a are presented in Figure C2.

To identify the exact difference in structure and composition between these spectra, an EXAFS fitting analysis was performed using *GNXAS*. This software package fits the entire EXAFS range, rather than shell by shell. The silver EXAFS analysis reveals the presence of a Ag-X contribution in samples held at higher current densities (Table 4.3) where X is a light and small element such as O, C or N. The Ag-X distance is very short compared to the other shell distances, with a size in the range of 2.05 – 2.07 Å. A possible candidate for X that fits these distances is oxygen. The Ag-X distance is slightly longer than for pure silver oxide (1.90 – 2.05 Å) but shorter than the recently found long Ag-O bonds on oxide-derived silver or the bond between Ag and a SiO_2 support.[15,44] A shorter distance or bond length means a stronger interaction between the species and possibly a (locally) positively charged silver. A Ag-O distance between 2.04 and 2.20 Å has been found to belong to linear two-fold oxygen coordinated Ag-O: O-Ag-O.[45] Ag-CO and Ag-OH on a Ag(110) surface were calculated to be 2.262 and 2.210 Å, respectively. Another candidate for X could be carbon. For Ag-C, a bond length of 2.214 and 2.336 Å for the vertically and horizontally adjacent Ag atoms was calculated.

Ex situ HR-SEM, XRD and XPS revealed the presence of monoclinic kalicinite ($KHCO_3$) crystals on the surface of the sample tested at 1 mA/cm^2 in 1M KOH, which could potentially give rise to a Ag-C signal (Figure C3 and C4). However, there are no kalicinite crystals found on the 100 and 200 mA/cm^2 KOH samples, which is where the Ag-X contribution was observed. When the silver is negatively charged, potassium ions near its surface will not be fully solvated anymore and the bond between silver and potassium can become direct, without any water molecules in between them.[46] However, the Ag-K distance was found to be 3.30 Å, and can therefore not account for the short distance that was found in the fitting process.[47] The most likely candidate for X seems to be oxygen, but the role of the Ag-O bond in this system remains unclear.

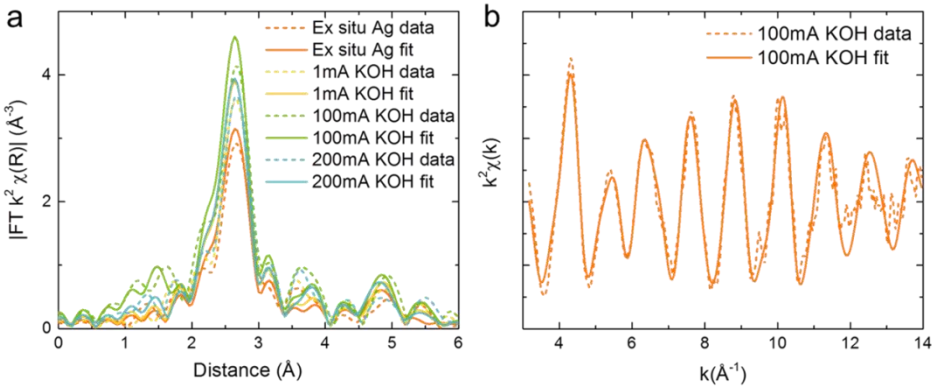

Figure 4.5. (a) FT graphs of EXAFS data and fits of 100 nm Ag samples under various conditions: ex situ, and under 1, 100 and 200 mA/cm² applied current density in 1 M KOH. (b) $k^2\chi(k)$ and fit of the Ag GDE at 100 mA/cm² in 1 M KOH. Note that the 1mA, 100mA and 200mA labels in the figures correspond to 1, 100 and 200 mA/cm² current density.

Table 4.3. EXAFS fitting results of Figure 4.5a. Fitted R (Ag-Ag distance), N (coordination numbers) and σ^2 (Debye-Waller factor) of first to fourth shell and the EXAFS diameter calculated using equation 4.1 for N_1. Note that the 1mA, 100mA and 200mA labels in the table correspond to 1, 100 and 200 mA/cm² current density. The errors to the last digit are reported in parentheses.

	Ex situ Ag	**1mA KOH**	**100mA KOH**	**200mA KOH**
$\mathbf{R_{Ag\text{-}O}}$ **(Å)**	0	0	2.074(5)	2.050(5)
$\mathbf{N_{Ag\text{-}O}}$	0	0	1.2(5)	1.2(5)
$\mathbf{\sigma^2_{Ag\text{-}O}}$ **(Å²)**	0	0	0.0059(5)	0.0059(6)
$\mathbf{R_1}$ **(Å)**	2.874(4)	2.867(4)	2.864(4)	2.864(4)
$\mathbf{N_1}$	6.0(7)	7.4(7)	8.7(6)	7.5(5)
$\mathbf{\sigma^2_1}$ **(Å²)**	0.0055(4)	0.0055(4)	0.0055(5)	0.0055(4)
$\mathbf{R_2}$ **(Å)**	4.06(6)	4.06(6)	4.05(6)	4.05(6)
$\mathbf{N_2}$	1.8(7)	2.8(7)	3.7(7)	2.8(7)
$\mathbf{\sigma^2_2}$ **(Å²)**	0.010(5)	0.010(5)	0.009(5)	0.007(5)
$\mathbf{N_3}$	6.8(7)	8.0(7)	8.3(8)	8.1(8)
$\mathbf{\sigma^2_3}$ **(Å²)**	0.010(5)	0.010(5)	0.010(7)	0.010(7)

When comparing the data in Figure 4.5a, it was found that all samples under operando conditions and the ex situ sample have similar Ag-Ag distances (R_1-R_4) and similar Debye-Waller factors. The main deviation is found in the coordination numbers. The coordination number and its derived dimension have a large standard deviation due to the strong polydispersity in the silver samples. To determine the upper bound of the particle size distribution, a Scherrer analysis on an XRD diffractogram of a fresh 100 nm

Ag sample was performed and revealed a 20 nm grain size, determined by the Ag(220) reflection at 76.6° 2θ. This is considerably higher than the upper bound of the copper samples, indicating a larger range of particle sizes within the silver samples compared to copper.

The overall trends that can be distinguished from the silver GDE experiments are an increase in size when comparing ex situ to operando samples and a decrease in Ag-Ag distance. For higher current densities the appearance of a small Ag-O contribution is identified.

4.5 Discussion

While ex situ, open circuit and operando applied current density spectra reveal a difference in crystallite size in both Cu and Ag samples, interestingly enough, no clear correlation is found between the different operating current densities. This is surprising especially for copper since several papers have shown the selectivity of CO_2 reduction products to vary with the applied current density.[6,37] Often, lower current densities produce mainly H_2 and CO and at higher applied current densities the product distribution becomes more C_2 dominant. From the results in the current work it appears that this selectivity variation is not related to structural changes in the catalyst, rather, it is most likely related to changes in potential and the local concentration of reactant species. The big difference between the ex situ and operando spectra for both copper and silver does however indicate a large degree of restructuring during the initial stages of operation. Given the length of these and most other operando studies, it is uncertain whether further restructuring might occur after hundreds of hours of operation. As we reach the point where we are investigating catalysts for industrial use (thousands of hours) operando spectroscopy could play an important role in observing and identifying the mechanisms behind catalyst (in)stability.

Another observation made in this work was the varying degree of polydispersity found in the silver and copper GDEs and warrants further investigation. Therefore, an additional analysis on the obtained copper and silver data was performed on the coordination numbers found through EXAFS fitting to determine the variation between coordination numbers of different shells within one sample. Since the coordination numbers are used to determine the crystallite size, a variation in coordination number indicates a variation in crystallite size. The coordination numbers (N) are normalised with respect to their bulk values (z_i) which are 12, 6, 24 and 12 for the first through fourth shell giving N/z_i. The normalised coordination numbers are then plotted as a function of their shell number (Figure 4.6). Here, the coordination numbers are compared to the expected N/z_i values for a spherical particle based on their N_1 value and equation 4.1, and the expected values are represented by the solid lines in Figure 4.6. Any deviation of the actual data points (symbols) from their corresponding solid lines can be

interpreted to arise from one of three mechanisms. Either the particles are not spherical, or the error in the fitting process causes the deviation, or the samples are so polydisperse that they don't adhere to equation 4.1. HR-SEM (Figure C4a) shows the presence of spherical particles, so this does not seem to be a likely candidate to explain the deviation. Note that the HR-SEM image only shows the largest clusters around 20 nm, the smaller clusters as identified by EXAFS analysis cannot be seen due to the limit in image resolution. This limitation means that HR-SEM in the current case cannot be used for a full polydispersity analysis. The error in coordination number is up to 20% (see Table 4.1-4.3), which is enough to explain the deviation found between actual data and the theoretical prediction of equation 4.1 in the case of copper (Figure 4.6a). For example, the actual N/z_3 for the Cu sample tested at 100 mA/cm² in 1 M KOH is 0.36, whereas equation 4.1 predicts 0.45. This difference can be explained by a 20% error and is the biggest outlier in Figure 4.6a. In the case of silver however, N/z_3 of the sample tested at 100 mA/cm² in 1 M KOH is 0.35 while equation 4.1 predicts 0.53, a 50% difference. For silver it therefore seems that the catalysts show a higher level of polydispersity in their films compared to copper.

The main difference between the silver and copper catalysts on GDEs is then the level of polydispersity that is larger for the silver samples. Both catalysts show variation in crystallite size between ex situ and CO_2 reduction conditions. The involvement of oxygen was found for silver and not for copper, implying that there could be a mechanistic difference between the two catalysts.

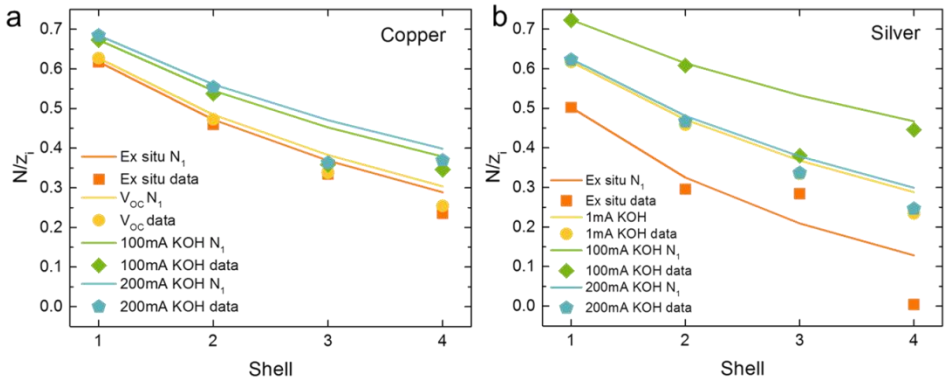

Figure 4.6. Normalised coordination numbers per shell (N/z_i, squares) are compared to the expected coordination numbers for a spherical particle, calculated using equation 4.1 based on N_1 (lines). Coordination numbers of (a) the copper data presented in Figure 4.4 and (b) the silver data presented in Figure 4.5a. Note that the 1mA, 100mA and 200mA labels in the figures correspond to 1, 100 and 200 mA/cm² current density.

4.6 Conclusions

In this work, we provide a detailed approach to design and perform operando XAS studies for electrochemical CO_2 reduction systems using a gas diffusion electrode based system. The presented configuration not only allowed for high-quality spectra to be obtained, but was demonstrated to work under a range of operating conditions which more closely resemble the needs of practical applications in the electrochemical field the last couple of years. The GDE configuration is well-suited to a back-irradiation geometry due to the porous and thin catalyst layer, overcoming design and operational challenges of previous operando systems. In the future, this cell design could easily be adopted to accommodate MEA-based electrodes.

Several results using two common electrochemical CO_2 reduction catalysts, copper and silver, deposited onto GDEs are presented as well, demonstrating the approach can be used for more than one of the catalytic materials and structures that have been developed over the last decade. The copper samples were shown to severely alter their structure in terms of crystallite size and amount of disorder upon a change from ex situ to open circuit and applied current density conditions. However, there exists little difference in size between different applied current densities. When comparing the 20 nm and 100 nm Cu samples, the 20 nm sample exhibited increased structural disorder and decreased crystallite size.

On the silver samples at high applied current density, a Ag-X contribution was found and is ascribed to Ag-O. Similar to copper, the silver crystallite size of the ex situ sample is smaller than the samples during CO_2 reduction. However, the strong degree of polydispersity found in the silver samples is very different than what was observed for the copper coated electrodes.

In short, an operando XAS system can provide unique information about the catalytic structure of CO_2 reduction catalysts. Pairing operando XAS data with electrocatalytic performance data, system modelling and highly sensitive ex situ material characterisation techniques offers a unique approach to study electrochemical catalysts in general and help further CO_2 reduction research in particular.

4.7 Experimental section

Sample fabrication. Copper and silver where sputtered in 100 and 20 nm layers by direct current magnetron sputtering in an AJA magnetron sputtering system on Sigracet 39 BC carbon paper containing 5% PTFE to ensure hydrophobicity.

Electrochemical characterisation. Gaseous products from CO_2 reduction were measured on an online Compact GC (Compact GC 4.0 from Global Analytical Solutions with H2/O2/C1-C5 analyser). The GC took an aliquot every three minutes. CO_2

reduction was performed for 23 minutes at a fixed current density of -1, -100 and -200 mA/cm^2 supplied by a Parstat 4000 potentiostat from Ametek. The reaction was performed in a homemade PMMA 3-compartment flow cell.[24] A peristaltic pump supplied either 1 M KOH (40 wt% KOH in H_2O, Sigma Aldrich) or 1 M CO_2-saturated $KHCO_3$ (99.95% K_2CO_3 from Sigma Aldrich) to both the anodic and cathodic liquid compartment at 15 ml/min. The gas compartment was purged with 10 ml/min 99.99% CO_2. A Ni mesh was used as counter electrode in the KOH experiments, a Pt wire was used as counter electrode in the $KHCO_3$ experiments. A glass Ag/AgCl electrode (saturated KCl, XR300, Radiometer Analytical) was used as reference electrode. An anion exchange membrane (Fumasep FAB-PK-130) separated the liquid compartments. The solvent resistance (R_u) was between 3 and 6 Ω in all experiments as measured via electrochemical impedance spectroscopy.

XAS characterisation. X-ray absorption spectra were recorded at the Dutch-Belgian beamline (DUBBLE, 26A) of the European Synchrotron Radiation Facility (ESRF) in Grenoble, France. Silver K-edge (25515.59 eV) spectra were recorded between 25300 and 26055 eV. Copper K-edge (8980.476 eV) spectra were recorded between 8879 and 9679 eV. The energy of the X-ray beam was tuned by a double-crystal monochromator operating in fixed-exit mode using a Si(111) crystal pair. XANES and EXAFS spectra of the samples were collected in fluorescence mode using a 9-element Ge detector (Ortec Inc.), whereas reference spectra of the metallic Ag and Cu foil and the silver and copper oxides were collected in transmission mode using Ar/He-filled ionisation chambers at ambient temperature and pressure. The photon flux of incoming X-rays is ~2.5 * 10^{10} photons/cm^2. All samples were measured in a standard 45° fluorescence configuration. EXAFS data analysis was performed on data that was averaged from three 20-minute scans.

For the operando measurements the same electrochemical cell as described for the electrochemical measurements was used. The gas compartment contained a Kapton-tape covered window through which the X-rays could reach the backside of the sample. A Biologic SP240 potentiostat was used to control the current density in a three-electrode configuration. The catalyst behaviour in a GDE cell is compared to behaviour in an H-cell using XAS. To keep other parameters unchanged, the H-cell behaviour is measured in the same cell (on a GDE) but with CO_2 dissolved in electrolyte and the back of the GDE taped so no gasses can enter or leave through there.

EXAFS data analysis. Because of the cell design, measurements could not be performed in transmission geometry. Instead, the EXAFS spectra were acquired in fluorescence mode under a 45° angle of incidence. The thin film samples abide the dilute sample approximation necessary for proper data extraction of fluorescence geometry measurements and did therefore not need any self-absorption correction data treatment. Spectra taken of the same sample were combined and normalised. The recorded and

analysed k-range was 3.1 – 13.5 $Å^{-1}$ for the copper data and 3.1 – 14 $Å^{-1}$ for the silver data.

Data extraction and EXAFS analysis were carried out with the *GNXAS* package for both Cu and Ag EXAFS data.[48,49,50] In this approach, the local atomic arrangement around the absorbing atom is decomposed into model atomic configurations containing *2*,...,*n* atoms. The theoretical EXAFS signal χ(k) is given by the sum of the *n*-body contributions γ^2, γ^3,…., γ^n, which take into account all the possible single and multiple scattering (MS) paths between the *n* atoms. The fitting of χ(k) to the experimental EXAFS signal allows to refine the relevant structural parameters of the metal Cu/Ag coordination shells; the suitability of the model is also evaluated by comparison of the experimental EXAFS signal Fourier transform (FT) with the FT of the calculated χ(k) function. Assuming that the Cu and Ag crystallites have a fcc structure, two γ^2 terms take into account the first and second coordination shell, respectively. The first-shell M−M R_1 distance is linked to the fcc a-axis length (the lattice constant a) by $R_1 = a/\sqrt{2}$, while the second neighbours are placed at R_2 = a. The higher shells are calculated according to three-body contributions: the third-shell term, at $R_3 = a*\sqrt{1.5}$, is relative to an isosceles triangle with two first neighbour R_1 sides and vertex angle θ = 120°, whereas the fourth shell contribution, involving particularly strong multiple scattering contributions, is obtained from the degenerate (θ = 180°) triangle formed by three aligned first neighbours and is $R_4 = a*\sqrt{2}$. Since all distances R_i are a function of a, only a needs to be determined. Then, the lattice constant a, the Debye−Waller factors, and the crystallite size are the only parameters needed for the structural analysis of the two metals Cu and Ag respectively. When needed, for the Ag catalyst an extra γ^2 contribution has been added to consider the Ag-O distance. Errors were determined with a 95% confidence interval as described in the *GNXAS* package. The error in N is larger than might be expected because the parameters N and σ^2 are correlated in *GNXAS*. The dimension was allowed to vary up to a maximum value based on XRD and EXAFS metal foils data.

Ex situ catalyst characterisation. XRD patterns (25°−100° 2θ) were collected using a Bruker D8 Advance X-ray diffractometer in Bragg−Brentano configuration with a cobalt source (λ = 1.7889 Å). XPS experiments were conducted using a Thermo Scientific K-alpha apparatus equipped with an Al K-alpha X-ray Source and a Flood Gun to avoid charging of the sample. Parameters used for the measurements were: spot size of 400 μm, pass energy of 50 eV, energy step size of 0.1 eV, dwell time of 50 ms, 10 scans in the vicinity of the Ag 3d, C 1s and O 1s orbital binding energy. HR-SEM images were taken with a Nova NanoSEM at an accelerating voltage of 5 kV. Samples were rinsed with water and dried with nitrogen before ex-situ material characterisation.

4.8 References

(1) Burdyny, T.; Smith, W. A. CO 2 Reduction on Gas-Diffusion Electrodes and Why Catalytic Performance Must Be Assessed at Commercially-Relevant Conditions. Energy Environ. Sci. 2019, Advance Ar.

(2) Higgins, D.; Hahn, C.; Xiang, C.; Jaramillo, T. F.; Weber, A. Z. Gas-Diffusion Electrodes for Carbon Dioxide Reduction: A New Paradigm. ACS Energy Lett. 2019, 4, 317–324.

(3) Zheng, T.; Jiang, K.; Ta, N.; Hu, Y.; Zeng, J.; Liu, J.; Wang, H. Large-Scale and Highly Selective CO 2 Electrocatalytic Reduction on Nickel Single-Atom Catalyst. Joule 2019, 3, 265–278.

(4) Zhang, L.; Zhao, Z.-J.; Gong, J. Nanostructured Materials for Heterogeneous Electrocatalytic CO2 Reduction and Related Reaction Mechanisms. Angew. Chemie Int. Ed. 2017, 56, 11326–11353.

(5) Lv, J. J.; Jouny, M.; Luc, W.; Zhu, W.; Zhu, J. J.; Jiao, F. A Highly Porous Copper Electrocatalyst for Carbon Dioxide Reduction. Adv. Mater. 2018, 30, 1803111.

(6) Dinh, C.-T.; Burdyny, T.; Kibria, G.; Seifitokaldani, A.; Gabardo, C. M.; Arquer, F. P. G. de; Kiani, A.; Edwards, J. P.; Luna, P. De; Bushuyev, O. S.; et al. CO2 Electroreduction to Ethylene via Hydroxide-Mediated Catalysis at an Abrupt Reaction Interface. Science (80-.). 2018, 360, 783–787.

(7) Garza, A.; Bell, A. T.; Head-Gordon, M. Is Subsurface Oxygen Necessary for the Electrochemical Reduction of CO 2 on Copper? J. Phys. Chem. Lett. 2018, 9, 601–606.

(8) Handoko, A. D.; Wei, F.; Jenndy; Yeo, B. S.; Seh, Z. W. Understanding Heterogeneous Electrocatalytic Carbon Dioxide Reduction through Operando Techniques. Nat. Catal. 2018, 1, 922–934.

(9) Gao, D.; Zegkinoglou, I.; Divins, N. J.; Scholten, F.; Sinev, I.; Grosse, P.; Roldan Cuenya, B. Plasma-Activated Copper Nanocube Catalysts for Efficient Carbon Dioxide Electroreduction to Hydrocarbons and Alcohols. ACS Nano 2017, 11, 4825–4831.

(10) Baruch, M. F.; Pander, J.; White, J. L.; Bocarsly, A. B. Mechanistic Insights into the Reduction of CO2 on Tin Electrodes Using In Situ ATR-IR Spectroscopy. ACS Catal. 2015, 150413134326004.

(11) Bohra, D.; Ledezma-Yanez, I.; Li, G.; de Jong, W.; Pidko, E. A.; Smith, W. A. Lateral Adsorbate Interactions Inhibit HCOO − While Promoting CO Selectivity for CO 2 Electrocatalysis on Silver. Angew. Chemie - Int. Ed. 2019, 58 (5), 1345–1349.

(12) Mahoney, M. R.; Howard, M. W.; Cooney, R. P. Carbon Dioxide Conversion to Hydrocarbons at Silver Electrode Surfaces. Chem. Phys. Lett. 1980, 71, 59–63.

(13) Rosen, J.; Hutchings, G. S.; Lu, Q.; Forest, R. V.; Moore, A.; Jiao, F. Electrodeposited Zn Dendrites with Enhanced CO Selectivity for Electrocatalytic CO 2 Reduction. ACS Catal. 2015, 5, 4586–4591.

(14) Jeon, H. S.; Sinev, I.; Scholten, F.; Divins, N. J.; Zegkinoglou, I.; Pielsticker, L.; Roldan Cuenya, B. Operando Evolution of the Structure and Oxidation State of Size-Controlled Zn Nanoparticles during CO 2 Electroreduction. J. Am. Chem. Soc. 2018, 140, 9383–9386.

(15) Firet, N. J.; Blommaert, M. A.; Burdyny, T.; Venugopal, A.; Bohra, D.; Longo, A.; Smith, W. A. Operando EXAFS Study Reveals Presence of Oxygen in Oxide-Derived Silver Catalysts for Electrochemical CO 2 Reduction. J. Mater. Chem. A 2019, 7, 2597–2607.

(16) Velasco-Vélez, J. J.; Jones, T.; Gao, D.; Carbonio, E.; Arrigo, R.; Hsu, C. J.; Huang, Y. C.; Dong, C. L.; Chen, J. M.; Lee, J. F.; et al. The Role of the Copper Oxidation State in the Electrocatalytic Reduction of CO2 into Valuable Hydrocarbons. ACS Sustain. Chem. Eng. 2019, 7 (1), 1485–1492.

(17) Weng, Z.; Wu, Y.; Wang, M.; Jiang, J.; Yang, K.; Huo, S.; Wang, X. F.; Ma, Q.; Brudvig, G. W.; Batista, V. S.; et al. Active Sites of Copper-Complex Catalytic Materials for Electrochemical Carbon Dioxide Reduction. Nat. Commun. 2018, 9, 1–9.

(18) Farmand, M.; Landers, A. T.; Lin, J. C.; Feaster, J. T.; Beeman, J. W.; Ye, Y.; Clark, E. L.; Higgins, D.; Yano, J.; Davis, R. C.; et al. Electrochemical Flow Cell Enabling: Operando Probing of Electrocatalyst Surfaces by X-Ray Spectroscopy and Diffraction. Phys. Chem. Chem. Phys. 2019, 21 (10), 5402–5408.

(19) Whipple, D. T.; Finke, E. C.; Kenis, P. J. A. Microfluidic Reactor for the Electrochemical Reduction of Carbon Dioxide: The Effect of PH. Electrochem. Solid-State Lett. 2010, 13 (9), B109.

(20) Zhuang, T.-T.; Pang, Y.; Liang, Z.-Q.; Wang, Z.; Li, Y.; Tan, C.-S.; Li, Y.; Dinh, C. T.; De Luna, P.; Hsieh, P.-L.; et al. Copper Nanocavities Confine Intermediates

for Efficient Electrosynthesis of C3 Alcohol Fuels from Carbon Monoxide. Nat. Catal. 2018, 1, 946–951.

(21) Raciti, D.; Mao, M.; Wang, C. Mass Transport Modelling for the Electroreduction of CO 2 on Cu Nanowires. Nanotechnology 2018, 29, 044001.

(22) Li, J.; Che, F.; Pang, Y.; Zou, C.; Howe, J. Y.; Burdyny, T.; Edwards, J. P.; Wang, Y.; Li, F.; Wang, Z.; et al. Copper Adparticle Enabled Selective Electrosynthesis of N-Propanol. Nat. Commun. 2018, 9, 4614.

(23) Velasco-Velez, J.-J.; Pascal, T. A.; Wan, L. F.; Guo, J.; Prendergast, D.; Salmeron, M. The Structure of Interfacial Water on Gold Electrodes Studied by X-Ray Absorption Spectroscopy. Science (80-.). 2014, 346, 831–834.

(24) Liu, K.; Smith, W. A.; Burdyny, T. Introductory Guide to Assembling and Operating Gas Diffusion Electrodes for Electrochemical CO 2 Reduction. ACS Energy Lett. 2019, 4, 639–643.

(25) Gabardo, C. M.; Seifitokaldani, A.; Edwards, J. P.; Dinh, C.-T.; Burdyny, T.; Kibria, M. G.; O'Brien, C. P.; Sargent, E. H.; Sinton, D. Combined High Alkalinity and Pressurization Enable Efficient CO 2 Electroreduction to CO. Energy Environ. Sci. 2018, 11, 2531–2539.

(26) Tröger, L.; Arvanitis, D.; Baberschke, K.; Michaelis, H.; Grimm, U.; Zschech, E. Full Correction of the Self-Absorption in Soft-Fluorescence Extended x-Ray-Absorption Fine Structure. Phys. Rev. B 1992, 46, 3283–3289.

(27) Xin, H.; Schweitzer, N.; Nikolla, E.; Linic, S. Communications: Developing Relationships between the Local Chemical Reactivity of Alloy Catalysts and Physical Characteristics of Constituent Metal Elements. J. Chem. Phys. 2010, 132, 111101.

(28) Ramaker, D. E.; Korovina, A.; Croze, V.; Melke, J.; Roth, C. Following ORR Intermediates Adsorbed on a Pt Cathode Catalyst during Break-in of a PEM Fuel Cell by in Operando X-Ray Absorption Spectroscopy. Phys. Chem. Chem. Phys. 2014, 16, 13645–13653.

(29) Mistry, H.; Choi, Y.-W.; Bagger, A.; Scholten, F.; Bonifacio, C.; Sinev, I.; Divins, N. J.; Zegkinoglou, I.; Jeon, H. S.; Kisslinger, K.; et al. Enhanced Carbon Dioxide Electroreduction to Carbon Monoxide over Defect Rich Plasma-Activated Silver Catalysts. Angew. Chemie Int. Ed. 2017, 56, 1–6.

(30) Borowski, M. Size Determination of Small Cu-Clusters by EXAFS. Le J. Phys. IV 1997, 7, C2-259-C2-260.

(31) Calvin, S.; Luo, S. X.; Caragianis-Broadbridge, C.; McGuinness, J. K.; Anderson, E.; Lehman, A.; Wee, K. H.; Morrison, S. A.; Kurihara, L. K. Comparison of Extended X-Ray Absorption Fine Structure and Scherrer Analysis of x-Ray Diffraction as Methods for Determining Mean Sizes of Polydisperse Nanoparticles. Appl. Phys. Lett. 2005, 87, 233102 1-3.

(32) Calvin, S.; Miller, M. M.; Goswami, R.; Cheng, S.-F.; Mulvaney, S. P.; Whitman, L. J.; Harris, V. G. Determination of Crystallite Size in a Magnetic Nanocomposite Using Extended X-Ray Absorption Fine Structure. J. Appl. Phys. 2003, 94, 778–783.

(33) Matsui, H.; Ishiguro, N.; Uruga, T.; Sekizawa, O.; Higashi, K.; Maejima, N.; Tada, M. Operando 3D Visualization of Migration and Degradation of a Platinum Cathode Catalyst in a Polymer Electrolyte Fuel Cell. Angew. Chemie - Int. Ed. 2017, 56, 9371–9375.

(34) Huang, J.; Hörmann, N.; Oveisi, E.; Loiudice, A.; De Gregorio, G. L.; Andreussi, O.; Marzari, N.; Buonsanti, R. Potential-Induced Nanoclustering of Metallic Catalysts during Electrochemical CO2 Reduction. Nat. Commun. 2018, 9:3117, 1–9.

(35) Nitopi, S.; Bertheussen, E.; Scott, S. B.; Liu, X.; Engstfeld, A. K.; Horch, S.; Seger, B.; Stephens, I. E. L.; Chan, K.; Hahn, C.; et al. Progress and Perspectives of Electrochemical CO2 Reduction on Copper in Aqueous Electrolyte. Chem. Rev. 2019, 119, 7610–7672.

(36) Bazin, D. C.; Sayers, D. A.; Rehr, J. J. Comparison between X-Ray Absorption Spectroscopy, Anomalous Wide Angle X-Ray Scattering, Anomalous Small Angle X-Ray Scattering, and Diffraction Anomalous Fine Structure Techniques Applied to Nanometer-Scale Metallic Clusters. J. Phys. Chem. B 1997, 101, 11040–11050.

(37) Ma, S.; Sadakiyo, M.; Luo, R.; Heima, M.; Yamauchi, M.; Kenis, P. J. A. One-Step Electrosynthesis of Ethylene and Ethanol from CO2 in an Alkaline Electrolyzer. J. Power Sources 2016, 301, 219–228.

(38) Verma, S.; Lu, X.; Ma, S.; Masel, R. I.; Kenis, P. J. A. The Effect of Electrolyte Composition on the Electroreduction of CO2 to CO on Ag Based Gas Diffusion Electrodes. Phys. Chem. Chem. Phys. 2015, 18, 7075–7084.

(39) Seifitokaldani, A.; Gabardo, C. M.; Burdyny, T.; Dinh, C.-T.; Edwards, J. P.; Kibria, M. G.; Bushuyev, O. S.; Kelley, S. O.; Sinton, D.; Sargent, E. H. Hydronium-Induced Switching between CO 2 Electroreduction Pathways. J. Am. Chem. Soc. 2018, 140 (11), 3833–3837.

(40) Ma, M.; Liu, K.; Shen, J.; Kas, R.; Smith, W. A. In Situ Fabrication and Reactivation of Highly Selective and Stable Ag Catalysts for Electrochemical CO2Conversion. ACS Energy Lett. 2018, 3 (6), 1301–1306.

(41) Yoon, Y.; Hall, A. S.; Surendranath, Y. Tuning of Silver Catalyst Mesostructure Promotes Selective Carbon Dioxide Conversion into Fuels. Angew. Chemie - Int. Ed. 2016, 128, 15508–15512.

(42) Lee, H. E.; Yang, K. D.; Yoon, S. M.; Ahn, H. Y.; Lee, Y. Y.; Chang, H.; Jeong, D. H.; Lee, Y. S.; Kim, M. Y.; Nam, K. T. Concave Rhombic Dodecahedral Au Nanocatalyst with Multiple High-Index Facets for CO2 Reduction. ACS Nano 2015, 9, 8384–8393.

(43) Zhang, Y.; Ji, L.; Qiu, W.; Shi, X.; Asiri, A. M.; Sun, X. Iodide-Derived Nanostructured Silver Promotes Selective and Efficient Carbon Dioxide Conversion into Carbon Monoxide. Chem. Commun. 2018, 54, 2666–2669.

(44) Balerna, A.; Liotta, L.; Longo, A.; Martorana, A.; Meneghini, C.; Mobilio, S.; Pipitone, G. Structural Characterisation of Pumice-Supported Silver-Palladium Metal Clusters by Means of XAFS and AWAXS. Eur. Phys. J. D 1999, 7, 89–97.

(45) Antonio, M. R.; Tsou, D. T. Silver Ion Coordination in Membranes for Facilitated Olefin Transport. Ind. Eng. Chem. Res. 1993, 32, 273–278.

(46) Mills, J. N.; McCrum, I. T.; Janik, M. J. Alkali Cation Specific Adsorption onto Fcc(111) Transition Metal Electrodes. Phys. Chem. Chem. Phys. 2014, 16, 13699–13707.

(47) DFT Calculations of the Interaction of Alkali Ions with Copper and Silver. J. Electroanal. Chem. 2001, 495, 160–168.

(48) Filipponi, A.; Di Cicco, A. Atomic Background in X-Ray Absorption Spectra of Fifth-Period Elements: Evidence for Double-Electron Excitation Edges. Phys. Rev. A 1995, 52, 1072–1078.

(49) Filipponi, A.; Cicco, A. Di. X-Ray-Absorption Spectroscopy and n-Body Distribution Functions in Condensed Matter. II. Data Analysis and Applications. Phys. Rev. B 1995, 52, 15135–15149.

(50) Filipponi, A.; Di Cicco, A.; Renzo Natoli, C. X-Ray-Absorption Spectroscopy and n-Body Distribution Functions in Condensed Matter. I. Theory. Phys. Rev. B 1995, 52, 15122–15134.

Appendix C

Data analysis The raw data obtained in an XAS experiment is often averaged when multiple scans are taken consecutively under the same reaction conditions on one sample. The averaged spectra are then normalised, sometimes smoothed and plotted to show the normalised absorption coefficient μ(E). Often only the 30 - 100 eV after the absorption edge are shown, this is the XANES spectrum. The μ(E) can be converted to give the EXAFS χ(k) as explained in great detail by many other books and papers.[1,2,3] The Fourier Transform (FT) of χ(k) gives a spectrum that is easier to interpret by eye compared to the χ(k) spectrum. The x-axis now displays the distance between the absorber atom and the neighbouring shells, the y-axis is a measure of the intensity. The EXAFS can be fit to the EXAFS equation using different software tools, including GNXAS, Athena and Viper.[4–6,7]

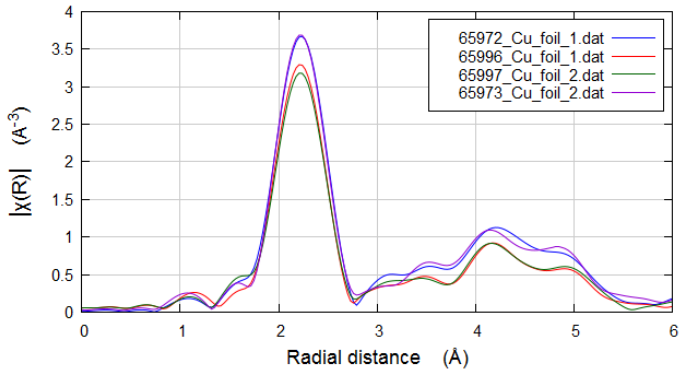

Figure C1. Blue and purple are scan 1 and 2 of the 100 nm Cu GDE 100mA/cm² in KOH, red and green are scan 1 and 2 for the 20 nm Cu GDE at 100 mA/cm² in KOH.

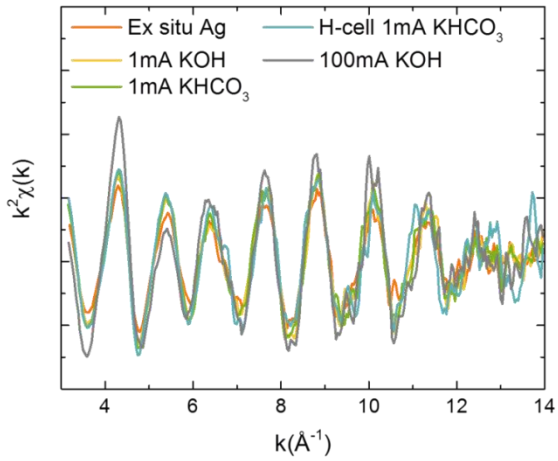

Figure C2. EXAFS data in k2χ(k) for 100 nm Ag GDEs measured under various experimental conditions, the matching FT spectra are shown in Figure 4.5a. Note that the 1mA and 100mA labels in the figures correspond to 1 and 100 mA/cm2 current density.

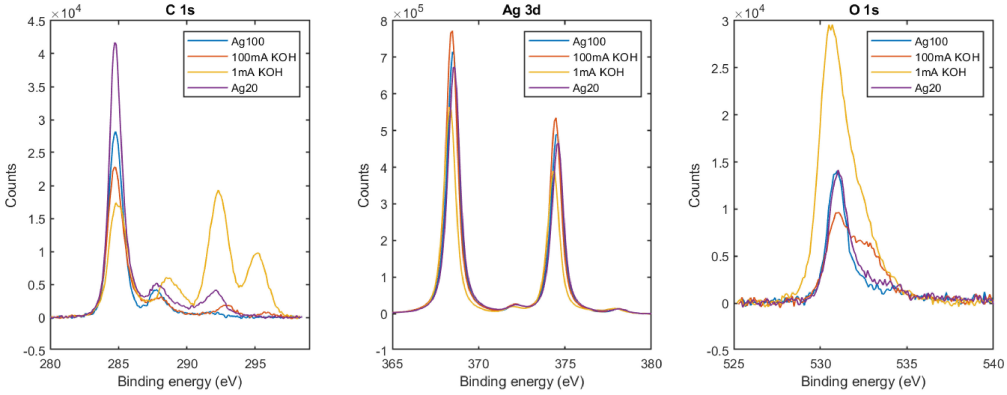

Figure C3. XPS C 1s, Ag 3d and O 1s spectra of a fresh 100 nm Ag on GDE, samples after 1h at 100 mA/cm² and 1 mA/cm² in KOH on a 100 nm Ag GDE and a fresh 20 nm Ag GDE sample. The C 1s graph includes the K 2p signal at 292 and 295 eV. Note that the 1mA and 100mA labels in the graphs correspond to 1 and 100 mA/cm² current density.

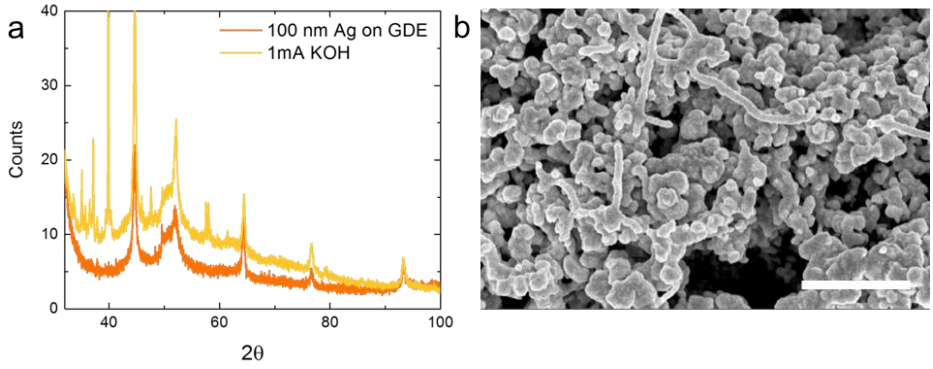

Figure C4. (a) XRD of a fresh 100 nm Ag GDE and a 100 nm Ag GDE after 1h at 1 mA/cm² in KOH sample. Besides the silver and GDE diffraction peaks, the 1 mA KOH sample also gives diffraction peaks of monoclinic kalicinite, or $KHCO_3$ crystals. (b) HR-SEM image of the 1mA KOH sample showing thread-like kalicinite structures on top of the Ag thin film. Scale bar is 1 μm. Note that the 1mA label in the figure corresponds to 1 mA/cm² current density.

References

(1) Vlaic, G.; Olivi, L. EXAFS Spectroscopy : A Brief Introduction. Croat. Chem. Acta 2004, 77 (3), 427–433.

(2) Newville, M. Fundamentals of XAFS. Rev. Mineral. Geochemistry 2014, 78 (1), 33–74.

(3) Calvin, S. XAFS for Everyone; CRC Press, 2013.

(4) Filipponi, A.; Di Cicco, A.; Renzo Natoli, C. X-Ray-Absorption Spectroscopy and n-Body Distribution Functions in Condensed Matter. I. Theory. Phys. Rev. B 1995, 52, 15122–15134.

(5) Filipponi, A.; Cicco, A. Di. X-Ray-Absorption Spectroscopy and n-Body Distribution Functions in Condensed Matter. II. Data Analysis and Applications. Phys. Rev. B 1995, 52, 15135–15149.

(6) Ravel, B.; Newville, M.; Calvin, S. ATHENA, ARTEMIS, HEPHAESTUS: Data Analysis for X-Ray Absorption Spectroscopy Using IFEFFIT. J. Synchrotron Radiat. 2005, 12, 537–541.

(7) Klementev, K. V. Deconvolution Problems in X-Ray Absorption Fine Structure Spectroscopy. J. Phys. D. Appl. Phys. 2001, 34, 209–217.

5

Chemisorption of anionic species from the electrolyte alters the surface electronic structure and composition of photocharged $BiVO_4$

This chapter is based on the following publication:

N.J. Firet*, A. Venugopal* , M.A. Blommaert, C. Cavallari, C.J. Sahle, A. Longo, W.A. Smith. Chemisorption of anionic species from the electrolyte alters the surface electronic structure and composition of photocharged $BiVO_4$. Chem. Mater. 2019, 31, 7453−7462.

* These authors contributed equally to this work.

Photocharging has recently been demonstrated as a powerful method to improve the photo-electrochemical water splitting performance of different metal oxide photoanodes, including $BiVO_4$. In this work, we use ambient-pressure X-ray Raman scattering (XRS) spectroscopy to study the surface electronic structure of photocharged $BiVO_4$. The O K edge spectrum was simulated using the Finite Difference Method Near Edge Structure (FDMNES) method, which revealed a change in electron confinement and occupancy in the conduction band. These insights, combined with ultraviolet-visible spectroscopy (UV-vis) and X-ray photoelectron spectroscopy (XPS) analyses, reveal that a surface layer formed during photocharging creates a heterojunction with $BiVO_4$, leading to favourable band bending and strongly reduced surface recombination. The XRS spectra presented in this work exhibit good agreement with soft X-ray absorption near-edge structure (XANES) spectra from literature, demonstrating that XRS is a powerful tool to study the electronic and structural properties of light elements in semiconductors. Our findings provide direct evidence of the electronic modification of a metal oxide photoanode surface as a result of the adsorption of electrolyte anionic species under operating conditions. This work highlights that the surface adsorption of these electrolyte anionic species is likely present in most studies on metal oxide photoanodes and has serious implications for the photo-electrochemical performance analysis and fundamental understanding of these materials.

5.1 Introduction

Bismuth vanadate ($BiVO_4$) is an extensively investigated n-type metal oxide semiconductor that has shown promising properties for photo-electrochemical (PEC) water splitting.[1] It has generated the highest photocurrent for a metal oxide photoanode to date[2] and the band gap of 2.4 eV could potentially be suitable to make $BiVO_4$ a good top absorber in tandem PEC devices with a low band gap bottom absorber.[3] In addition, the optoelectronic properties of $BiVO_4$ are easily modified: the material can accommodate a large number of defects and dopants, enabling a high degree of material engineering making $BiVO_4$ a suitable model photoanode.[4] Many improvements in the PEC performance of $BiVO_4$ have used the addition of dopants to improve electron conductivity[3,5], or the addition of co-catalysts to improve the kinetics of the oxygen evolution reaction (OER).[6,7]

Interestingly, recent work by Zachäus et al.[8] showed that surface recombination is one of the major performance-limiting factors for $BiVO_4$. In fact, the presence of a cobalt phosphate (CoPi) catalyst on the surface of $BiVO_4$ suppresses surface recombination by aiding the transfer of holes from the semiconductor valence band (VB) to the OER intermediates. While CoPi effectively suppresses surface recombination, it also introduces parasitic light absorption, which is unwanted in a practical device.[9] Recently, the photocharging (PC) technique has been introduced on $BiVO_4$ photoanodes, which drastically reduced the onset potential for OER and increased the photocurrent density and fill factor of PC-$BiVO_4$ compared to untreated $BiVO_4$.[10] This treatment was performed by exposing $BiVO_4$ photoanodes to prolonged exposure to AM1.5 illumination under open circuit conditions in a neutral electrolyte. After extensive material characterisation, it was shown that the surface structure of $BiVO_4$ was altered upon photocharging.[10,11] This treatment lead to a suppression of the surface recombination of photogenerated charge carriers, improving the overall photo-electrochemical performance of $BiVO_4$. In a follow-up work, the pH of the electrolyte was found to have a significant effect on the photocharging enhancement, where an alkaline solution increased the PEC performance more compared to a neutral or slightly acidic electrolyte.[11] Using Intensity-Modulated Photoelectron Spectroscopy (IMPS) and a hole scavenger, Liu et al. quantified the enhancement from photocharging in the bulk and at the surface of $BiVO_4$ in a potassium phosphate buffer.[12] It was demonstrated that photocharging of $BiVO_4$ resulted in a significant enhancement in both the bulk charge separation and surface charge transfer efficiencies. Similar photo-electrochemical enhancements have also been recently shown in other metal oxide photoanodes such as WO_3[13], $CuWO_4$[14] and doped Fe_2O_3[15,16], showing that the photocharging treatment can be extended beyond $BiVO_4$, and is a potentially generalizable phenomenon.

Recently, Favaro et al.[17] have reported the formation of a $Bi_x(PO_4)_y$ layer at the surface of a $BiVO_4$ photoanode when illuminated in a phosphate buffer under open circuit

conditions. A similar copper borate layer was formed during the examination of $CuWO_4$ when it was photocharged in a borate buffer.[14] These results suggest that an overlayer is formed at these metal oxide photoanode surfaces upon illumination by the chemisorption of the electrolyte anionic species. It was proposed that this semiconducting overlayer then creates a heterojunction with the underlying photoanode, improving the charge separation close to the surface and thus suppressing the surface recombination of the photo-excited charge carriers. To better explain the enhancements in charge separation and suppression of surface recombination of the photocharged electrodes, it is necessary to gain further insights into the modification of the electronic structure of the metal oxide photoanodes by this light-induced overlayer. This knowledge can help to improve the general understanding of an illuminated metal oxide/electrolyte interface, which is crucial for the development of PEC water splitting devices. In this work, $BiVO_4$ is used as a model photoanode to study the changes in its electronic structure during photocharging in a borate electrolyte using a combination of X-ray photoelectron spectroscopy (XPS), ultraviolet-visible spectroscopy (UV-vis) and ambient-pressure (in air) X-ray Raman scattering (XRS) spectroscopy. XPS only penetrates the first ~5 nm of the $BiVO_4$ film and therefore provides surface-sensitive information, while both UV-vis and XRS techniques provide bulk-sensitive information. A surface hydroxide layer was found to form spontaneously even when the $BiVO_4$ electrode was placed in the electrolyte in the dark. A bismuth borate layer was formed under the photocharging conditions, creating a heterojunction that resulted in an improved charge separation and decreased charge carrier recombination near the surface as discovered through ab initio simulations of the O K edge spectra of $BiVO_4$. These findings validate the previous hypotheses proposed in literature[17,14], about improved band bending in the space charge region (SCR) as a result of the light-induced heterojunction formation. These results highlight the complex and dynamic nature of metal oxide-electrolyte interfaces, and give new insights into the mechanisms for PEC performance enhancement of photocharged $BiVO_4$ photoanodes. More importantly, this work highlights that the surface adsorption of anionic electrolyte species on metal oxide surfaces cannot be ignored, as it has serious implications on the fundamental understanding and performance analysis of metal oxide photoanodes.

5.2 Experimental section

Fabrication of $BiVO_4$ thin film photoanodes Thin films of $BiVO_4$ were deposited on fluorine-doped tin oxide (FTO) substrates via spray pyrolysis. The details of the experimental procedure can be found elsewhere.[18] In short, FTO substrates were first coated with ~80 nm of SnO_2 while the substrate temperature was kept at 425 °C, and subsequently coated with 200 nm of $BiVO_4$ while the substrate was kept at 450 °C. The samples were then annealed in an air-flushed tube furnace for 2h at 460 °C.

X-ray Raman scattering spectroscopy All X-ray Raman scattering spectroscopy data were gathered using the dedicated large solid angle spectrometer at ID20 beamline of the European Synchrotron Radiation Facility.[19] These experiments were performed in air under atmospheric conditions. A pink beam from four U26 undulators was monochromatised to a 9,686 eV elastic energy, first by using a cryogenically cooled Si(111) monochromator and then a Si(311) Channel Cut post-monochromator. The beam was focused using a mirror system in Kirkpatrick-Baez geometry yielding a spot size of approximately 50 x 100 μm^2 (V x H) at the sample position. Given the experimental setup, the signal coming from 36 spherically bent Si(660) analyser crystals in the vertical scattering plane was exploited. The overall energy resolution was 0.7 eV, and the mean momentum transfer was 6.2 ± 0.4 $Å^{-1}$.

The reference sample used for this study was a $BiVO_4$ film prepared as described above and measured without any further treatment at a 0.5° angle relative to the incidence beam (penetration depth 60 nm). Pellets of cellulose and vanadium oxide (V_2O_4 and V_2O_5 Sigma-Aldrich) were also measured at a 0.5° angle. A grazing incidence angle is required to ensure surface-sensitive measurements when a hard X-ray beam is used. Before the XRS measurements, the dark and PC sample were kept in open circuit conditions in a flow cell with a 0.1 M sodium borate buffer (sodium tetraborate decahydrate (Sigma Aldrich 99.5%) in MilliQ water, while NaOH was added until pH 10 was reached) for 12h in the dark and under illumination, respectively. The flow cell was further equipped with a glass Ag/AgCl reference electrode (XR300, Radiometer Analytical) and a coiled Pt wire as counter electrode both in the dark (dark sample) and under illumination (photocharged sample, 100 mW/cm^2 Xe lamp with water filter). After 12h, the electrodes were removed from the electrochemical cell, quickly dried under a flow of nitrogen and moved to the experimental hutch for the XRS measurements. The preparation procedure was performed very quickly to ensure the XRS measurements could start less than 15 min after the sample was removed from the electrochemical cell. During the XRS measurements, the incident energy was scanned at a fixed analyser energy of 9.7 keV in order to create energy losses in the vicinity of the core-electron excitations of interest ($L_{2,3}$ of V and K edge of O). The data collected by 3 pixelated Maxipix detectors[20] were integrated over appropriated Regions Of Interest (ROI), then averaged over the 36 Si(660) analyser crystals and treated with the XRS-tools

program package. A background accounting for the valence Compton profile was subtracted as described elsewhere.[21] Finally, a normalisation over an area of 40 eV across the edge was applied.

Eight energy loss scans per sample were measured at room temperature, each one at a new sample position to avoid beam radiation damage. All XRS measurements were checked for consistency prior to summation to rule out radiation damage of the sample induced by the X-ray beam.

Ab initio XRS simulations at the O K edge were performed with the Finite Difference Method Near Edge Structure (FDMNES) software package.[22,23] The calculated spectra were compared to both photocharged and dark samples. The input parameter files of the calculations are reported in the Supporting Information (SI). The vanadium L edges were simulated with Crispy[24] using a multiplet analysis approach.

X-ray photoelectron spectroscopy XPS spectra were obtained using a Thermo Scientific K-alpha apparatus equipped with an Al K-alpha X-ray Source and a Flood Gun for charge compensation of the sample. Parameters used for the measurements were: spot size of 400 μm, pass energy of 50 eV, energy step size of 0.1 eV, dwell time of 50 ms, 10 scans in the vicinity of the Bi 4f, C 1s, Na 1s, O 1s and V 2p orbital binding energy with alternative scan numbers for B 1s (200 scans) and the valence band (50 scans). Samples were rinsed and dried before measuring.

UV-Vis spectroscopy UV-Vis transmission measurements were performed on the reference, dark and the photocharged $BiVO_4$ samples using a Perkin Elmer Lambda 900 UV/Vis/NIR spectrometer. The transmission measurements were performed inside an integration sphere in the transmittance mode (%T). Data was recorded with a 15° tilt in the sample, with respect to the incident light beam to minimise reflection. A scan rate of 250 nm/min and an integration time of 0.2 s were used for the data capture. The absorption coefficient and the Tauc plot were calculated from the transmittance data using the formulas in appendix D.

High-resolution Scanning Electron Microscopy HR-SEM images were taken with a Nova NanoSEM at an accelerating voltage of 10 kV.

5.3 Results

To gain further insights into the mechanisms of the photo-electrochemical enhancement that arise from the photocharging procedure in $BiVO_4$, several material properties of $BiVO_4$ were investigated before and after photocharging. In particular, the influence of placing the photoanodes in solution under open circuit conditions with and without illumination were examined. A reference $BiVO_4$ sample (as-deposited) was compared to both a $BiVO_4$ film that was kept under open circuit conditions and AM1.5 light illumination (i.e. photocharged) for 12 h, and a $BiVO_4$ film that was kept in open circuit for 12 h in the dark. The samples are referred to as untreated $BiVO_4$, photocharged $BiVO_4$ (PC-$BiVO_4$) and dark $BiVO_4$, respectively. The samples were studied through several spectroscopic techniques, including UV-Vis spectroscopy, XPS and XRS. Both XPS and XRS give electronic and structural information on the film, however due to the difference in penetrating depth of the X-rays in the different experiments, XPS gives information about the surface of the films while XRS provides information on the structure up to 60 nm into the bulk of $BiVO_4$.

X-ray photoelectron spectroscopy XPS measurements were performed on reference, dark and PC-$BiVO_4$ films, and the results are shown in Figure 5.1. The presented spectra are background subtracted and energy corrected with the C 1s signal (Figure D1d). Several trends can be observed between the different samples. The Bi 4f peaks are shown in Figure 5.1a, and a shift was observed from 159.5 eV for the reference sample to 159.0 eV and 158.7 eV for the dark and photocharged $BiVO_4$, respectively. This shift is accompanied by slight broadening of the Bi 4f peaks for the dark and the photocharged samples, as shown with the increase in full width at half-maximum (FWHM) in Table D1. A signal from the B 1s spectrum is not present in the reference sample, while it appears very small in the dark and is much more pronounced in the PC-$BiVO_4$, as seen in Figure 5.1b. In Figure 5.1c, the main signal from the oxygen (O 1s) spectra was observed to decrease slightly in binding energy from 530.3 eV for the reference sample to 529.9 eV and 529.6 eV for the dark and PC-$BiVO_4$ samples, while the shoulder peak at 531 eV grows significantly (deconvolution of the O 1s peaks is given in Figure D1). The peak signal from the V 2p spectra is shown in Figure 5.1c, where a shift to lower binding energies is observed along with a strong signal decrease when looking at the reference, dark and PC-$BiVO_4$ films, respectively.

When these results are compared to prior literature, several important similarities can be seen. Favaro et al. found a bismuth phosphate layer forming on the surface of the $BiVO_4$ films under illumination that slowly disappeared again after the light was turned off.[17] In our current work, the buffer used is not a phosphate but rather a borate electrolyte. The binding energies of Bi to borate and phosphate are not the same, which implies that the peak shift found in our Bi 4f spectrum is not the same as in the work by Favaro. A previous report on B_2O_3-Bi_2O_3 glasses reported the Bi 4f binding energies of

Bi-O-Bi at 159.85 eV and B-O-Bi at 158.7 eV, which was explained by the presence of boron shifting the Bi signal to lower binding energies.[25] In addition, the O 1s binding energies were reported to be 530.35 eV for Bi_2O_3 and 530.95 eV for B_2O_3. In our work, we find a shoulder in the O 1s spectra at 531.0 eV to increase during photocharging, and coincide with the emergence of the B 1s peak at 192.0 eV (Figures 5.1b,c, and D1). We therefore ascribe the shift and the broadening of the Bi 4f peak, the emergence of the O 1s shoulder together with the B 1s peak to reveal the formation of a surface bismuth borate layer during photocharging. This surface borate layer is very similar to the phosphate layer found by Favaro et al. In addition to the XPS data given for Bi, B and O, we also observed a shift toward lower binding energies for the V 2p signal, which indicates a reduction in the oxidation state of the vanadium.[11]

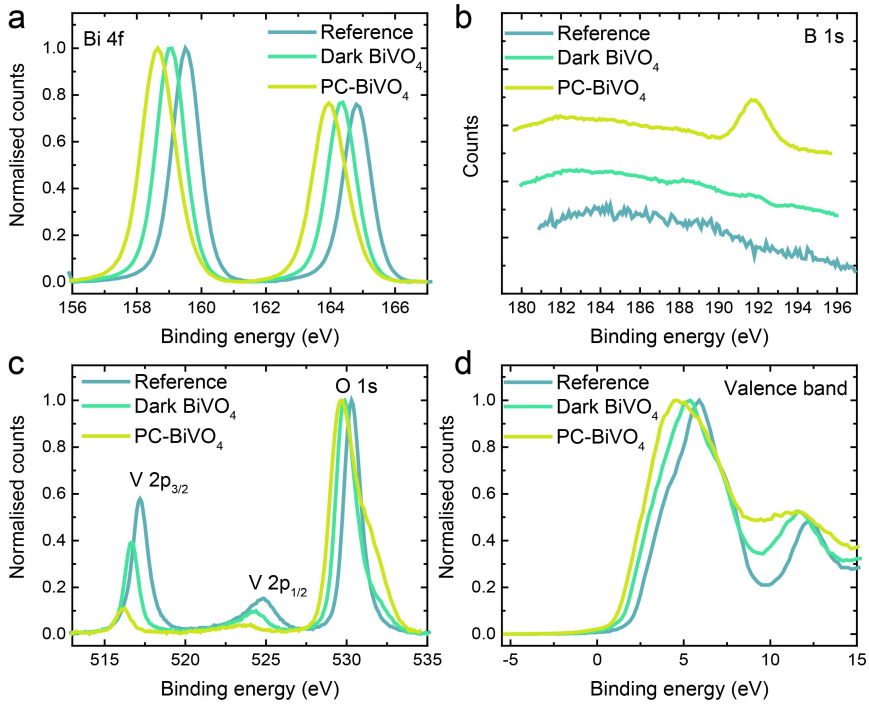

Figure 5.1. XPS spectra of the reference $BiVO_4$, and the dark and PC-$BiVO_4$ after 22h under open circuit conditions in a borate buffer electrolyte. Spectra of (a) Bi 4f, (b) B 1s, (c) V 2p and O 1s and (d) the valence band are shown.

When considering the difference between the dark and photocharged samples, it is interesting to note that the electronic features of the dark sample show an intermediate phase between the photocharged and the reference sample. Since the dark sample has no clear B 1s signal, yet still has a partial shoulder in the O 1s spectrum, it is likely that this sample instead has a surface coverage of bismuth hydroxide as previously

reported.[11] Since the binding energies for Bi-O-B and Bi-O-H are almost identical (the electronegativity values of H and B are 2.2 and 2.0, respectively), the distinction is difficult to make without analysing the B 1s signal as well.

The valence band (VB) of the reference, dark and PC-$BiVO_4$ electrodes was also examined, and is shown in Figure 5.1d. It can be seen from this figure that similar to the previously observed shifts in the binding energy of Bi, O and V, there is also a shift in the valence band energy toward lower binding energies when looking at the reference, dark and PC-$BiVO_4$ samples, respectively.

A broadening to lower binding energy of the valence band spectra of the dark and PC-$BiVO_4$ is also visible here, due to the convolution of the VB spectra of bismuth hydroxide/bismuth borate and bismuth vanadate, respectively. These results indicate that the bismuth borate layer formed on the surface has a valence band closer to the Fermi level of the composite system. The exact composition of the bismuth borate surface layer is unknown, but from prior work on bismuth borate glasses, we can estimate the band gap of the bismuth borate layer to be equal to or larger than that of $BiVO_4$.[20,26]

The unidirectional peak shifts in the Bi 4f, V 2p, O 1s and VB XPS spectra to lower binding energies are in part an electronic effect. Band bending caused by the equilibration of the Fermi level of $BiVO_4$ and the chemisorbed anionic surface layer shifts the XPS spectra. Similar XPS peak shifts were observed by Hermans et al.[27] where different metal oxide surface layers were deposited on $BiVO_4$, and the peak shifts were attributed to a change in Fermi level position because of the surface layer induced band bending. NiO and CoO_x surface layers lead to an upward band bending whereas indium-doped tin oxide induced a downward band bending in $BiVO_4$, due to the differences in their respective work functions compared to that of $BiVO_4$. The core level XPS spectra shifted to lower binding energies with the deposition of NiO and CoO_x overlayers, similar to the shifts seen with dark and PC-$BiVO_4$ in this study. Note that band bending induced shifts should be equal in magnitude for different core levels. Table D2 shows that the shifts for V and Bi are larger than for O, meaning that the V and Bi shifts also have a chemical component to them, assigned above as a reduction in V oxidation state and the appearance of the Bi borate surface layer.

The formation of the bismuth borate layer at the surface forms a heterojunction with the $BiVO_4$ as well as induces an upward band bending, and reduces photogenerated charge recombination at the semiconductor-liquid junction (SLJ). The cathodic Fermi level shift that was observed with the open circuit potential (OCP) measurements for the dark and photocharged samples, as shown in Figure D2, is another evidence of the band bending observed through the XPS shifts.

Ultraviolet-visible spectroscopy UV-vis spectroscopy was performed before and after the photocharging process to determine if there were any optical changes in the $BiVO_4$ films during the treatment that may arise from the formation of the bismuth borate surface layer. In Figure 5.2a, the spectra of a dark (green) and photocharged (yellow) sample are shown together with their corresponding spectra before treatment. A small increase in absorption is found within the band gap of $BiVO_4$ for the photocharged sample, while the dark sample does not show this increase in absorption. Just outside the band gap energy, between 475 and 700 nm, the photocharged sample shows a very distinct absorption feature.

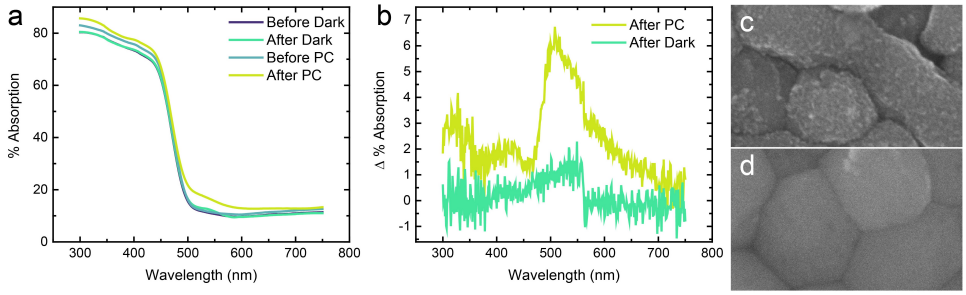

Figure 5.2. (a) UV-vis absorption spectra of a dark, before (purple) and after (green) the treatment and photocharged before (blue) and after (yellow) the treatment. (b) Difference spectra between before and after showing a defect-related feature in the PC sample. (c) HR-SEM image of PC-$BiVO_4$, showing small particles (white spots), finely dispersed over the $BiVO_4$ grains. (d) HR-SEM image of dark $BiVO_4$. Width of HR-SEM images is 520 nm.

The absorption increase inside the band gap could explain part of the improved OER activity of the PC-$BiVO_4$ sample, but cannot account for the observed 3-fold increase in the incident photon-to-current conversion efficiency (IPCE).[11] To determine whether the choice of buffer anion has any effect on this absorption feature, photocharging was performed in a phosphate buffer at pH 10. This treatment revealed a very similar improvement within the absorption spectra post photocharging (Figure D3a). When subtracting the spectrum of the before-PC from the after-PC spectrum (Figure 5.2b), a feature emerges that resembles either a surface plasmon resonance (SPR) mode with a peak in absorption around 520 nm or a defect-related absorption in PC-$BiVO_4$. The dark sample only has a minor increase in this region, but still shows a feature with a peak centred around 520 nm. Plasmonic features of vanadium oxide are only found in the infra-red region[28], and those for metallic vanadium are found in the UV region[29], whereas metallic bismuth nanoparticles in an oxide medium can give rise to plasmonic features around 500 nm.[20,30] However, the Bi 4f XPS spectra does not show any indication of the presence of metallic bismuth in the PC-BiVO4. Therefore, we tentatively assign this feature to a defect-related light absorption in PC-$BiVO_4$. In fact, such above bandgap optical features have been observed with some metal oxides[31,32]

and have often been attributed to defect-related light absorption, induced by surface oxygen vacancies. Therefore, the anion adsorption on the $BiVO_4$ surface upon photocharging could have introduced surface oxygen vacancies through surface restructuring. A high resolution scanning electron microscopy (HR-SEM) image of PC-$BiVO_4$ (Figure 5.2c) shows severe roughening of the surface on the nanoscale, compared to the dark and reference sample (Figure 5.2d and D3c, respectively). This surface roughening could be a result of the surface restructuring to accommodate the buffer anion adsorption.

X-ray Raman scattering To gain further insight into the structural and electronic changes induced by the photocharging treatment, the vanadium L_2 and L_3 edge and the oxygen K edge were probed using X-ray Raman scattering spectroscopy in near in situ conditions. X-ray absorption spectroscopy uses soft X-rays to probe light elements (<1 keV); however, these X-rays require ultra-high vacuum (UHV) conditions and are therefore less suitable for in situ studies. Instead, XRS allows the use of hard X-rays to probe elements with core-electron excitation energies in the soft X-ray regime i.e. lower than 1 keV. The use of hard X-rays leads to a bulk sensitive approach and can offer the possibility of working under operando conditions. In this work, we were able to study the $BiVO_4$ structure at room temperature and pressure and measure spectra immediately after the photocharging treatment was performed. Real operando conditions would greatly complicate the analysis of the O K edge spectrum since the electrolyte also contains oxygen, and instead this near in situ approach was adopted. A grazing incidence angle was maintained to avoid contributions from the oxygen-containing FTO substrate and to increase the footprint of the X-ray beam on the sample. The vanadium L_3 and L_2 edges and oxygen K edge can be probed within the same measurement since their absorption energies are very close. The electronic structure of the various $BiVO_4$ samples is obtained from XRS data by simulating the data with ab-initio based calculations.

The effect of photocharging on the electronic states in the conduction band of $BiVO_4$ was studied by comparing a photocharged (PC) sample and a dark sample to a reference sample. To try and preserve the operando state, the samples were not rinsed but only dried before being transferred to the XRS measurement chamber. All samples were fabricated according to the same procedure and XRS measurements were taken under identical settings. The XRS spectra of the three samples are shown together in Figure 5.3.

The region from 515 to 545 eV covers the core-electron excitations of interest, namely the vanadium L_2 and L_3 and oxygen K edges. For low transferred momenta, the orbital selection rule dictates $\Delta l = \pm 1$, where l is the azimuthal quantum number. Therefore, the vanadium L edge excitation results in a transition to the first available vanadium d orbital, and the oxygen K edge excitation transitions to the first unoccupied oxygen p orbital.

The XRS spectrum of the reference thin film $BiVO_4$ sample (dashed blue line in Figure 5.3) is discussed first. Four main peaks with shoulders to the left of the first three peaks are easily discernible. The first main peak between 515-520 eV corresponds to the V L_3 edge: the excitation from V $2p_{3/2}$ to conduction band V 3d states; the second main peak from 521 – 528 eV is the V L_2 edge: the excitation from $2p_{1/2}$ to the conduction band V 3d states.[33] The L_3 region consists of a main peak at 518 eV and a shoulder at 516 eV, which are the t_{2g} (main peak) and e_g (left shoulder) states of the VO_4 structure within the $BiVO_4$ lattice.[33,34] The V 3d orbitals are hybridised with the O 2p orbital. The L_2 edge is excited to the same (hybridised) V 3d t_{2g} and e_g states, however, this part of the spectrum is noisier than the V L_3 edge because the core-hole lifetime at the L_2 edge is shorter resulting in a broader spectrum. All excited state energies that are visible in Figure 5.3 are given in Table 5.1 with their corresponding orbital transitions. Overall, the XRS spectrum shows good agreement with soft X-ray XANES spectra of $BiVO_4$ in literature.[33,34]

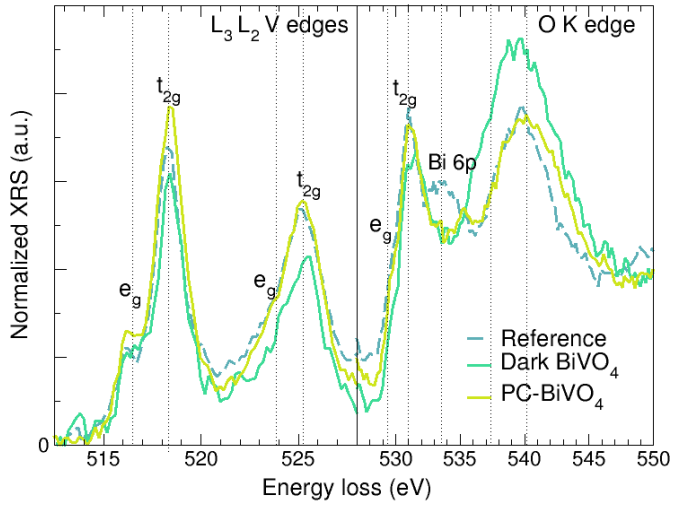

Figure 5.3. Normalised XRS spectra of the vanadium L_2, L_3 and the oxygen K edge region of a reference, dark and PC-$BiVO_4$ sample. The changing ratio of the O K edge peaks reveals a filling with electrons of the pre-edge peak (O 2p - V3d e_g/t_{2g}) for the dark sample.

The oxygen K excitations extend from 528 eV upwards, and consist of transitions from the occupied O 1s orbital close to the core of the oxygen atom, to the unoccupied O 2p states. A peak at 531 eV and its shoulder at 530 eV show the O 2p – V 3d hybridisation, and thus represent the same orbitals as the V L_2 and L_3 edge spectrum. Therefore, again these peaks are split into the e_g and t_{2g} states according to the tetrahedral crystal field splitting.[33] A second strong peak in the spectrum at 534 eV corresponds to anti-bonding π O 2p - Bi 6p states.[34,35] The final peak at 540 eV is the excitation to anti-bonding states

of σ character originating from the hybridisation of both V 4s and Bi 6s with O 2p.[33,36] Since the hybridisation between V and O is stronger than between Bi and O, the O K edge spectra mainly consist of V – O states.[36]

Table 5.1. All assigned peaks of the reference $BiVO_4$ sample as depicted in Figure 5.3.

Probed edge	Energy	Electronic transition
V L_3		**From $2p_{3/2}$ to unoccupied V 3d states**
	516 eV	to e_g V 3d – O 2p (d_{x2-y2}, d_{z2})
	518 eV	to t_{2g} V 3d – O 2p (d_{xy}, d_{xz}, d_{yz})
V L_2		**From $2p_{1/2}$ to unoccupied V 3d states**
	523 eV	to e_g V 3d – O 2p
	525 eV	to t_{2g} V 3d – O 2p
O K		**From O 1s to unoccupied O 2p states**
	530 eV	to e_g V 3d – O 2p
	532 eV	to t_{2g} V 3d – O 2p
	534 eV	to π* Bi 6p – O 2p
	540 eV	to σ* from V 4s and Bi 6s with O 2p

According to Cooper et al., the hybridised V 3d – O 2p orbitals are not simply split into the e_g and t_{2g} tetrahedral molecular orbitals, instead, three different V 3d contributions should be present in the spectrum.[34] This is due to the fact that the monoclinic scheelite (ms) form of $BiVO_4$ has lattice distortions causing the tetrahedral and dodecahedral symmetries to be broken. In fact, two separate V-O bond lengths and 4 separate Bi-O bond lengths are reported.[36] Therefore, the VO_4 has a C_2 symmetry, leading to triplet splitting of the V 3d orbitals. This is not easily discernible from the measured spectrum because of the lower resolution of XRS compared to standard soft X-ray XANES. However, it is important to realise that the broad peaks observed are composed of overlapping contributions of several orbitals.

XRS spectra of V^{4+} and V^{5+} reference samples were collected to help interpret the oxidation state of V in $BiVO_4$. These reference spectra were plotted together with those of reference, dark and photocharged $BiVO_4$ and are presented in Figure 5.4a. As is evident from the figure, the peaks of the V^{4+} reference sample (dark blue) are shifted to lower binding energies as compared to the peaks of the V^{5+} sample (purple). This is in very good agreement with the other studies in literature.[37,38] Another interesting aspect is that the peaks in the V L edge spectra for the reference, dark and PC-$BiVO_4$ are in between the V^{4+} and V^{5+} L edge reference spectra. From this, it can be concluded that the spray deposited $BiVO_4$ has a mix of V^{4+} and V^{5+} oxidation states. In an ideal $BiVO_4$ lattice, the vanadium species should have a 5+ oxidation state. However, it is very common to have intrinsic defects in the structure, in the form of oxygen vacancies. These oxygen vacancies are responsible for the n-type character of monoclinic $BiVO_4$. Due to these

oxygen vacancies, to maintain charge neutrality, some vanadium species in the $BiVO_4$ lattice could exist in the 4+ oxidation state. Rossell et al.[39] quantified the vanadium oxidation state in monoclinic $BiVO_4$ using energy-loss spectroscopy and suggested that the surface vanadium ions predominantly exist in a ~ 4+ oxidation state, due to the presence of a significant amount of oxygen vacancies.

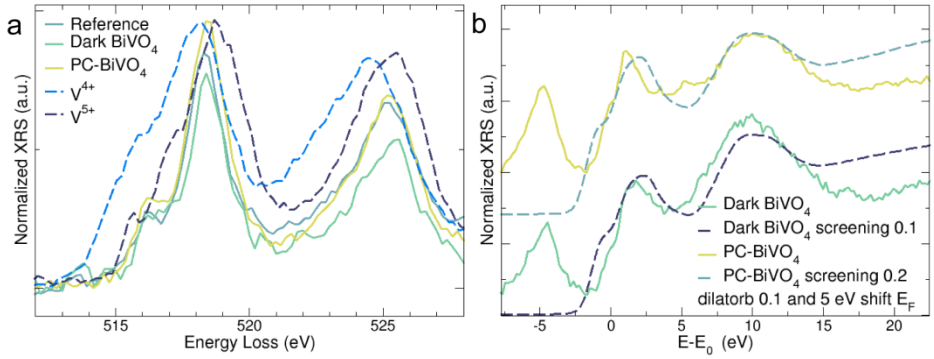

Figure 5.4. (a) XRS spectra of the vanadium oxides (V_2O_4 and V_2O_5) are presented together with the reference, dark and PC-$BiVO_4$ to show the effect of changing V oxidation state on the peak position in the V L_2 and L_3 edge spectra. (b) The O K edge spectra of the dark and PC sample are overlaid with ab initio simulations including the semi-empirical *dilatorb* and *screening* parameters.

To better understand these results, it is important to consider the penetration depth of the performed XRS measurements. Due to the grazing incidence angle of 0.5°, only the first 60 nm are probed. Additionally, the spray deposited $BiVO_4$ is highly nanostructured and hence has a high surface-to-volume ratio. Therefore, the obtained vanadium L edge spectra for the reference, dark and photocharged samples could be an average of the surface and bulk oxidation state of vanadium who fall between the 4+ and 5+ oxidation state. These results are in alignment with the XRD diffractograms that show a strong resemblance between the reference and photocharged samples, both having monoclinic scheelite $BiVO_4$ features (Figure D4).[40] The reference, dark and photocharged $BiVO_4$ have similar vanadium L edge peak positions. However, the dark and PC-$BiVO_4$ show a slightly different ratio in intensity between the V L_3 and L_2 edges compared to the reference spectra. A multiplet analysis was performed to predict the shape of the V L edge spectra for a vanadium species in its V^{4+} and V^{5+} oxidation state, in a hypothetical bismuth-vanadium oxide compound. These results are shown in Figure D5 and suggest that there could be a decrease in the oxidation state of vanadium, with an increase in the L_3/L_2 peak ratio. The V L_3/L_2 peak ratio is indeed higher for the dark and PC-$BiVO_4$ compared to the reference (Table D3) and would suggest a decrease in the oxidation state of vanadium, possibly from the creation of additional oxygen vacancies at the surface. This would be in agreement with the above bandgap absorption

feature seen in the absorption spectra of the PC-$BiVO_4$ and with the shift in the V 2p XPS spectrum. However, the low resolution of the XRS technique coupled with the surface and bulk averaging of the XRS technique, makes this comparison difficult. Screening of V 2p XPS spectra by the surface adsorbed layer also makes the comparison of the V 2p XPS spectra difficult. Additional experiments will be needed to study and quantify the vanadium oxidation state change in the dark and the photocharged sample, which is out of the scope of this work.

A disappearance of the O 2p - Bi 6p peak at 534 eV was observed for both the PC sample and the dark sample. As mentioned previously, the Bi – O hybridisation is not very strong, therefore a small change in the electronic structure can make the Bi 6p signal less visible, this appears to be the case for the dark sample. Bismuth borate withdraws bismuth from $BiVO_4$, which leads to the reduction of the O 2p – Bi 6p signal in the XRS spectrum of the photocharged $BiVO_4$. The broadening of the mixed metal sp – O 2p peak implies the existence of multiple orbitals that partly overlap in energy. This can be caused by the presence of multiple V oxidation states that all have molecular orbitals of slightly different energy.

The main difference between the dark and PC-$BiVO_4$ XRS spectra is the filling with electrons of the V 3d states of the dark sample, as observed from a difference in peak height ratio between the pre-edge peak (V 3d – O 2p) and the main peak (mixed metal sp – O 2p) in the O K edge spectrum. This lowering of the pre-edge peak implies a filling of the d states, resulting in a higher concentration of electrons for the dark sample compared to the reference and photocharged samples. The reason for this difference is not immediately obvious, so to further elucidate and quantify the influence of the photocharging treatment on the electronic structure of $BiVO_4$, ab initio simulations at the O K edge were performed with the FDMNES program package. The calculated spectra were compared to the experimentally obtained XRS spectra (the input parameter files of the calculations are shown in appendix D). In order to simulate the peak height ratios observed in the experimental XRS spectra, two semi-empirical parameters, the *dilatorb* and *screening* parameter were used in the calculations. The *dilatorb* and *screening* parameters allow the ability to tune the height of the pre-edge peaks and their position with respect to the main edge. Moreover, the *dilatorb* parameter allows the ability to consider the degree of ionicity of oxygen in the lattice structure by modifying the valence orbitals. Modifying this parameter means either dilating or contracting the valence orbitals, which is a necessary procedure when modelling anions with this package since the default is fully covalent, not considering the ionic character of oxygen.[41] Anions have a more negative charge and are larger than their covalent radius because of the extra electrons that the anions take from the cations. The effect of changing the *dilatorb* parameter is shown in Figure D6.

The *screening* parameter is used to simulate a not fully screened core-hole in the absorbing atom, meaning that part of the electron charge in the conduction band is missing. When the total excited electron is present in the conduction band, no charge is missing and the core-hole is considered fully screened. The screening parameter generally points to a correlation effect caused by the presence of the excited 3d electrons that hinder the screening process. In this respect, the screening value is an indication of the filling with electrons of the conduction band. However, oxygen electrons can behave unexpectedly to the removal of electrons, and it is therefore not always possible to predict the pattern in the O K edge spectra as a function of electron depletion. Instead, the *screening* parameter can help making the trends of the spectra quantifiable. The effect of changing the *screening* parameter is shown in Figure D7.If the effects of the *dilatorb* and the *screening* value are now combined, it is possible to effectively simulate the XRS spectra. The best fitting simulations are shown in Figure 5.4 and D6. The reference spectrum (Figure D8) was fitted with a *dilatorb* value of 0.1 and no *screening* potential. The dark sample is fitted with a *screening* value of 0.1 and the *dilatorb* set to 0.1. The photocharged sample on the other hand is fitted with a *screening* parameter of 0.2 and a *dilatorb* value of 0.1. The default value for the *screening* parameter is 0 in the FDMNES software, so the lack of a defined *screening* value in the reference sample should be understood as full *screening*. The trend in the *screening* between the different samples is therefore: reference > dark > photocharged $BiVO_4$.

The difference in *screening* value between the dark and PC spectra can be explained by the photocharged sample having less electrons in the conduction band than the dark sample in the area measured by XRS, which also explains the pre-edge filling of the dark sample observed in Figure 5.3. The *screening* value of 0.2 for PC-$BiVO_4$ is significantly higher with respect to the value of 0 that was used for the reference sample, showing strong structural changes in $BiVO_4$ as a result of the photocharging treatment. A higher *screening* value also indicates a shift to a lower Fermi level since less electrons are present in the conduction band. Less electrons for the photocharged sample might seem counterintuitive, but in fact it is a consequence of improved band bending induced by the heterojunction between $BiVO_4$ and the surface formed bismuth borate layer. The fact that electrons are driven away from the surface by band bending is responsible for the strong suppression of surface recombination induced by the photocharging treatment. The decrease in Fermi level is also introduced in the simulations. The dark sample also has less electrons compared to the reference sample and a lower Fermi level, but the changes are smaller as compared to the photocharged sample.

5.4 Discussion

The XPS analysis confirmed the formation of a bismuth borate surface layer on $BiVO_4$, upon photocharging. The shifts of the core level XPS spectra, to lower binding energies upon photocharging, suggested that this borate surface layer induced an upward band bending within $BiVO_4$ (Figure 5.5a). Similar conclusions could be drawn in the case of the dark samples. After 18 h under open circuit conditions in the dark, the dark sample has an OH coverage that initially improves the photo-electrochemical performance of the sample (Figure D9). This improvement is, however, smaller than the PEC improvement of the PC samples and is not maintained over time because the OH species are removed from the surface during water oxidation. Both the dark and photocharged samples demonstrated a higher open circuit potential in the dark than the reference sample (Figure D2), resulting in a Fermi level closer to the conduction band in the bulk, as depicted in Figure 5.5a. To determine whether the bismuth borate and OH surface layers had any effect on the bulk structure of $BiVO_4$, both UV-Vis and XRS measurements were performed. The UV-Vis spectra revealed a change in absorption post photocharging, with the formation of an above bandgap absorption feature. This feature was attributed to a defect-related absorption, possibly from the creation of surface oxygen vacancies.

To gain a deeper understanding of the electronic effect of the bismuth borate layer on $BiVO_4$, XRS measurements were performed. These results showed that the hybridised Bi 6p – O 2p orbital disappeared, which corresponds well with the formation of a Bi surface layer. In addition, the ab-initio simulations of the O K edge spectra revealed a decrease in the Fermi level of the PC-$BiVO_4$. This can be explained by band bending induced by the surface borate layer. Bismuth borate has a larger band gap than $BiVO_4$ and according to the valence band spectra (Figure 5.1d) its valence band lies closer to the Fermi level than the valence band of $BiVO_4$. This means that the heterojunction of $BiVO_4$ and bismuth borate will create strong band bending and a significant space charge region (SCR) of several tens of nanometres (Figure 5.5a).[42,43] The SCR coincides with the region that is probed by XRS. Since the band bending forces electrons toward the back contact, the SCR will contain fewer electrons than in the case of a flat band situation. The monolayer of OH on the surface of the dark $BiVO_4$ sample has a similar band bending effect that directs the electrons toward the back contact, away from the surface.

The XRS results from this work suggest that there is a severe alteration in the surface electronic structure when $BiVO_4$ comes in contact with an electrolyte, even without illumination. This is also supported by the changes visible in the data obtained from XPS and HR-SEM. The initiator of this surface restructuring could be the surface adsorption of electrolyte anionic species, borate in the case of the PC-$BiVO_4$ and hydroxide in the case of dark $BiVO_4$. The heterojunctions formed as a result of this surface adsorption

improve the charge separation close to the surface, and thus suppress surface recombination. Since other metal oxides[13,14,16] were also shown to photocharge like $BiVO_4$, these findings could be generalised.

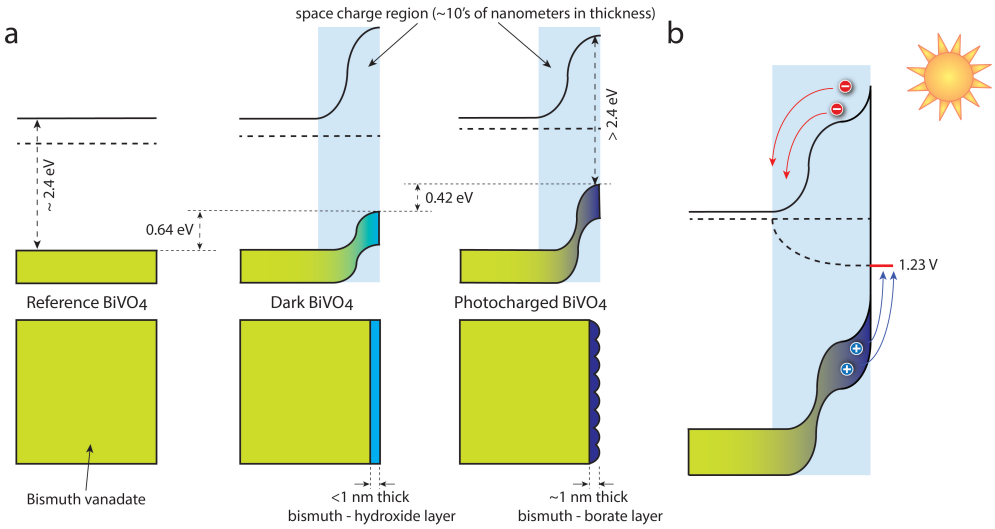

Figure 5.5. The effect of photocharging on the band gap region and the Fermi level of $BiVO_4$. (a) The hydroxide (dark sample) and bismuth borate (PC sample) surface layers have a valence band closer to the Fermi level, introducing band bending at the surface. The band bending directs electrons towards the bulk of $BiVO_4$, leading to a reduced electron concentration in the space charge region for PC-$BiVO_4$. Note that the bulk band gap size is not altered by the PC treatment (Figure D10). (b) The effect of photocharging on a $BiVO_4$ photoanode in contact with an electrolyte under illumination. The additional band bending improves the charge separation, leading to the unrivalled PEC properties of PC-$BiVO_4$.

Additionally, this time-dependent surface layer formation shows that the metal oxide/electrolyte interface is very dynamic. Reversibility of the photocharging effect[10] in the dark could be explained by the desorption of this buffer anion surface layer under dark conditions, which was also shown by Favaro et al.[17] The dynamic nature of the metal oxide/electrolyte interface makes it difficult for the photoanode material to be stable for long-term operation. The constant switching between the dark and light conditions, as in a practical case where intermittent sunlight drives the reaction, would imply constant surface restructuring of the photoanode material. Some material from the surface could be lost in each of these restructuring steps, in addition to other corrosion mechanisms occurring at the surface of a photoanode material.

It is important to emphasise that this surface layer formation, in the dark and under illumination, from the electrolyte anionic species has been "ever-present" in metal oxide photoanodes. This work highlights that the choice of electrolyte/buffer solutions needs

to be considered when making comparisons of PEC performance of different systems with the same metal oxide semiconductor. The surface layer formed would be different with different electrolytes and hence the resultant heterojunction would be different as well. However, the importance or the effect of the electrolyte has been largely unnoticed in the PEC research field when analysing material surfaces after photo-electrochemical measurements. This current study is a strong indicator that the effect of surface adsorption of electrolyte anionic species can have serious implications on PEC measurements and should be given due regard for future works in the field.

5.5 Conclusions

The photocharging treatment of $BiVO_4$ was studied using a sequence of XPS, UV-Vis and XRS techniques. The XPS studies revealed the formation of a surface borate layer on the $BiVO_4$ surface, upon illumination in open circuit conditions. The borate anion from the electrolyte covalently bonded with the bismuth ions in the BiVO4, resulting in a BiVO4/bismuth borate heterojunction near the surface. This heterojunction resulted in improved band bending near the surface, improving the charge separation and suppressing the surface recombination of charge carriers. The improved band bending, as a result of the heterojunction, explains the enhancement in the PEC performance of photocharged $BiVO_4$. In a similar manner, a $BiVO_4$ sample kept under open circuit conditions in the dark formed an OH layer at the surface, leading to a relatively smaller degree of band bending and a short-lived PEC performance enhancement.

The UV-Vis studies showed the formation of a new absorption feature, outside the bandgap of $BiVO_4$, upon photocharging. This feature was attributed to defect-related absorption, resulting from the surface restructuring during photocharging. This surface restructuring during photocharging was confirmed using HR-SEM images. A combination of XRS studies and ab-initio simulations on the oxygen K edge spectra revealed a decrease in the electron occupancy in the space charge region of the dark and PC-$BiVO_4$, confirming the improvement in band bending after the dark and photocharging treatment. Additionally, the XPS, UV-Vis and XRS measurements indicated a decrease in the oxidation state of the surface vanadium species due to the anion adsorption. Further experiments are required to quantify this change.

A strong agreement was found between the XRS spectra obtained in this work and soft X-ray XANES spectra from others, indicating that XRS is a very powerful tool to study semiconductors in (near) in-situ conditions with a larger probing depth than allowed by soft X-ray techniques. The dynamic nature of the metal oxide/electrolyte interface will have strong implications on the long-term stability of metal oxide photoanodes. The effect of surface adsorption of electrolyte anionic species on the surface structure of metal oxide photoelectrodes is often overlooked within the PEC research field. Our results show that this time-dependent surface adsorption of electrolyte anionic species

on the metal oxide photoanode surface plays an important role in defining the electronic and catalytic properties of a photoanode. Anionic adsorption was shown to form a heterojunction at the surface which improved charge separation and suppressed surface recombination. The effect of the electrolyte on the metal oxide photoanode surface and the time-scale of the surface adsorption of these anions cannot be ignored, and hence should be taken into consideration while performing analyses and gaining mechanistic understanding of reactions on metal oxide photoanodes surfaces.

5.6 References

(1) Alexander, B. D.; Kulesza, P. J.; Rutkowska, I.; Solarska, R.; Augustynski, J. Metal Oxide Photoanodes for Solar Hydrogen Production. J. Mater. Chem. 2008, 18, 2298–2303.

(2) Han, H. S.; Shin, S.; Kim, D. H.; Park, I. J.; Kim, J. S.; Huang, P. S.; Lee, J. K.; Cho, I. S.; Zheng, X. Boosting the Solar Water Oxidation Performance of a BiVO4 Photoanode by Crystallographic Orientation Control. Energy Environ. Sci. 2018, 11, 1299–1306.

(3) Abdi, F. F.; Han, L.; Smets, A. H. M.; Zeman, M.; Dam, B.; Van De Krol, R. Efficient Solar Water Splitting by Enhanced Charge Separation in a Bismuth Vanadate-Silicon Tandem Photoelectrode. Nat. Commun. 2013, 4 (2195).

(4) Sharp, I. D.; Cooper, J. K.; Toma, F. M.; Buonsanti, R. Bismuth Vanadate as a Platform for Accelerating Discovery and Development of Complex Transition-Metal Oxide Photoanodes. ACS Energy Lett. 2017, 2, 139–150.

(5) Pilli, S. K.; Furtak, T. E.; Brown, L. D.; Deutsch, T. G.; Turner, J. A.; Herring, A. M. Cobalt-Phosphate (Co-Pi) Catalyst Modified Mo-Doped BiVO4 Photoelectrodes for Solar Water Oxidation. Energy Environ. Sci. 2011, 4, 5028–5034.

(6) Zhong, D. K.; Choi, S.; Gamelin, D. R. Near-Complete Suppression of Surface Recombination in Solar Photoelectrolysis by "Co-Pi" Catalyst-Modified W:BiVO4. J. Am. Chem. Soc. 2011, 133, 18370–18377.

(7) Lee, D.; Kvit, A.; Choi, K. S. Enabling Solar Water Oxidation by BiVO4 Photoanodes in Basic Media. Chem. Mater. 2018, 30, 4704–4712.

(8) Zachäus, C.; Abdi, F. F.; Peter, L. M.; Van De Krol, R. Photocurrent of BiVO4 Is Limited by Surface Recombination, Not Surface Catalysis. Chem. Sci. 2017, 8, 3712–3719.

(9) Trotochaud, L.; Mills, T. J.; Boettcher, S. W. An Optocatalytic Model for Semiconductor-Catalyst Water-Splitting Photoelectrodes Based on in Situ Optical Measurements on Operational Catalysts. J. Phys. Chem. Lett. 2013, 4, 931–935.

(10) Trześniewski, B. J.; Smith, W. A. Photocharged BiVO4 Photoanodes for Improved Solar Water Splitting. J. Mater. Chem. A 2016, 4, 2919–2926.

(11) Trześniewski, B. J.; Digdaya, I. A.; Nagaki, T.; Ravishankar, S.; Herraiz-Cardona, I.; Vermaas, D. A.; Longo, A.; Gimenez, S.; Smith, W. A. Near-Complete

Suppression of Surface Losses and Total Internal Quantum Efficiency in BiVO 4 Photoanodes. Energy Environ. Sci. 2017, 10, 1517–1529.

(12) Liu, E. Y.; Thorne, J. E.; He, Y.; Wang, D. Understanding Photocharging Effects on Bismuth Vanadate. ACS Appl. Mater. Interfaces 2017, 9, 22083–22087.

(13) Breuhaus-Alvarez, A. G.; Dimeglio, J. L.; Cooper, J. J.; Lhermitte, C. R.; Bartlett, B. M. Kinetics and Faradaic Efficiency of Oxygen Evolution on Reduced HxWO3 Photoelectrodes. J. Phys. Chem. C 2019, 123, 1142–1150.

(14) Venugopal, A.; Smith, W. A. Light Induced Formation of a Surface Hetero-Junction in Photocharged CuWO4 Photoanodes. Faraday Discuss. 2019, 215, 175–191.

(15) Xie, J.; Yang, P.; Liang, X.; Xiong, J. Self-Improvement of Ti:Fe2O3 Photoanodes: Photoelectrocatalysis Improvement after Long-Term Stability Testing in Alkaline Electrolyte. ACS Appl. Energy Mater. 2018, 1, 2769–2775.

(16) Deng, J.; Lv, X.; Zhong, J. Photocharged Fe2TiO5/Fe2O3 Photoanode for Enhanced Photoelectrochemical Water Oxidation. J. Phys. Chem. C 2018, 122, 29268–29273.

(17) Favaro, M.; Abdi, F. F.; Lamers, M.; Crumlin, E. J.; Liu, Z.; van de Krol, R.; Starr, D. E. Light-Induced Surface Reactions at the Bismuth Vanadate/Potassium Phosphate Interface. J. Phys. Chem. B 2018, 122, 801–809.

(18) Abdi, F. F.; Firet, N.; van de Krol, R. Efficient BiVO4 Thin Film Photoanodes Modified with Cobalt Phosphate Catalyst and W-Doping. ChemCatChem 2013, 5, 490–496.

(19) Huotari, S.; Sahle, C. J.; Henriquet, C.; Al-Zein, A.; Martel, K.; Simonelli, L.; Verbeni, R.; Gonzalez, H.; Lagier, M. C.; Ponchut, C.; et al. A Large-Solid-Angle X-Ray Raman Scattering Spectrometer at ID20 of the European Synchrotron Radiation Facility. J. Synchrotron Radiat. 2017, 24, 521–530.

(20) Singh, S. P.; Karmakar, B. Bismuth Oxide and Bismuth Oxide Doped Glasses for Optical and Photonic Applications. In Bismuth: Characteristics, Production and Applications. Materials Science and Technologies; New York, 2012; p Chapter 9.

(21) Sahle, C. J.; Mirone, A.; Niskanen, J.; Inkinen, J.; Krisch, M.; Huotari, S. Planning, Performing and Analyzing X-Ray Raman Scattering Experiments. J. Synchrotron Radiat. 2015, 22, 400–409.

(22) Joly, Y. X-Ray Absorption near-Edge Structure Calculations beyond the Muffin-Tin Approximation. Phys. Rev. B 2001, 63, 125120 1-10.

(23) Joly, Y.; Cavallari, C.; Guda, S. A.; Sahle, C. J. Full-Potential Simulation of X-Ray Raman Scattering Spectroscopy. J. Chem. Theory Comput. 2017, 13, 2172–2177.

(24) Retegan, M. Mretegan/Crispy v0.7.1. Zenobo. October 8, 2018.

(25) Oprea, B.; Radu, T.; Simon, S. XPS Investigation of Atomic Environment Changes on Surface of B2O3-Bi2O3 Glasses. J. Non. Cryst. Solids 2013, 379, 35–39.

(26) Bajaj, A.; Khanna, A.; Chen, B.; Longstaffe, J. G.; Zwanziger, U. W.; Zwanziger, J. W.; Gómez, Y.; González, F. Structural Investigation of Bismuth Borate Glasses and Crystalline Phases. J. Non. Cryst. Solids 2009, 355, 45–53.

(27) Hermans, Y.; Murcia-López, S.; Klein, A.; Morante, J. R.; van de Krol, R.; Andreu, T.; TOUPANCE, T.; Jaegermann, W. Analysis of the Interfacial Characteristics of BiVO4/Metal Oxide Heterostructures and Its Implication on Their Junction Properties. Phys. Chem. Chem. Phys. 2019, 21, 5086–5096.

(28) Feldman, L. C.; Boatner, L. A.; López, R.; Rini, M.; Haynes, T. E.; Cavalleri, A.; Haglund, R. F.; Schoenlein, R. W. Photoinduced Phase Transition in VO2 Nanocrystals: Ultrafast Control of Surface-Plasmon Resonance. Opt. Lett. 2005, 30, 558–560.

(29) Schubert, W. K.; Wolf, E. L. Electron-Energy-Loss Spectra of Vanadium, Niobium, Molybdenum, and Tantalum. Phys. Rev. B 1979, 20, 1855–1862.

(30) Toudert, J.; Serna, R.; Jiménez De Castro, M. Exploring the Optical Potential of Nano-Bismuth: Tunable Surface Plasmon Resonances in the near Ultraviolet-to-near Infrared Range. J. Phys. Chem. C 2012, 116, 20530–20539.

(31) Wang, L.; Tsang, C. S.; Liu, W.; Zhang, X.; Zhang, K.; Ha, E.; Kwok, W. M.; Park, J. H.; Suk Lee, L. Y.; Wong, K. Y. Disordered Layers on WO 3 Nanoparticles Enable Photochemical Generation of Hydrogen from Water. J. Mater. Chem. A 2019, 7, 221–227.

(32) Wang, S.; Chen, P.; Yun, J. H.; Hu, Y.; Wang, L. An Electrochemically Treated BiVO4 Photoanode for Efficient Photoelectrochemical Water Splitting. Angew. Chemie - Int. Ed. 2017, 56, 8500–8504.

(33) Jovic, V.; Laverock, J.; Rettie, A. J. E.; Zhou, J.-S.; Mullins, C. B.; Singh, V. R.; Lamoureux, B.; Wilson, D.; Su, T.-Y.; Jovic, B.; et al. Soft X-Ray Spectroscopic

Studies of the Electronic Structure of M:BiVO 4 (M = Mo, W) Single Crystals. J. Mater. Chem. A 2015, 3, 23743–23753.

(34) Cooper, J. K.; Gul, S.; Toma, F. M.; Chen, L.; Glans, P. A.; Guo, J.; Ager, J. W.; Yano, J.; Sharp, I. D. Electronic Structure of Monoclinic BiVO4. Chem. Mater. 2014, 26, 5365–5373.

(35) Jovic, V.; Rettie, A. J. E.; Singh, V. R.; Zhou, J.; Lamoureux, B.; Buddie Mullins, C.; Bluhm, H.; Laverock, J.; Smith, K. E. A Soft X-Ray Spectroscopic Perspective of Electron Localization and Transport in Tungsten Doped Bismuth Vanadate Single Crystals. Phys. Chem. Chem. Phys. 2016, 18 (46), 31958–31965.

(36) Zhao, Z.; Li, Z.; Zou, Z. Electronic Structure and Optical Properties of Monoclinic Clinobisvanite BiVO4. Phys. Chem. Chem. Phys. 2011, 13, 4746–4753.

(37) Nie, K.; Kashtanov, S.; Wei, Y.; Liu, Y. S.; Zhang, H.; Kapilashrami, M.; Ye, Y.; Glans, P. A.; Zhong, J.; Vayssieres, L.; et al. Atomic-Scale Understanding of the Electronic Structure-Crystal Facets Synergy of Nanopyramidal CoPi/BiVO4 Hybrid Photocatalyst for Efficient Solar Water Oxidation. Nano Energy 2018, 53, 483–491.

(38) Lin, X. W.; Wang, Y. Y.; Dravid, V. P.; Michalakos, P. M.; Kung, M. C. Valence States and Hybridization in Vanadium Oxide Systems Investigated by Transmission Electron-Energy-Loss Spectroscopy. Phys. Rev. B 1993, 47, 3477–3481.

(39) Rossell, M. D.; Agrawal, P.; Borgschulte, A.; Hébert, C.; Passerone, D.; Erni, R. Direct Evidence of Surface Reduction in Monoclinic BiVO 4. Chem. Mater. 2015, 27, 3593–3600.

(40) Tokunaga, S.; Kato, H.; Kudo, A. Selective Preparation of Monoclinic and Tetragonal BiVO4 with Scheelite Structure and Their Photocatalytic Properties. Chem. Mater. 2001, 13, 4624–4628.

(41) Joly, Y.; Cabaret, D.; Renevier, H.; Natoli, C. R. Electron Population Analysis by Full-Potential X-Ray Absorption Simulations. Phys. Rev. Lett. 1999, 82, 2398–2401.

(42) Peter, L. M.; Gurudayal; Wong, L. H.; Abdi, F. F. Understanding the Role of Nanostructuring in Photoelectrode Performance for Light-Driven Water Splitting. J. Electroanal. Chem. 2018, 819, 447–458.

(43) van der Krol, R.; Grätzel, M. Photoelectrochemical Hydrogen Production, 1st ed.; Springer US: New York, 2012.

Appendix D

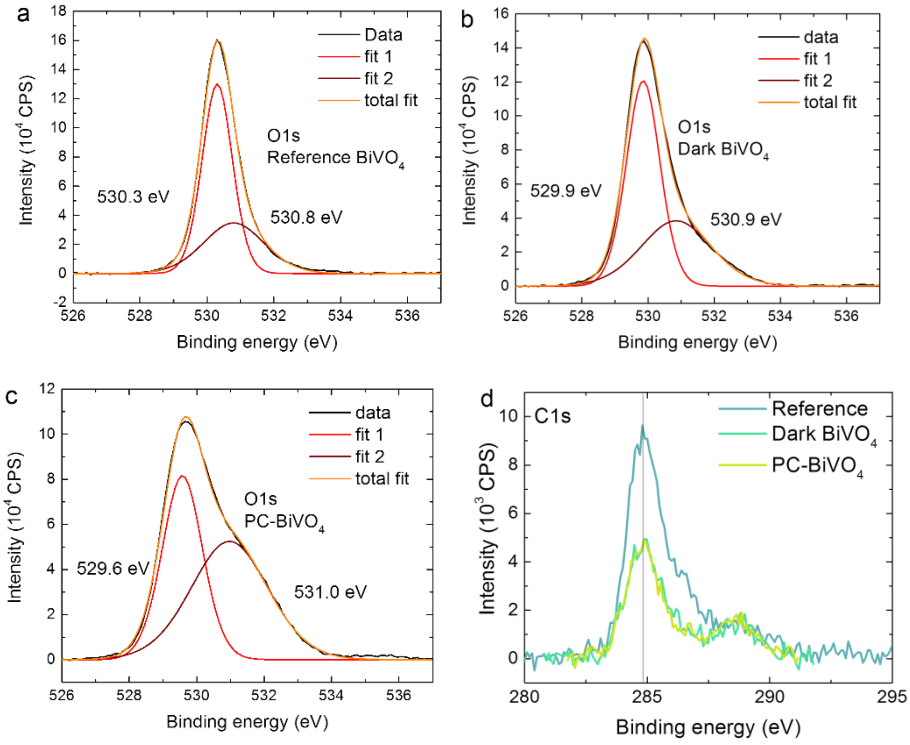

Figure D1. Deconvoluted O 1s XPS spectra for (a) reference $BiVO_4$, (b) dark $BiVO_4$ and (c) PC-$BiVO_4$. (d) C1s spectra showing the C correction to 284.8 eV.

Table D1. Gaussian fits of Bi 4f spectra from Figure 5.1a. All values are given in eV.

		Ref	Dark	PC
Centre	Bi $4f_{5/2}$	164.82	164.34	163.97
FWHM	Bi $4f_{5/2}$	1.05	1.07	1.27
Centre	Bi $4f_{7/2}$	159.52	159.04	158.67
FWHM	Bi $4f_{7/2}$	1.04	1.07	1.26

Table D2. Gaussian peak fits of core level spectra and valence band onset values from Figure 5.1. All values are given in eV.

	Ref	Dark	Ref-Dark (Dark shift)	PC	Ref-PC (PC shift)
O 1s main	530.29	529.85	0.44	529.57	0.72
O 1s shoulder	530.8	530.85	-0.05	530.97	-0.17
V 2p3/2	517.21	516.67	0.54	516.16	1.05
Bi 4f5/2	164.82	164.34	0.48	163.97	0.85
VB onset	1.94	1.42	0.52	1.06	0.88

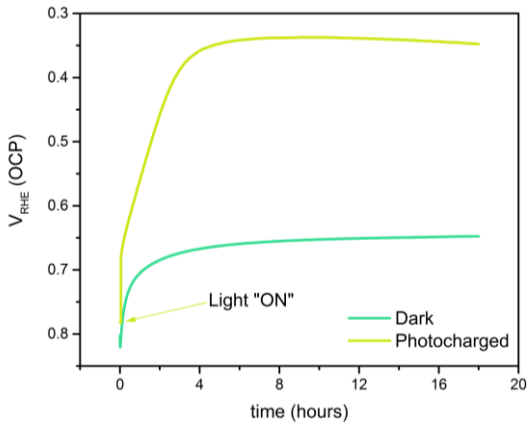

Figure D2. Plot of OCP vs time for dark and PC-$BiVO_4$.

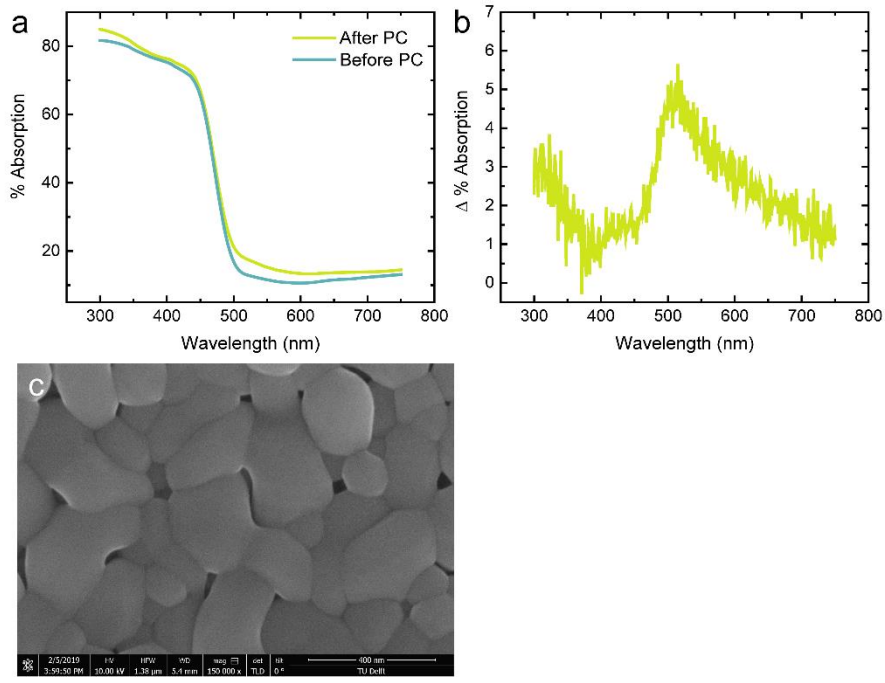

Figure D3. (a) UV-vis absorption and (b) difference spectra of a before and after photocharging sample in phosphate buffer. After photocharging in phosphate buffer at pH 10, the PC sample also displays a plasmonic feature at 520 nm, indicating the optic response stems from the $BiVO_4$, rather than the electrolyte. (c) HR-SEM images of reference $BiVO_4$, not displaying surface roughening. Scale bar is 400 nm.

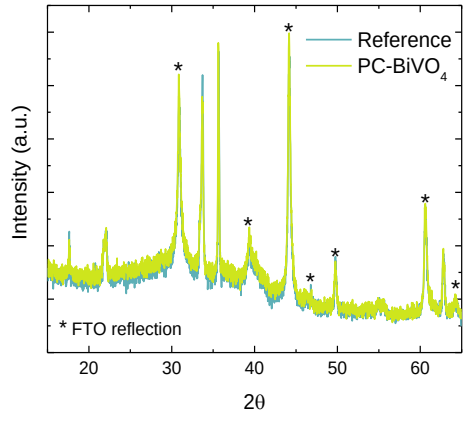

Figure D4. X-ray diffraction patterns of a reference and PC-$BiVO_4$ sample. The peak at 17.5° 2θ only exists in monoclinic scheelite. Note that these XRD patterns were recorded using a cobalt (λ=1.7903 Å) radiation source, changing the XRD pattern compared to more commonly used copper (λ=1.5406 Å) sources.

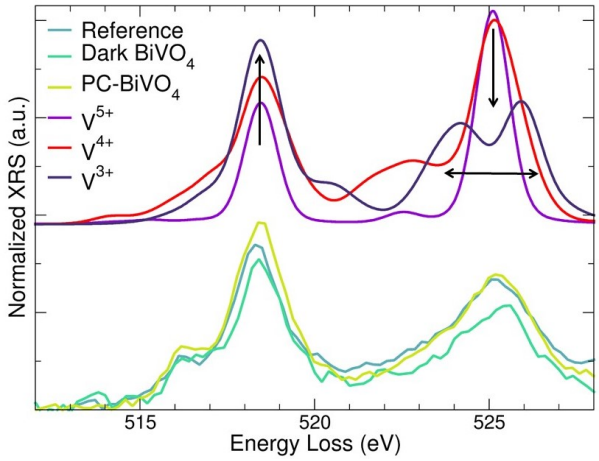

Figure D5. A multiplet analysis of the vanadium L_3 and L_2 edge reveals the oxidation state of vanadium in the first 60 nm of $BiVO_4$ to be lower than 5+. Arrows indicate trends: the L_3 increases in height and the L_2 edge decreases and broadens when the oxidation state decreases. Note: analysis was normalised with respect to E_0. Therefore the shift in energy as a function of oxidation state cannot be derived from the simulated spectra.

Table D3. Heights and intensity ratios of the XRS spectra given in Figure 5.4a.

	V^{5+}	V^{4+}	Ref	Dark	PC
L_3	1.9	1.9	1.7	1.5	1.9
L_2	1.7	1.7	1.3	1.1	1.4
L_3/L_2	1.1	1.2	1.3	1.4	1.4

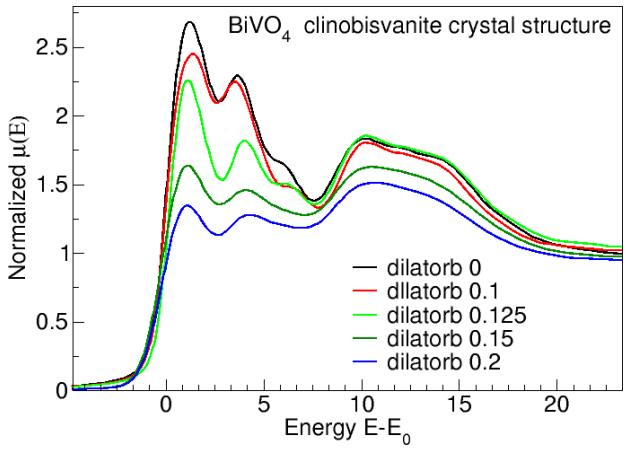

Figure D6. The effect of increasing the dilatorb parameter on the $BiVO_4$ crystal structure.

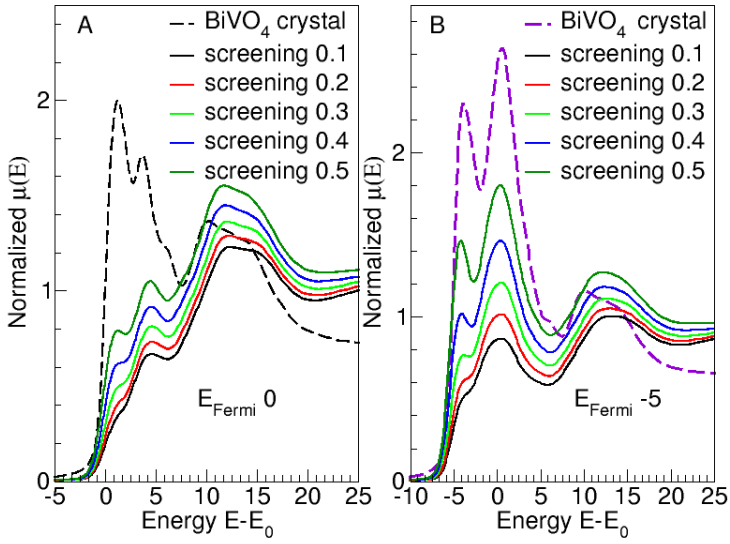

Figure D7. Simulated O K edge spectra. The effect of changing the screening parameter on the $BiVO_4$ crystal structure for (a) a standard and (b) a 5 eV shifted Fermi level case.

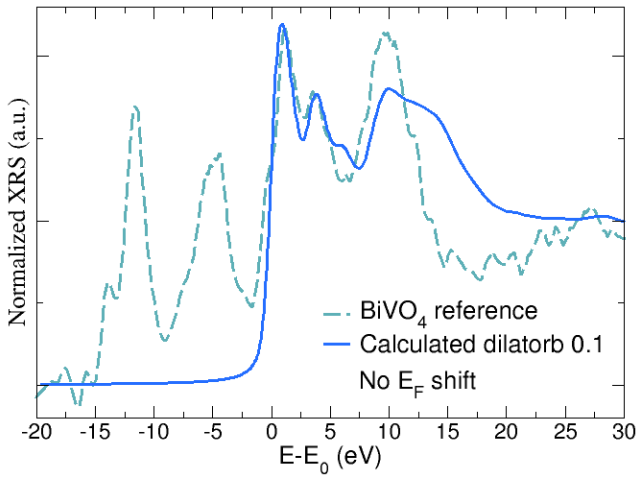

Figure D8. Simulated O K edge spectra overlaid on XRS reference $BiVO_4$ spectrum. Reference $BiVO_4$ was simulated with a dilatorb value of 0.1, no screening parameter and no Fermi level shift.

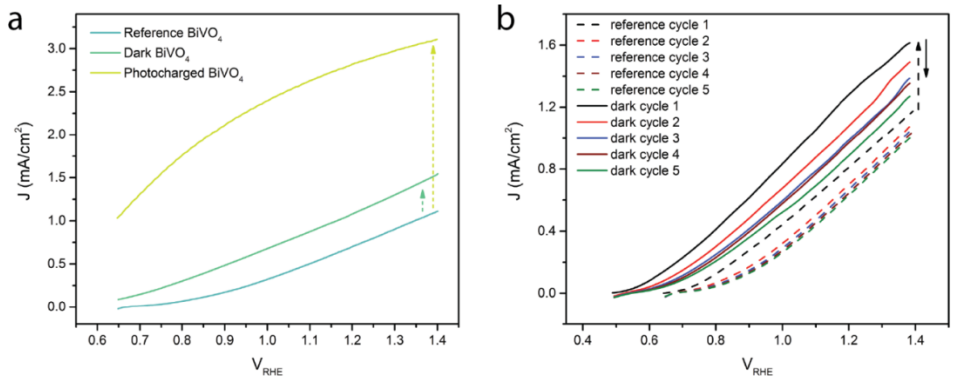

Figure D9. (a) Plot showing the anodic scans of the CV's of the reference, dark and PC-$BiVO_4$ (b) Improved performance of the $BiVO_4$ sample post dark treatment and the sudden decay of the performance once the surface adsorbed OH species is consumed for the water oxidation reaction.

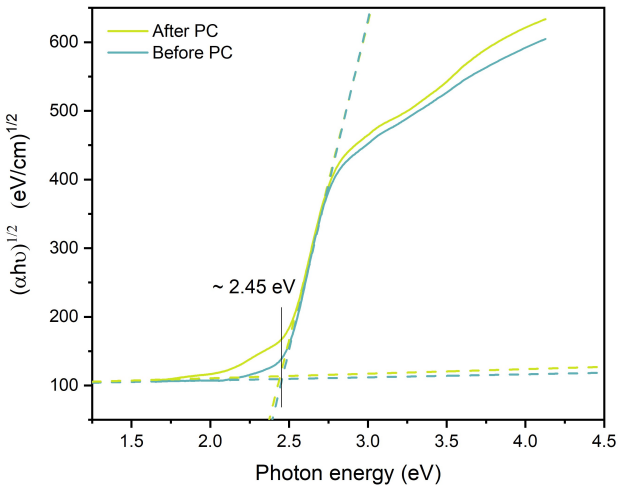

Figure D10. Tauc plot of the absorbance spectra in Figure 5.2a.

The absorption coefficient (α) was calculated using equation D1,

$$\alpha = 2.303\ A/t \qquad \text{D1}$$

where A is the absorbance and t is the thickness of the $BiVO_4$ sample. A thickness of 200 nm of deposited $BiVO_4$ was used for the calculations. The absorbance was calculated from the measured transmittance (%T) data using equation D2,

$$A = 2 - \log(\%T) \qquad \text{D2}$$

The bandgap of the $BiVO_4$ was determined using the relation presented by Tauc and Davis and Mott[1,2],

$$(\alpha h\nu)^{1/n} \propto (h\nu - E_g) \qquad \text{D3}$$

Where n can take different values depending on the type of bandgap. $BiVO_4$ is an indirect bandgap semiconductor[3] and hence n=2 was used to make the calculation from Figure D10. E_g in equation D3 is the bandgap and is obtained by extrapolation to the baseline, as in Figure D10.

```
! Fdmnes indata file
! Calculation for the O K edge in BiVO4
! Finite difference method calculation with convolution

 Filout
  ./bvo4_cry_o_dlorb_0.2_sp_scr_0.1_new

 Range                    ! Energy range of calculation (eV)
-20. 0.2 -5 0.05 0. 0.1 5 0.2 10. .5 40. 1 80. ! first energy, step, intermediary energy, step ..., last energy

 Radius                   ! Radius of the cluster where final state calculation is performed
 8.0
              ! For a good calculation, this radius must be increased up to 6 or 7 Angstroems
! SCF

! R_self
! 7

! N_self
! 100

 Green

! state_all

 Edge
 K

 Z_absorber
 8

 Atom
 83 1 6 1 3
 23 2 3 2 3 4 0 2
 8  2 2 0 2 2 1 4

 Dilatorb
 0 1 0.2

 Screening
 2 1 0.1

 Spgroup
 15:b1

 Crystal
 7.2532 11.702 5.096 90 134.234 90
1  0.0000 0.2500 0.6337
2  0.0000 0.2500 0.1352
3  0.1490 0.5060 0.2100
3  0.2580 0.3790 0.4510

!!!Convolution keyword : broadening with a width increasing versus energy as an arctangent
 Estart
 -20
Convolution
  42 11 10
 Gamma_hole
 0.5
 Gamma_fix
 Gaussian
 1.0
 End
```

References

1. D. L. Wood and J. Tauc, Weak Absorption Tails in Amorphous Semiconductors. Physical Review B 5, (1972), 3144 3.

2. E. A. Davis and N. F. Mott, Conduction in non-crystalline systems V. Conductivity, optical absorption and photoconductivity in amorphous semiconductors. Philosophical Magazine 22, (1970), 0903

3. Cooper, Jason K., et al., Indirect bandgap and optical properties of monoclinic bismuth vanadate. The Journal of Physical Chemistry C 119 (2015), 2969-2974.

6

Outlook

6.1 The role of science versus industry

Science is often the birth ground of new technologies. However, to truly incorporate new technologies into society, industry has to adopt them at a certain stage and aid their further development. For electrochemistry in general and CO_2 reduction in particular, this moment has now come. Reactor configurations currently exist where CO_2 can be reduced at almost 1 A/cm^2 with ~90% faradaic efficiency toward carbon-based products.[1] Industry should now take this knowledge and start working on upscaling, separation technologies and long-term stability tests. At the same time, science can still contribute by trying to understand catalyst degradation mechanisms, the interplay between reactants and their environment and improving selectivity toward specific products even further. Many of these studies will benefit greatly from operando studies, to which this thesis can hopefully provide a place to start.

The rest of this chapter is devoted to several issues that have emerged over the course of this PhD work as new fields of research. These topics have only recently become important since CO_2 reduction research has now matured to a point where it has become an interesting technology for industry. A brief techno-economic analysis is discussed to show which factors affect economic validity the most. Separation technology and intermittency are identified as severely underdeveloped but highly important research topics to have industrial-scale CO_2 reduction succeed; these are discussed as well.

6.2 Techno-economic background

In a research field where the ultimate goal is implementation into society, the cost of the technology is an omnipresent variable. The two main cost drivers for electrochemical CO_2 reduction are the electricity price and the cost of an electrolyser.[2] The main profit besides selling the product can be gained from policies rewarding storage options that can make intermittent power production more constant. High power electricity grids need to make expensive adjustments to their systems in order to keep up with projected solar photovoltaics (PV) and wind turbine parks since the increase of these loads make the variability bigger. Building electrolyser facilities next to wind or solar farms that can store the electricity would reduce the load on the grid, and could therefore become a profitable activity. The prices of solar PV and wind-generated electricity are falling fast, and are already cheaper than fossil fuel-based electricity in some parts of the world.

The type of product determines the amount of electrons needed per produced molecule and thus largely determines the cost price. Therefore, products that require few electrons to make and that have a high selling price under current technologies are expected to be the first to enter the market. Table 6.1 shows that carbon monoxide and formic acid are obvious initial products. Hydrogen has an even better electrons-to-price ratio and is in some cases already being produced electrochemically.[3] The cost of hydrogen electrolysers is dropping at the moment due to an increasing demand and developments in increasing electrolyser size.

A simple techno-economic analysis for CO and ethylene was recently published to be able to compare the economic value of these different CO_2 reduction products (Figure 6.1). The chosen parameters are quite optimistic, but might be within reach in the coming years. Since the parameters are the same for CO and C_2H_4 it becomes evident how big the effect of the number of required electrons is to the total production cost. The difference in selling price between CO and ethylene is relatively minor, yet electrochemical CO production is far more cost-competitive than ethylene production. Unless the energy conversion efficiency improves and the electricity price decreases significantly, it will be difficult to produce ethylene or higher order hydrocarbons such as diesel cost effectively through a purely electrochemical process. Instead, partial electrochemical pathways could be envisaged where either H_2 or syngas (CO + H_2) are

formed electrochemically and further conversions are performed through thermocatalytic or biological pathways. Methanol, having the same electrons/price ratio as ethylene, could become a very interesting product to make if subsidies for large-scale storage are added to the profits.

Table 6.1. Number of electrons needed to generate one molecule of product and their current market price[4,5]

Product	Electrons needed	Selling price $/tonne
Carbon monoxide	2	700[4] or 300[5]
Formic acid	2	400
Hydrogen	2	3900
Methane	8	200
Methanol	6	500
Ethanol	12	800
Ethylene	12	1000

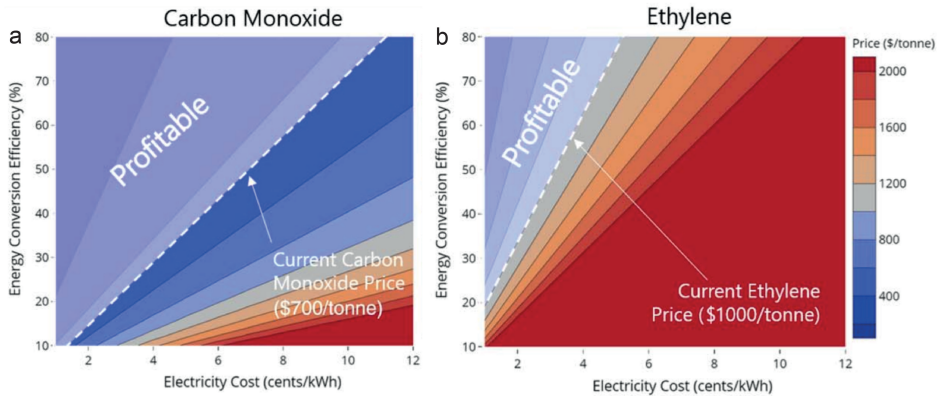

Figure 6.1. Basic techno-economic analyses for the electrochemical production of (a) CO and (b) C_2H_4. Based on a CO_2 price of 30 $/tonne, 90% FE, 500 mA/cm^2, $300/kW electrolyser cost, plant lifetime: 30 years. Reprinted from De Luna et al.[4]

6.2.1 Product separation

When considering the production of methanol, ethanol and formic acid through electrochemical CO_2 reduction, it is very important to study separation technologies, since these are liquid products that can be difficult to separate from an aqueous electrolyte. In theory, liquid products in the catholyte can be separated using distillation, although this is an energy intensive process. One method to reduce the overall energy consumption is process intensification, which can reduce the carbon and energy footprint by burning the hydrogen that is produced during CO_2 reduction as a side-product to heat the distillation column.[2] Other types of liquid separation technologies

should be studied to help improve the overall energy footprint of CO_2 reduction. Since not all liquid side products can be recovered from the electrolyte, the influence of trace amounts of liquid side products in the catholyte on the CO_2 reduction performance should be studied as well.

Gasses can be separated using pressure swing adsorption. For the CO_2 stream it is still unknown what effect the presence of side products such as hydrogen and carbon monoxide will have on the reaction efficiency. The influence of flue gas impurities is also not yet studied.

6.2.2 Intermittent operation

When electrochemical CO_2 reduction is used as a technology that can absorb the intermittent character of renewable electricity generation, it will not run continuously and at variable current density. Research is then needed to study whether CO_2 reduction can be performed at different current densities and if the electrolysers maintain their lifetime when they are switched on and off regularly. In order to finance an electrochemical CO_2 reduction facility that does not run continuously, the plant design needs to be simplified to save on capital cost. Certain separation techniques, like distillation boilers, can only run efficiently if they run continuously. Therefore, not recycling the electrolyte (which is done to stay below a 10% impurity level in the catholyte) is detrimental to the cost and energy balances of a CO_2 reduction facility when considerable amounts of liquid side products are expected.[2] Intermittent operation therefore only seems feasible for processes at near 100% Faradaic efficiency at high current density, unless new separation technologies are developed.

6.3 Conclusion

Clearly, a renewable electricity based society needs other technologies than what is presently available to become the main source of our energy supply. Electrochemistry, and in particular, CO_2 reduction can play an important and enabling role here. The CO_2 reduction technology does still have significant work to be done, in terms of stability, energy efficiency and cost reduction.

6.4 References

(1) Dinh, C.-T.; Burdyny, T.; Kibria, G.; Seifitokaldani, A.; Gabardo, C. M.; Arquer, F. P. G. de; Kiani, A.; Edwards, J. P.; Luna, P. De; Bushuyev, O. S.; et al. CO2 Electroreduction to Ethylene via Hydroxide-Mediated Catalysis at an Abrupt Reaction Interface. Science (80-.). 2018, 360, 783–787.

(2) Ege, H. B. Master Thesis: Electrochemical Production of Ethylene 2019.

(3) https://new.siemens.com/global/en/products/energy/renewable-energy/hydrogen-solutions.html.

(4) De Luna, P.; Hahn, C.; Higgins, D.; Jaffer, S. A.; Jaramillo, T. F.; Sargent, E. H. What Would It Take for Renewably Powered Electrosynthesis to Displace Petrochemical Processes? Science (80-.). 2019, 364, 3506.

(5) Bushuyev, O. S.; De Luna, P.; Dinh, C. T.; Tao, L.; Saur, G.; van de Lagemaat, J.; Kelley, S. O.; Sargent, E. H. What Should We Make with CO2 and How Can We Make It? Joule 2018, 2, 825–832.

Summary

Fossil resources are being depleted, while the concentration of CO_2 in the atmosphere rises (408.5 ppm in September 2019, against 401.5 in March 2015, when I started my PhD). All over the world, extreme weather events take place more frequently. There clearly is a strong and immediate need for a radical energy transition. Renewable energy is growing strongly as supplier of fossil-free electricity, but it needs large-scale and long-term storage options in order to be able to make a real impact on our total energy market. Another difficulty in eliminating fossil fuels from our society is the fact that petroleum is not only a feedstock for energy resources such as kerosene and gasoline, but also for many materials and chemicals that are being used in everyday life. A technology called electrochemical CO_2 reduction (CO_2R) can provide a solution to both these issues: renewably generated electricity is converted in any carbon-based energy containing molecule. The purpose (large-scale energy storage, mobile energy carrier or chemical) determines the molecule that should be produced.

Electrochemical CO_2 reduction is demonstrated at the lab scale. In order for it to become economically feasible and scalable to use in industry, additional research is needed to find better catalysts, understand the reactions and to improve cell design. The need for research includes a need for operando studies to investigate the exact physical and structural state of the catalyst under operating conditions. Also, relevant reaction intermediates cannot be studied without operando experiments. This thesis therefore focusses on the question how we can use existing operando characterisation techniques to study electrochemical systems.

The results obtained through operando studies in this thesis are combined with modelling work (Chapter 3) and ex situ material characterisation (Chapter 3 and 4) to better our understanding of CO_2 reduction. Reaction species can be monitored using infrared radiation (Chapter 2). There are pitfalls connected to operando studies. Since there is little literature to compare to, signals are easily misinterpreted. Operando experiments to study catalyst properties may also complicate the experimental set-up to such an extent that it is preferred to use ex situ characterisation instead (Chapter 5).

Attenuated total reflection Fourier transform infrared (ATR-FTIR) spectroscopy can be used to study reaction mechanisms since the technique is able to probe molecular species close to the ATR crystal. The ATR-FTIR signal strength decreases exponentially as a function of distance from the crystal, making it very suitable to study molecules that are adsorbed on the ATR crystal. In Chapter 2, this characteristic was exploited by depositing a silver film on the ATR crystal and using this as the cathode in CO_2 reduction. This way, adsorbates present on the cathode surface could be monitored during CO_2R. The results indicated a change in reaction mechanism between low (up to -1.55 V vs. Ag/AgCl) and high (-1.60 V vs Ag/AgCl) applied potential.

Literature has hosted a debate over the presence of oxygen in both oxide-derived silver (ODAg) and oxide-derived copper electrocatalysts. Its presence is difficult to confirm experimentally since it is a low concentration, low mass element, making most characterisation techniques unsuitable. X-ray photoelectron spectroscopy works well in low concentration and low mass, but often operates in vacuum, which could change the oxidation state of silver. In Chapter 3, a cell design for an electrochemical cell enabling operando X-ray absorption spectroscopy (XAS) studies on ODAg during CO_2 reduction is presented. The elongated ODAg cathode is covered by a thin layer of electrolyte and a polypropylene window, allowing the X-rays to pass at a shallow angle and probe only the first micrometres of the nanoporous ODAg. Experiments performed in this cell revealed the presence of a silver-oxygen bond, that at 2.28 Å is longer than average silver-oxygen bonds in silver oxides (up to 2.06 Å). The silver-oxygen bond concentration and length were modelled and compared to literature and considered accurate for this system. Several CO_2 reduction reaction mechanisms including the oxygen bond were hypothesised.

A gas-diffusion electrode (GDE) improves the performance of CO_2 reduction immensely due to the high concentration of CO_2 at the reaction site. Since the GDE-based CO_2 reduction research field is relatively recent, not much is known about the catalyst under relevant experimental conditions. Especially the effects of high current density (>50 mA/cm^2) on the catalyst are unknown, since such current densities are not possible in traditional H-cell systems. Chapter 4 presents a guide on how to conduct operando XAS experiments on GDE-based CO_2 reduction catalysts. The chapter discusses both the experimental details, the theory behind the technique, the most important shortcomings and presents work on silver and copper GDEs. The data shows how silver films are more polydisperse compared to copper films and that thin (20 nm) copper catalysts with reduced ethylene selectivity compared to 100 nm copper films are almost amorphous. Another important observation was the transformation that the copper samples underwent between reducing, ex situ, and open circuit conditions. In open circuit, the copper films quickly reduce in size compared to CO_2 reduction conditions, the same holds for ex situ samples. This confirms the earlier notion made in Chapter 3 that ex situ characterisation techniques can easily misinterpret the exact size and oxidation state of a catalyst.

Chapter 5 shows how light elements can be studied with hard X-rays using a technique called X-ray Raman scattering (XRS). In XAS, catalysts are probed with X-rays of an energy equal to the energy of the core electrons. This limits the availability of the technique to heavier (> 7000 eV) elements, since lower energy photons will not be able to penetrate through air or any other element without being fully absorbed. In XRS, a higher energy beam can be used and light-weight elements such as oxygen and carbon can be studied. Using XRS, in Chapter 5 the electronic effect of photocharging on

bismuth vanadate ($BiVO_4$) photoanodes is revealed to be the result of band bending induced by a bismuth borate surface layer. The surface layer is created by light soaking and the subsequent band bending directs photogenerated electrons toward the back contact, suppressing the surface recombination that often troubles $BiVO_4$.

CO_2 reduction research has progressed tremendously during the last 5 years. Large improvements in operating current densities and stability have raised the interest of companies to join in developing the technology further. This means that science should focus on furthering the understanding of CO_2 reduction under relevant conditions while industry works on upscaling and improving the cell and catalyst stability to thousands of hours. The operando methods developed in this thesis can help further scientific studies on electrochemical systems.

Samenvatting

Fossiele brandstoffen raken uitgeput, en tegelijkertijd stijgt de concentratie van CO_2 in de atmosfeer. Deze was 401.5 ppm in maart 2015, toen ik met mijn PhD begon en 408.5 in september 2019, aan het einde van mijn PhD. Extreem weer komt over de hele wereld steeds vaker voor. Dit maakt duidelijk dat er een dringende behoefte is aan een radicale energietransitie. Hernieuwbare energie groeit sterk als een leverancier van fossiel-vrije elektriciteit, maar er is behoefte aan lange termijn en grootschalige opslagmogelijkheden, wil fossiel-vrije elektriciteit een serieuze impact op de energiemarkt hebben. Een andere uitdaging van het elimineren van fossiele brandstoffen uit onze maatschappij is het feit dat petroleum niet alleen een grondstof is voor brandstoffen zoals kerosine en benzine, maar ook voor veel materialen en chemicaliën die men dagelijks gebruikt. Een technologie genaamd elektrochemische CO_2 reductie kan een oplossing bieden voor deze twee problemen: hernieuwbaar opgewekte elektriciteit kan worden omgezet in ieder op koolstof gebaseerd hoogenergetisch molecuul. Het doel (grootschalige energieopslag, of mobiele energiedragers, of chemicaliën) bepaalt het te produceren molecuul.

Elektrochemische CO_2 reductie is reeds bewezen op laboratorium niveau. Om het economisch rendabel en schaalbaar naar industrieel gebruik te maken is er meer onderzoek nodig naar betere katalysatoren, begrip van chemische reacties, en verbeterd cel ontwerp. Binnen deze onderzoeksrichtingen valt een sterke behoefte aan operando studies die de precieze fysische en structurele staat van de katalysator tijdens de chemische reacties kunnen meten. Ook relevante reactie intermediairen kunnen niet bestudeerd worden zonder operando experimenten. Deze PhD thesis focust daarom op de vraag hoe we bestaande operando karakterisatie technieken kunnen gebruiken om elektrochemische systemen te bestuderen.

De resultaten die met behulp van operando experimenten zijn behaald in deze thesis worden gecombineerd met modelleren (Hoofdstuk 3) en met ex situ materiaalkarakterisatie (Hoodstuk 3 en 4) om ons begrip van CO_2 reductie te verbeteren. Reaktie intermediairen kunnen gemeten worden met infrarood spectroscopie (Hoofdstuk 2). Er zitten ook nadelen aan operando studies. Aangezien er weinig vakliteratuur bestaat waarmee de metingen vergeleken kunnen worden, is het makkelijk om verkeerde interpretaties te maken. Ook kunnen operando metingen die als doel hebben de katalysator te bestuderen een meetopstelling in zulke mate compliceren dat het in sommige situaties beter is ex situ karakterisatie te gebruiken (Hoofdstuk 5).

Attenuated total reflection Fourier transform infrarood (ATR-FTIR) spectroscopie kan gebruikt worden om reactiemechanismen te bestuderen omdat deze techniek moleculen die zich in de buurt van het ATR kristal bevinden kan meten. Het signaal van de ATR-

FTIR meting neemt exponentieel af met de afstand tot het kristal, dit maakt het een uitermate geschikte techniek om moleculen die zich op de oppervlakte van het kristal bevinden te meten. In Hoofdstuk 2 is deze eigenschap gebruikt door een zilveren laag bij wijze van kathode voor de CO_2 reductie op de oppervlakte van het kristal aan te brengen. Op deze manier konden geadsorbeerde moleculen die aanwezig waren tijdens CO_2 reductie worden gemeten. De resultaten in dit hoofdstuk wijzen op een verandering in reactiemechanisme tussen lage (tot -1.55 V vs RHE) en hoge (-1.60 V vs RHE) aangelegde potentiaal.

Binnen de vakliteratuur is er een debat gaande over de vermeende aanwezigheid van zuurstof in zowel oxide-afgeleide zilveren (ODAg) en oxide-afgeleide koperen katalysatoren. De aanwezigheid van zuurstof is moeilijk experimenteel vast te stellen omdat het een element betreft dat in lage concentratie aanwezig is en een lage massa heeft. De meeste karakterisatietechnieken zijn hierdoor ongeschikt om de eventuele zuurstof te meten. X-ray photoelectron spectroscopie is wel geschikt binnen deze eisen, maar werkt onder hoog vacuüm. Hoog vacuüm kan de oxidatiestaat van zilver aantasten, waardoor deze techniek ook niet geschikt is. In Hoofdstuk 3 wordt een cel gepresenteerd waarmee operando X-ray absorption spectroscopie (XAS) metingen kunnen worden gedaan aan ODAg tijdens CO_2 reductie. De langwerpige ODAg kathode wordt bedekt door een dunne laag elektroliet en een polypropyleen venster, waardoor de X-ray bundel kan binnenkomen onder een zeer lage hoek, en zodoende alleen de eerste paar micrometers van het ODAg zullen meten. Metingen die in deze cel zijn gedaan wezen op de aanwezigheid van een zuurstof-zilver verbinding van 2.28 Å. Deze verbinding is significant langer dan de meeste zuurstof-zilver verbindingen in zilveroxides, deze zijn maximaal 2.06 Å lang. De concentratie en lengte van zuurstof-zilver verbindingen werden gemodelleerd, vergeleken met waardes uit de vakliteratuur en aannemelijk bevonden voor dit systeem. Tevens zijn verschillende mogelijke CO_2 reductie reactiemechanismen waarbij zuurstof een rol speelt beschreven.

Een gas-diffusie elektrode (GDE) verbetert de CO_2 reductie presaties aanzienlijk dankzij de enorm hoge CO_2 concentratie op de locatie van de reactie. Omdat het op GDEs gebaseerde CO_2 reductie onderzoeksveld nog relatief nieuw is, is er weinig bekend over de staat van de katalysator onder relevante reactiecondities. Vooral de effecten van hoge stroomdichtheden (>50 mA/cm^2) zijn niet bekend, omdat zulke stroomdichtheden onmogelijk zijn in traditionele H-cellen. Hoofdstuk 4 bevat een gids over hoe een operando XAS experiment uit te voeren op GDE-gebaseerde CO_2 reductie katalysatoren. Het hoofdstuk behandelt experimentele details, de theorie achter de techniek, de belangrijkste tekortkomingen van de techniek en presenteert metingen aan zilveren en koperen GDEs. Deze data laat zien dat zilveren GDEs een grotere verscheidenheid aan deeltjesgrootte hebben dan koperen GDEs. Ook blijken zeer dunne (20 nm) koperen GDEs niet alleen een slechtere selectiviteit voor ethyleenproductie te hebben dan 100

nm koperen GDEs, maar ook bijna volledig amorf te zijn. Een derde belangrijke observatie was de verandering die de koperen films doormaakten tussen reducerende, ex situ en open circuit omstandigheden. Zodra de films in een open circuit gebracht worden krimpt de kristalgrootte aanzienlijk ten opzichte van de reducerende omstandigheden, hetzelfde geldt voor de ex situ omstandigheden. Dit bevestigt de eerdere opmerking gemaakt in Hoofdstuk 3, namelijk dat ex situ karaterisatietechnieken makkelijk een verkeerd beeld kunnen geven van de exacte grootte en oxidatiestaat van een katalysator onder realistische omstandigheden.

Hoofdstuk 5 laat zien hoe lichte elementen bestudeerd kunnen worden met harde X-rays met een techniek genaamd X-ray Raman scattering (XRS). Met XAS worden katalysatoren gemeten met X-rays van dezelfde energie als de energie van diens kernelektronen. Dit maakt de techniek alleen geschikt voor zware (> 7000 eV) elementen, omdat X-rays met een lagere energie niet in staat zijn om door lucht of andere elementen te dringen zonder volledig geabsorbeerd te worden. In tegenstelling tot XAS, kan met XRS een bundel van hogere energie dan de te meten elementen worden gebruikt. Dit maakt deze techniek geschikt om lichte elementen zoals zuurstof en koolstof te bestuderen. In Hoofdstuk 5 is met behulp van XRS ontdekt dat het foto-laden ('photocharging') van bismut vanadaat ($BiVO_4$) fotoanodes zorgt voor een bismut boraat oppervlaktelaag die leidt tot buigende banden in $BiVO_4$. De oppervlaktelaag wordt gecreëerd door lange blootstelling aan licht en de daarop volgende buiging van banden duwt de fotogegenereerde fotonen in de richting van het elektrische contact aan de achterzijde, dit onderdrukt de recombinatie aan de oppervlakte die vaak voorkomt bij $BiVO_4$.

Onderzoek naar CO_2 reductie is enorm vooruit gegaan gedurende de laatste 5 jaar. Grote verbeteringen in operationele stroomdichtheden en stabiliteit hebben de interesse van de industrie gewekt om mee te werken aan de verdere ontwikkeling van deze technologie. Dit betekent dat de wetenschap zich moet richten op het verbeteren van het begrip van CO_2 reductie onder relevante reactieomstandigheden terwijl de industrie kan werken aan de opschaling en de verbetering van de stabiliteit van cellen en katalysatoren richting duizenden uren. De operando methodes die zijn ontwikkeld in deze thesis kunnen een bijdrage leveren aan verdere wetenschappelijke studies aan elektrochemische systemen.

List of publications

Firet, N.J.; Burdyny, T.; Nesbitt, N.T., Chandrashekar, S.; Longo, A.; Smith, W.A., Copper and silver gas diffusion electrodes performing CO_2 reduction studied through operando X-ray absorption spectroscopy, Catal. Sci. 2020, under review

Firet, N.J.; Venugopal, A.; Blommaert, M.A.; Cavallari, C.; Sahle, C.J.; Longo, A.; Smith, W.A., Chemisorption of anionic species from the electrolyte alters the surface electronic structure and composition of photocharged $BiVO_4$, Chem. Mater. 2019, 31, 7453−7462.

Firet, N.J.; Blommaert, M.A.; Burdyny, T.; Venugopal, A.; Bohra, D.; Longo, A.; Smith, W.A., Operando EXAFS Study Reveals Presence of Oxygen in Oxide-Derived Silver Catalysts for Electrochemical CO_2 Reduction. J. Mater. Chem. A 2019, 7, 2597–2607.

Firet, N.J.; Smith, W.A., Probing the Reaction Mechanism of CO_2 Electroreduction over Ag Films via Operando Infrared Spectroscopy. ACS Catal. 2017, 7 (1), 606–612.

Van Oversteeg, C.; Tapia Rosales, M.; Helfferich, K.H.; Ghiasi, M.; Meeldijk, J.D.; Firet, N.J.; Ngene, P.; de Mello Donegá, C.; de Jongh, P., Copper sulfide derived nanoparticles supported on carbon for the electrochemical reduction of carbon dioxide, Catal., 2020, under review

Sassenburg, M.; Burdyny, T.; Nesbitt, N.T.; Kas, R.; Chandrashekar, S.; Firet, N.J.; Yang, K.; Lui, K.; Blommaert, M.A.; Kolen, M.; Ripepi, D.; Smith, W.A., Characterizing CO_2 reduction catalysts on gas diffusion electrodes: A direct comparison of transition metals, ACS Catal. 2020, in preparation

Veerbeek, J.; Firet, N.J.; Vijselaar, W.; Elbersen, R.; Gardeniers, H.; Huskens, J., Molecular Monolayers for Electrical Passivation and Functionalization of Silicon-Based Solar Energy Devices. ACS Appl. Mater. Interfaces 2017, 9 (1), 413–421.

Abdi, F.F.; Firet, N.; van de Krol, R., Efficient $BiVO_4$ Thin Film Photoanodes Modified with Cobalt Phosphate Catalyst and W-Doping. ChemCatChem 2013, 5, 490–496.

Review article: Kas, R.; Ayemoba, O.; Firet, N.J.; Middelkoop, J.; Smith, W.A.; Cuesta, A., In-situ infrared spectroscopy applied to the study of the electrocatalytic reduction of CO_2: Theory, Practice and Challenges, ChemPhysChem 2019, doi.org/10.1002/cphc.201900533

Patent: Jones T.W.; Wilson, G.J.; Anderson, K.F.; Hollenkamp, A.F.; Duffy, N.W.; Firet N.J., Process of forming a photoactive layer of an optoelectronic device. 2015. Issued Dec. 18, 2018. US20180005764A1.

Acknowledgements

Acknowledgements time. We are in the middle of the Corona outbreak, so I haven't seen many of you in quite a while but I hope these words of thanks will reach you at some point. Getting your PhD is a journey with highs and lows and so many people have helped me through this period, thank you all for making it unforgettable.

First of all, I want to thank the person who got me into this crazy and amazing part of my life: Wilson. Based on what you heard from Fatwa and other MECSicans, you offered me a PhD position. And since I loved MECS and really enjoyed your enthusiasm during our first meeting, I took it. Wilson, I once tried to tell someone what your supervision meant to me. I decribed it as my biweekly dose of motivation. Your endless enthusiasm and optimism in our biweekly meetings are what got me through the tough times. Thank you so so much for that. I will try to take some of your cheer with me in my mind to encourage me on my further adventures. And thank you for being just as passionate about saving the world as I am. The team you have assembled over the years was the best team I could have wished for to have as my collegues.

Bernard, as my other promotor you were always there in the background. A few times during my PhD your supervision has been a great help. We have had wonderful in-depth discussions and I greatly appreciate your help during the last few months with finalising my PhD under unusual circumstances. As a leader, you have a combination of personal attention and practical decisiveness that I greatly admire and strive towards myself.

During my PhD, I estimate that I have eaten approximately 80 pieces of cake and 2700 cookies during coffee breaks. I would like to thank everyone involved: cake makers, cookie buyers, coffee makers, attendees of coffee breaks: you made my days and have kept me well fed. Besides the coffee breaks, all the people in MECS have been great in many, many ways. I will miss you all! Herman, Joost, Bart and many technicians from other groups: Marcel, Ben and Ruben thanks for all your help with suddenly crashing equipment, weird experimental ideas I wanted to persue and calmly helping me when I was not calm at all. Heleen and Rajshree, thank you for all your kind words and help with little administrative annoyances, MECS misses you both! MECS is an ever evolving group of great people that I cannot all name personally due to its high conversion rate. But to name a few: my dear office mates Fahimeh, Christiaan, Kai and Marijn, thanks for making our office great. Divya, we were great conference room-mates with perfectly non-matching time schedules, I loved it!

I want to thank everyone who has been to ESRF with me: Bartek, Ming, Marco and Kai for the initial trips where damage control was the main task. Anirudh and Marijn for our bizarre psychedelic trip during Sinterklaas where thanks to super long

measurements we were able to relax a bit in between measurements. A slightly less soothing trip was the next one where we added Tom to our beam team. Then Nate, Sanjana and Tom for the smooth final beam time, thanks for making it a relatively relaxed experience. Besides the beam teams, there are many people within DUBBLE and ID20 I would like to thank for all their help and for making me feel so at home in Grenoble: Marcus, Chiara, Christoph, Dip, Florian, Aleksei and Christian. So much science depends on the amazing staff of ESRF, thank you!

And of course, there would be no thesis on electrochemical operando science without the help of Ale. Thank you so much for all the time and effort you have spent teaching me XAS, doing data analysis with me, giving me extra beam time, keeping me motivated, inviting me to meet your family and so much more! I am honoured to call you my friend.

There is no better way to end a day full of science (good or bad) than by bouldering the night away with some great friends. Giorgio, Nate, Marijn, Katie and Peter, thanks for all the great evenings, weekends and even a holiday we spent together climbing and talking about life. To many more!

A great thanks to all my students over the years! Dear Edward, Vincent, Jael, Joram, Jorrit, Rebecca, Jasper, Nicolo and Berna. Thank you for teaching me and letting me teach you. I really enjoyed supervising all of you! And a special thanks to Boaz, who was never my student but who helped me enormously during the last stage of my PhD.

And then there are so many friends and family completely unrelated to science but all instrumental in helping me get here. Many of your little nudges have helped me made my choices. And being able to talk about other things than science has helped me even more. Mama en papa, thanks for always letting me choose my own path. Thank you for making me strong and independent and for your never ending support. Tessa, I am proud to be your big sister, it is amazing to see how you choose your own path in life. Thank you for your inspiration. Rosan, Sonne, Vincent, Joël, and so many others, thanks for all the great dinners and talks we shared!

Peter, thank you for being my rock. For always being there for me and giving me just what I needed. After 9 years together we have both been through tough things but we have always been able to help each other through them. And after nine years were are still happily and effortlessly in love, this amazes me every day. For that I am eternally greatful.

Curriculum Vitae

Nienke Joan Firet was born in Amsterdam, the Netherlands on May 21st, 1989. In 2012, she received her bachelor's degree in Molecular Science and Technology from Delft University of Technology. In 2015, she obtained two master degrees from the University of Twente: one in Chemical Engineering, where she did the Molecules and Materials track. The other degree was in Sustainable Energy and Technology, the Solar Energy track. The subject of her Master thesis was the development of a molecular electrical passivation layer to improve the efficiency of photocathodes made of silicon micropillars. Both master degrees were received cum laude and for this she was awarded with the Unilever Research prize 2015. She worked for 6 months as a researcher at the Commonwealth Scientific and Industrial Research Organisation (CSIRO) on the development of safer fabrication methods for perovskite solar cells. From 2015 to 2019, she worked on her PhD thesis in the Materials for Energy Conversion and Storage group at the TU Delft under the supervision of Wilson Smith. The work she did during her PhD was focussed on finding techniques to study electrochemical processes under operating conditions.